Engineered Science

REVIEW PAPER View Article Online

Recent Advances on the Electromagnetic Wave Absorption Properties of Ni Based Materials

Biao Zhao,*[1,2] Jiushuai Deng,[2,3] Rui Zhang,*[1,4] Luyang Liang,[1] Bingbing Fan,[4] Zhongyi Bai,[1] Gang Shao[4] and Chul B. Park[2]

Electromagnetic interference problems have become an increasing problem with the rapid development of wireless information technologies and electronic devices at high frequency ranges, and this has stimulated much attention. To tackle this challenge issue, the electromagnetic absorbing materials that can attenuate electromagnetic waves are urgently pursued. The desired absorbers should include high-efficiency absorption, wide dissipation band, low cost, and being lightweight. Due to high saturation magnetization and permeability at high GHz frequency, ferromagnetic Ni has been considered as a high efficiency electromagnetic absorption. However, the eddy current effect caused by high electrical conductivity, would limit the application. To tackle this problem, two effective ways including designing hierarchical structure and compounding are explored. This paper reviews the state-of-the-art research in the design of Ni based composites as electromagnetic absorption materials. The ultimate goal of these Ni based absorbers is to achieve the strong absorption, the broader effective absorption frequency. The core-shell, yolk-shell and hollow porous structures are introduced into Ni based composites (Ni-metal, Ni-polymer, Ni-semiconductor and Ni-carbon composites) to enhance the electromagnetic absorption properties. Particularly, combing with carbonaceous (CNTs or graphene), the Ni-carbon ternary or quaternary even more phases composite would be a target direction to design high-efficiency electromagnetic absorption capability.

Keywords: Electromagnetic absorption; Ni-based absorbers; Eddy current effect; Core-shell structure; Impedance match

Received 16th May 2018, Accepted 17th June 2018

DOI: 10.30919/es8d735

1. Introduction

Electromagnetic interferences (EMI) can be described as conducted and/or radiated electromagnetic signals emitted by electrical circuits which, under operation, perturb proper operation of surrounding electrical instruments or cause irradiative damage to living/biological species.[1–10] The extensive development of gigahertz (GHz) electronic systems and telecommunication devices has elevated the electromagnetic pollution to a level never attained before, which endows an active quest for novel and effective EM absorbing material solutions in a wide variety of applications. Numerous applications are concerned from commercial and scientific electronic instruments to antenna systems and military electronic devices.[11–22] Another military application is stealth, devoted to the reduction of the detectability of target by canceling reflections of a radar signal incident to its surface. Nowadays, the development of high performance microwave absorbing materials (MAMs) with thin thickness, low density, wide bandwidth, and strong absorption have stimulated great interests to eliminate the electromagnetic pollution.[23–26] Because they can absorb electromagnetic waves effectively and transform electromagnetic energy into heat energy or attenuate electromagnetic waves by interference.[27–31]

Among the candidates of electromagnetic absorbers, metallic magnetic materials usually possess high saturation magnetization and thus high permeability at high frequency (1-18 GHz), as a result they can be widely used to prepare thinner absorbing materials along with high efficiency electromagnetic absorption properties.[32–44] However, as a fact of matter, the metallic materials usually have relatively high electrical conductivity, and their permeability decreases very rapidly at high frequency thanks to the eddy current losses caused by the alternated electromagnetic fields, which is generally named as skin-depth effect.[45–49] When the high frequency electromagnetic waves encounter a microwave absorption material, they penetrate only the near-surface region, and the phenomenon is known as the skin effect. Moreover, the depth, at which the amplitude of the incident electromagnetic wave dissipates to 1/e of the surface value is called as the skin depth and it can be expressed as:[50–54]

$$\delta = \sqrt{\frac{1}{f\pi\mu\sigma}} \quad (1.1)$$

[1] *Henan Key Laboratory of Aeronautical Materials and Application Technology, School of Mechatronics Engineering, Zhengzhou University of Aeronautics, Zhengzhou Henan 450046, China. E-mail: biao_zhao@zua.edu.cn, bzhao@mie.utoronto.ca, zhangray@zua.edu.cn*

[2] *Department of Mechanical and Industrial Engineering, University of Toronto 5 King's College Road, Toronto, Ontario M5S 3G8, Canada. E-mail: biao_zhao@zua.edu.cn, bzhao@mie.utoronto.ca*

[3] *State Key Laboratory of Complex Nonferrous Metal Resources Clean Utilization, Faculty of Land Resource Engineering, Kunming University of Science and Technology, Kunming 650093, China*

[4] *School of Material Science and Engineering, Zhengzhou University, Zhengzhou, Henan 450001, China. E-mail: zhangray@zua.edu.cn*

Herein f is the frequency, μ is the magnetic permeability, σ is the electrical conductivity. From the above formula, the skin depth is related with the measured frequency, permeability, and conductivity. For instance, nickel (Ni) has a skin depth of about 1 μm over 1-5 GHz. That is to say, if Ni particles possess sizes larger than 1 μm, then only the surface part with a thickness of about 1 μm will play a positive role to electromagnetic response, while the remain interior portion makes no contribution. Thus, it is urgently suggested to deal with this problem to boost the electromagnetic absorption properties of magnetic metallic Ni materials.

Up to now, it is well anticipated that there are two effective ways to address this issue, namely, to decrease the size of Ni particles or fabricate complex hierarchical shape, and to compound with other materials to form unique structure, such as core-shell, yolk-shell or porous structures to improve the impedance match and dissipation capability. This review article focuses on the state-of-the-art of Ni-based electromagnetic absorption materials, and the related electromagnetic attenuation theory about how to enhance absorption properties through above mentioned method is also discussed in detail.

2. The fundamental theory of electromagnetic absorption

In this section, the fundamental theory of electromagnetic (EM) absorption will be described. When the EM wave is incident on a dissipated material, the experience can be divided into three processes:[55–63] reflection, absorption and transmission, which definitely obeys the laws of optics, as shown in Fig. 1. The reflection of the EM waves containing surface reflection and multiple reflection, meaning that the promotion of the multiple reflection will induce extended transmitted routes of the EM wave, and further improve the absorbing ability of the EM wave absorbents.[64–66] Then, the incident electromagnetic energy can generate heating within the material by the aid of the interactions of the electromagnetic field with the material's molecular and electronic structure, which would transfer the incidence EM wave into thermal energy, causing an energy dissipation. Therefore, there are two main avenues to enhance EM wave absorption, one is by increasing the transmitted routes of the EM wave in the absorbers by adjusting their nanostructures, and the other is by regulating the electromagnetic parameters to enhance the EM absorption ability.

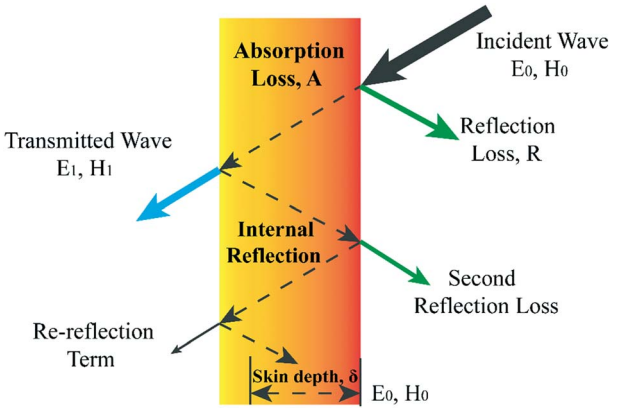

Fig. 1 Schematic of an incident electromagnetic wave through the dissipation materials.

In order to eliminate the transmission of EM through an absorbing material and evaluate the absorption properties by analyzing the reflection of the wave, the United States Naval Research Laboratory (NRL) arch measurement method is used to measure the reflected power of the materials placed on a metal panel.[67–69] The EM absorbing property of the materials is evaluated with reflection loss (RL), which can be expressed as the following equation:

$$RL(dB) = 10\log_{10}(P_R / P_I) \tag{2.1}$$

In which P_I and P_R stands for the incident power and reflection power of an EM wave, respectively. When RL is less than -10 dB, only 10% of the EM powder is reflected and 90% of the EM energy is absorbed. However, for NRL-arch method, a metal substrate (generally Al substrate) should be applied to make all of the transmitted electromagnetic wave reflect and enter into the absorber again. Thus, numerous researchers used the waveguide and coaxial-line methods[70–79] to characterize the electromagnetic absorption properties of absorbing materials based on the following equations:[80–88]

$$RL = 20\log_{10}\left|(Z_{in} - Z_0)/(Z_{in} + Z_0)\right| \tag{2.2}$$

$$Z_{in} = Z_0\sqrt{\frac{\mu_r}{\varepsilon_r}}\tanh\left(j\frac{2\pi fd\sqrt{\mu_r\varepsilon_r}}{c}\right) \tag{2.3}$$

In this equation, Z_0 = 376.7 Ω is the impedance of the air and Z_{in} the input impedance of samples. The $\varepsilon_r = \varepsilon' - j\varepsilon''$ and $\mu_r = \mu' - j\mu''$ are the complex permittivity and permeability of the paraffin composite in air, f is the frequency, c is the velocity of light, and d is the absorber thickness. Generally, the frequency range over which the RL is smaller than −10 dB is regarded as the effective absorption bandwidth. On the basis of above formulas, the electromagnetic absorption performance of absorber is closely related to the complex relative complex ($\varepsilon_r = \varepsilon' - j\varepsilon''$) and permeability ($\mu_r = \mu' - j\mu''$).[89–93] It is well accepted that the real permittivity (ε′) and permeability (μ′) symbolize the ability to store the electric and magnetic energy, while the imaginary permittivity (ε″) and permeability (μ″) stand for the dissipation of electric and magnetic energy.[94–96]

The complex permittivity can be computed from the S-parameters collected from the measurement. S-parameters S_{11} and S_{21} can be expressed via reflection coefficient Γ and transmission coefficient T as:[97–101]

$$S_{11} = \frac{(1-T^2)\Gamma}{1-\Gamma^2T^2} \tag{2.4}$$

$$S_{21} = \frac{(1-\Gamma^2)T}{1-\Gamma^2T^2} \tag{2.5}$$

$$\Gamma = \frac{Z - Z_0}{Z + Z_0} = \frac{\sqrt{\mu_r / \varepsilon_r} - 1}{\sqrt{\mu_r / \varepsilon_r} + 1} \tag{2.6}$$

$$T = e^{-\gamma d} \tag{2.7}$$

where $\gamma = j\frac{2\pi f}{c}\sqrt{\mu_r \varepsilon_r}$, c is the velocity of light, f is the measured frequency. Then, based on these equations, we can deduce that the complex permittivity and permeability are described as:

$$\mu_r = \mu' - j\mu'' = (\frac{1+\Gamma}{1-\Gamma}) j \frac{\ln(T)}{2\pi d} \frac{c}{F} \tag{2.8}$$

$$\varepsilon_r = \varepsilon' - j\varepsilon'' = \frac{j\frac{\ln(T)}{2\pi d}\frac{c}{F}}{\mu} \tag{2.9}$$

Herein $F = \frac{\omega}{2\pi}$, d is the thickness of absorbing material. The coaxial-line method is so popular because it just needs a tiny absorbing materials (generally less than 0.2 g, depending on the filling ratio). Before obtaining the RL value, the scattering parameters (S parameters) are obtained by a vector network analyzer using the coaxial-line method (as shown in Fig. 2(a,c)) for which the samples are prepared by homogeneously mixing paraffin wax (paraffin wax is transparent to electromagnetic wave, as a result, for a sample/paraffin wax composite, the electromagnetic absorption property was just considered from the absorbing materials) and then pressing into toroidal-shaped samples of 7.0 mm in outer diameter and 3.04 mm in inner diameter (Φ_{out}: 7.0 mm, Φ_{in}: 3.04 mm, as shown in Fig. 2b).[21,102–105]

To achieve excellent electromagnetic wave absorption properties, two important factors should be taken into account. The prerequisite condition is the impedance matching condition between the electromagnetic wave absorber and free space. In order to obtain zero reflection at the front surface of the samples, the characteristic impedance of the samples ought to be equal/close to that of the free space. To achieve a good impedance matching, it is necessary to make the material having the same or similar ε_r and μ_r. The impedance matching degree Δ can be expressed by the following equations:[22,106–117]

$$|\Delta| = |sinh^2(Kfd) - M| \tag{2.10}$$

And, the values of K and M are also calculated through the complex permittivity and permeability by the following equations:

$$K = \frac{4\pi\sqrt{\varepsilon'\mu'\sin\frac{\delta_\varepsilon + \delta_\mu}{2}}}{c\cos\delta_\varepsilon\cos\delta_\mu} \tag{2.11}$$

$$M = \frac{4\mu'\varepsilon'\cos\delta_\varepsilon\cos\delta_\mu}{(\mu'\cos\delta_\varepsilon - \varepsilon'\cos\delta_\mu) + \left[\tan\left(\frac{\delta_\mu}{2} - \frac{\delta_\varepsilon}{2}\right)\right]^2 (\mu'\cos\delta_\varepsilon + \varepsilon'\cos\delta_\mu)^2} \tag{2.12}$$

It is worth noting that a smaller absolute value of delta (Δ) means a better impedance matching.

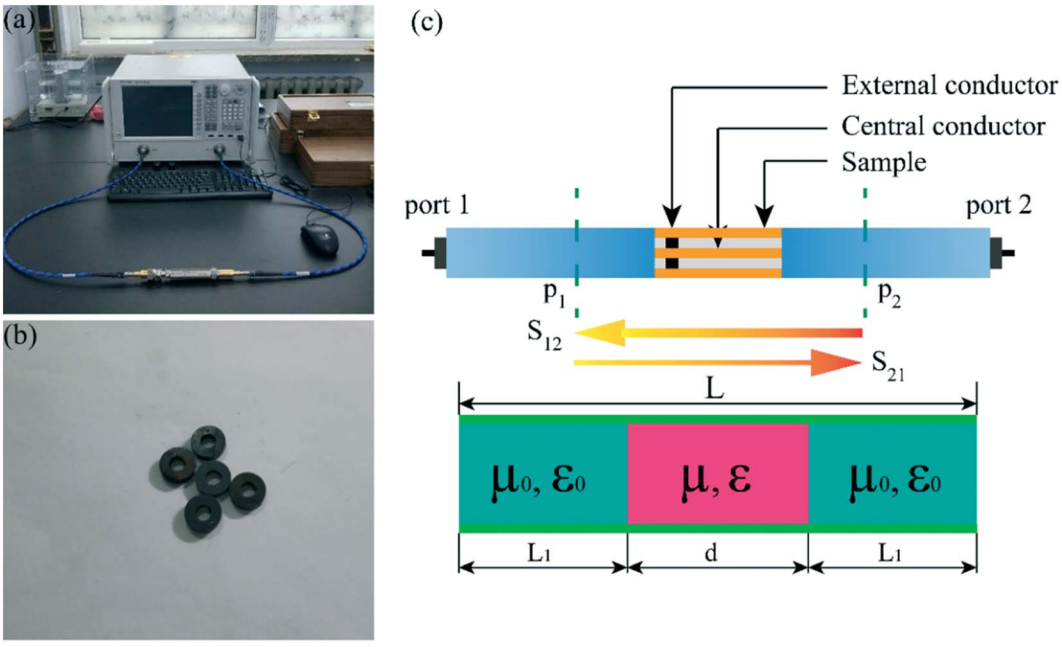

Fig. 2 (a) The picture of vector network analyzer; (b) Picture of ring-like paraffin based samples to be tested; (c) Schematic diagram of coaxial-line measurement method.

The other important parameter is the microwave attenuation ability in the interior of microwave absorber, which can make the microwave absorber sufficiently dissipate the incident microwaves by the intrinsic magnetic and dielectric loss features. The electromagnetic wave dissipation ability of the microwave absorber can be evaluated by attenuation constant (α):[118–122]

$$\alpha = \frac{\sqrt{2}\pi f}{c} \times \sqrt{\left(\mu''\varepsilon'' - \mu'\varepsilon'\right) + \sqrt{\left(\mu''\varepsilon'' - \mu'\varepsilon'\right)^2 + \left(\mu'\varepsilon'' + \mu''\varepsilon'\right)^2}} \tag{2.13}$$

where f is the frequency and c is the velocity of light. From this equation, it is noted that high values of ε″ and μ″ would result in high a value. The metallic magnetic Ni is a dual-loss absorber, which is made up of the dielectric loss and magnetic loss. Thus, it will render absorbers with high electromagnetic dissipation capability.

Besides above mentioned reasons for electromagnetic absorption, the electromagnetic wave can be absorbed via the "geometrical effect", which means that when the thickness of absorber satisfies the equation:[123–130]

$$d = \frac{l\lambda_m}{4}\left(l = 1,3,5,...\right) \tag{2.14}$$

$$\lambda_m = \frac{\lambda_0}{\sqrt{|\mu_r||\varepsilon_r|}} \tag{2.15}$$

where λ_m is the wavelength at certain frequency, $|\mu_r|$ and $|\varepsilon_r|$ are the moduli of μ_r and ε_r, and λ_0 is the wavelength in the free space, the incident and reflected waves in the absorber are out of phase 180° and resulting the reflected waves in the air-absorber interface are totally canceled. Yan et al.[124] used oxidative molecular layer deposition to fabricate one dimensional Fe_3O_4-poly(3,4-ethylenedioxythiophene) (PEDOT) nanospindles with controllable PEDOT thickness. Their absorption performance was evaluated in the 2-18 GHz frequency range (Fig. 3), and the bandwidths with RL values less than -10 dB get much broader with the increase of PEDOT cycles. Moreover, the absorption peaks move to lower frequencies by increasing the PEDOT cycles (Fig. 3a) and sample thickness (Fig. 3b), covering three Ku, X, and C microwave bands. This indicates that deposition thickness of PEDOT and absorber thickness can tune absorption bandwidth and achieves selective-frequency absorption. Therefore, by control of absorbing materials' thickness, we can design a promising electromagnetic wave absorbing materials with the strong absorption and selective-frequency absorption properties.

For the dielectric loss, as reported by other researchers, the dielectric loss behaviors are mainly related to conduction loss and polarization loss,[37] and polarization loss basically comes from ionic polarization, electronic polarization, dipole orientation polarization and interfacial polarization (space charge polarization).[5] Ionic polarization and electronic polarization always work in higher frequency region (10^3-10^6 GHz),[131] and dipole orientation polarization from the frustrated reorientation of dipoles (bound charges in defects and residual groups) prefers frequency dispersion.[70] The conduction loss usually occurs only when high metallic magnetic Ni contents was dispersed into paraffin matrix to form conductive network.[46–48] This high amount was limited in practical application. Therefore, the interfacial polarization and dipoles polarization can considerably influence the permittivity. Normally, the Debye theory is considered to be a

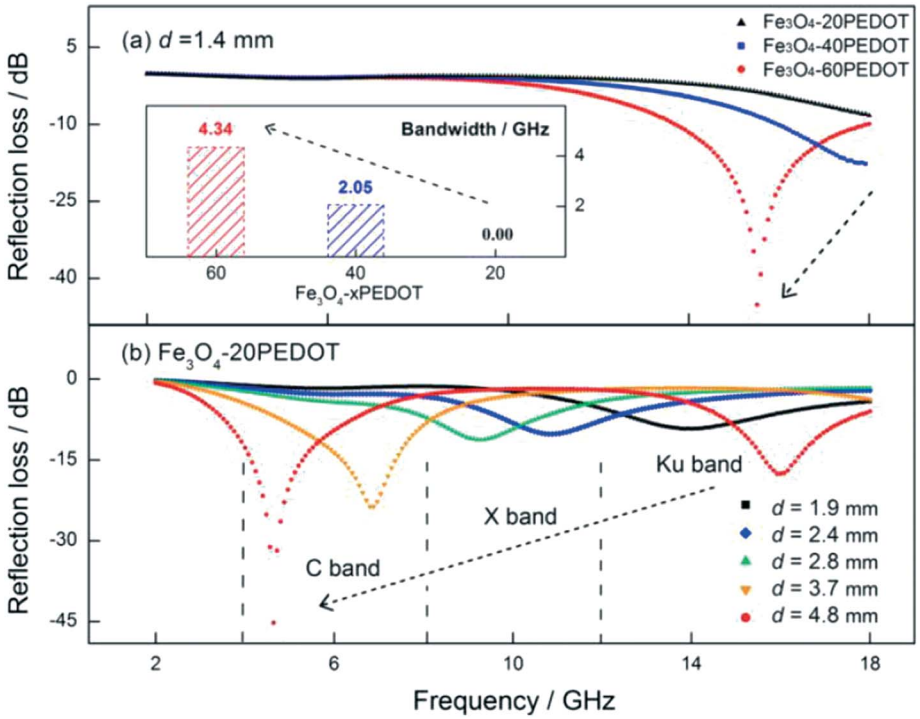

Fig. 3 (a) RL curves of Fe_3O_4-xPEDOT nanospindles with a 1.4 mm thickness; (b) RL curves of Fe_3O_4-20PEDOT nanospindles with different matching thicknesses. (Reprinted with permission from Ref. [124]. Copyright 2017, American Chemical Society.)

powerful tool to understand the dielectric properties of absorbers. According to the Debye dipolar relaxation, the relative complex permittivity can be described by the following equation: [76,88,132–146]

$$\varepsilon_r = \varepsilon_\infty + \frac{\varepsilon_s - \varepsilon_\infty}{1 + j2\pi f\tau} = \varepsilon' - j\varepsilon'' \tag{2.16}$$

where ε_s, ε_∞, f, τ are the static permittivity, relative dielectric permittivity at the high-frequency limit, frequency and polarization relaxation time, respectively. From the eqn (1), it can be deduced that

$$\varepsilon' = \varepsilon_\infty + \frac{\varepsilon_s - \varepsilon_\infty}{1 + (2\pi f)^2\tau^2} \tag{2.17}$$

$$\varepsilon'' = \frac{2\pi f\tau(\varepsilon_s - \varepsilon_\infty)}{1 + (2\pi f)^2\tau^2} + \frac{\sigma}{(2\pi f)^2\varepsilon_0} \tag{2.18}$$

Inferred from eqn (2) and (3), we can obtain the relationship between ε′ and ε″ that

$$\left(\varepsilon' - \frac{\varepsilon_s + \varepsilon_\infty}{2}\right)^2 + (\varepsilon'')^2 = \left(\frac{\varepsilon_s - \varepsilon_\infty}{2}\right)^2 \tag{2.19}$$

Therefore, the plot of ε′ versus ε″ would be a single semicircle, which is usually defined as the Cole–Cole semicircle, and each semicircle is correlated with one Debye relaxation process.[107,147,148] Wang et al[143] and coworkers prepared the reduced graphene oxide (RGO)/CuS nanocomposites with CuS microspheres embedded in reduced graphene oxide (RGO) layers, and the dielectric loss was described by the Cole–Cole semicircle' theory. Fig. 4 shows ε′-ε″ curves of the pure PVDF, RGO/CuS/PVDF (5 wt%), (10 wt%) and (15 wt%). One obvious Cole–Cole semicircle is found in the ε′-ε″ curve of pure PVDF (Fig. 4a) and complex semicircles in RGO/CuS/PVDF, indicating the existence of the Debye relaxation process in the pure PVDF and RGO/CuS/PVDF composites. In the meanwhile, more semicircles are clearly found in the curve of the RGO/CuS/PVDF composites, which represent the contribution of the Debye relaxation process to the enhanced wave absorption properties of the RGO/CuS/PVDF composites.

The magnetic loss of the absorber was mainly from many impacts including hysteresis, resonance, eddy current effect, and so forth.[87,149–154] Herein, the magnetic hysteresis is negligible in the case of weak magnetic field. Although the loss from the domain wall resonance often exists in relatively low frequency which is below gigahertz, it is also negligible at 1–18 GHz.[121,155,156] Therefore, in the present case of Ni based absorbers, the magnetic loss mainly originates from other three factors: natural ferromagnetic resonance,[157–160] exchange resonance [33,161,162] and eddy current effect. The natural resonance frequency is related to the magnetic anisotropic properties of the material. According to ferromagnetic resonance theory, the relationship between the natural resonance frequency f_r and the anisotropy energy Ha is:[163–167]

$$f_r = \gamma H_a / 2\pi \tag{2.20}$$

$$H_a = \frac{4|K|}{3\mu_0 M_s} \tag{2.21}$$

$$K = \frac{\mu_0 M_S H_c}{2} \tag{2.22}$$

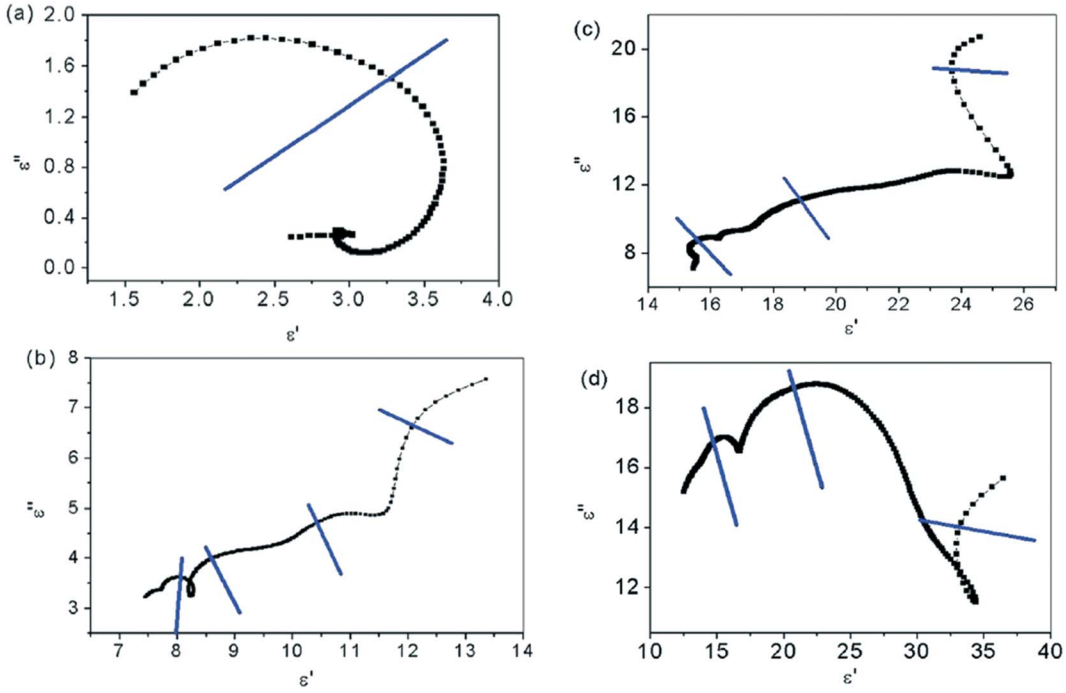

Fig. 4 The ε′-ε″ curves of (a) pure PVDF, and with (b) loading of 5 wt%, (c) loading of 10 wt%, (d) loading of 15 wt% of the RGO/CuS composites. (Reprinted with permission from Ref. [143]. Copyright 2013, Royal Society of Chemistry.)

where f_r is the resonance frequency, γ is gyromagnetic ratio, and Ha is anisotropy field. K is the anisotropy coefficient, μ_0 is the vacuum permeability ($4\pi \times 10^{-7}$ N·A^{-2}), H_c is the coercivity, and M_s is saturation magnetization. It can be seen from the equation that the high anisotropy energy is related to the high anisotropy coefficient, and the increase of the anisotropic energy causes an increase of the natural resonance frequency. Therefore, it is possible to tune the resonant frequency by changing the anisotropy field of magnetic particles.

The eddy current loss is correlated to the diameter (d) and the electric conductivity (σ), which can be described as:[168–171]

$$\mu'' \approx 2\pi\mu_0 (\mu')^2 \sigma d^2 f / 3 \quad (2.23)$$

In which f is the applied frequency, μ_0 is the vacuum permeability. From the above equation, if magnetic loss only originates from eddy current loss, the values of C_0 should be constant as the frequency is varied, which is called the skin-effect criterion.[172–176]

$$C_0 = \mu''(\mu')^{-2} f^{-1} = 2\pi\mu_0\sigma d^2 / 3 \quad (2.24)$$

3. Ni-based materials as EM absorbers

3.1. Pure magnetic Ni as EM absorber

As above mentioned, thanks to the relatively high electrical conductivity of metallic Ni materials, the permeability decreases very quickly at high frequency, namely, eddy current effect.[170–172] One effective way is to reduce the size of Ni particles to nanometers or fabricate the hierarchical structural Ni, which would decreases the eddy current effect.

3.1.1. Ni particles with nanoscale size. In our previous investigation,[177] we studied the effect of size on the electromagnetic absorption properties of Ni particles. From Fig. 5(b-d), one can notice that three Ni particles with the sizes of 780 nm, 420 nm and 100 nm, respectively, could be obtained. Fig. 5a shows the electromagnetic absorption of the three Ni samples with a thickness 2 mm. As for the Ni-780, it has weak ability to absorb EM wave in the 1-18 GHz. For the Ni-420 sample, one strong peak (-17.3 dB, 12.2 GHz) was clearly observed. The absorption bandwidth is up to 3.2 GHz (from 10.3 to 13.5 GHz). In comparison with those two Ni samples, the Ni-100 wax-composite has different intensities and positions of RL peaks. The sharp RL peak reaches -26.4 dB at 9.3 GHz and the effective electromagnetic absorption band covering a frequency range of 8.3-10.1 GHz were obtained. The Ni-420 and Ni-100 samples possess better microwave absorption than that of the Ni-780 sample, which is attributed to the good impedance match[178–180] and synergetic effect between magnetic loss and dielectric loss.[181–183] Furthermore, the nanoscale Ni particles with a high density of point defects (such as vacancies) and dangling bonds are prone to polarization in an electromagnetic wave field, and the quantum size effect of nanoparticles could result in the splitting of the electron energy that accompanies the formation of a new band gap, also leading to the absorption of electromagnetic energy.[184,185] Wang et al.[186] reported hollow Ni spheres were prepared by electroless plating on carbonyl iron and template corrosion method. The real (ε′) and imaginary (ε″) parts of complex permittivity of hollow nickel spheres first

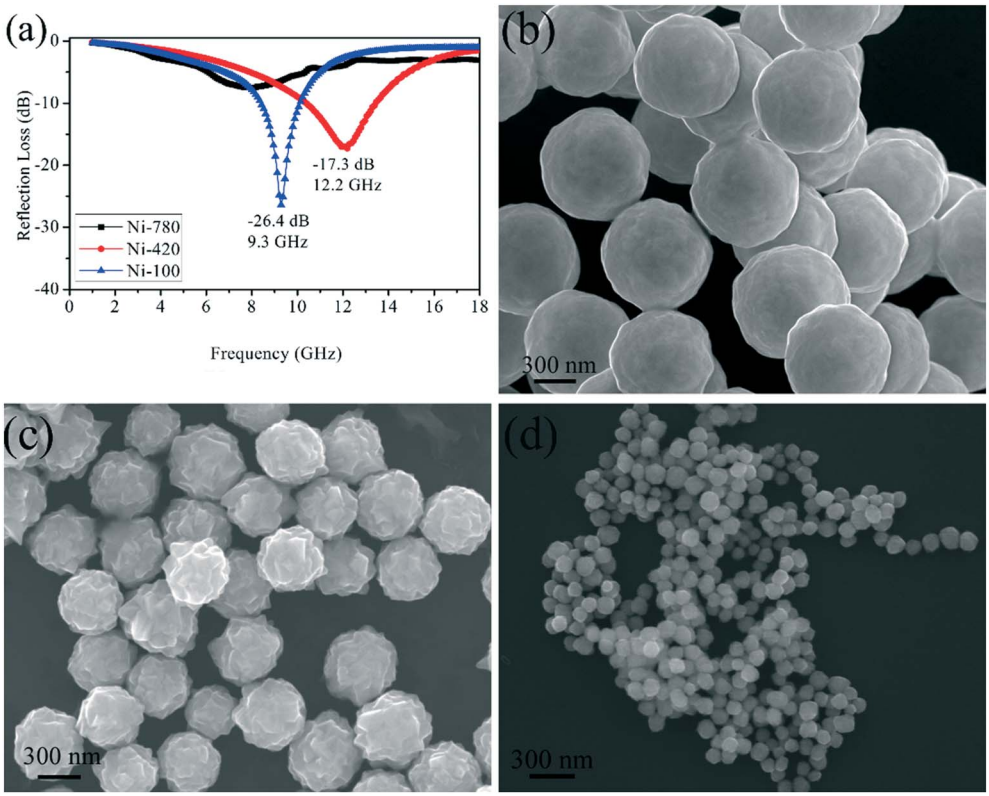

Fig. 5 (a) The comparison of frequency dependence of RL (dB) for the Ni wax-composites with a thickness of 2 mm; SEM images of Ni particles with different size: (b) 780 nm, (c) 420 nm, and (d) 100 nm. (Reprinted with permission from Ref. [177]. Copyright 2015, Elsevier B.V.)

increased and then decreased as the shell thickness increased, and the sample with the thinnest shell showed the lowest complex permittivity. For the complex permeability, the resonance peak shifted to the lower frequency and then moved to higher frequency, as the shell thickness increased. The microwave absorption performances could be tuned by changing the shell thickness. In their study, the minimum RL (RL) value of −27.2 dB was obtained at 13.4 GHz with a matching thickness of 1.4 mm.

3.1.2. Ni particles with hierarchical structure. If we design the Ni particles with hierarchical complex structures, we can obtain the reasonable Ni absorbers with low conductive property. Moreover, the hierarchical complex structure would get high permeability thanks to the high anisotropy shape.[187–189] Furthermore, the complicate structure could also absorb electromagnetic wave, which is called as "structure absorption". In following sections, we focus on the electromagnetic properties of Ni particles with one-dimensional (1D), two-dimensional (2D) and three-dimensional (3D) complex structures.

3.1.2.1. One-dimensional (1D) structural Ni as absorber. One-dimensional (1D) structured Ni particles, which could be synthesized via wet-chemical methods by the aid of external magnetic fields, surfactants, and templates,[190–192] have attracted more and more attentions due to their new challenging magnetic properties. When 1D Ni particles were deliberately designed as microwave absorbing materials, besides anisotropy shape causing magnetic variation, the unique 1D structure could be expected to be as antenna receives to induce point charge to dissipate microwave energy, and also cause orientation polarization loss,[184,193–195] which would absorb more electromagnetic wave.

The 1D structural Ni particles, such as nanowires, nano-fibers and nano-chains are proved to be the promising electromagnetic absorbers.[196–200] In our team, 1D Ni chains were successfully prepared by a facile solvothermal method.[197] The measured electromagnetic parameters displayed that the effective absorption bandwidth was up to 4.3 GHz in the high frequency range of 13.7-18.0 GHz by tuning the thickness of 0.8-1.0 mm. A minimum RL value of −19.9 dB was observed at 17.2 GHz with only thickness of 0.8 mm. The excellent electromagnetic absorption mainly resulted from dielectric loss rather than magnetic loss.

Gong et al.[198] fabricated the ultrafine Ni fibers under normal pressure via the reduction of Ni^{2+} ions by hydrazine hydrate in the absence of any templates or external magnetic field, and the electromagnetic properties of Ni fibers were correspondingly investigated. Fig. 6 presents the typical SEM images of the Ni fibers obtained at 70 °C from the reaction systems with various NaOH/Ni^{2+} molar ratio. It is noted that the concentration of NaOH has an evident influence on the nucleation and growth of Ni nanocrystallites during the chemical reaction. One can notice that a higher molar ratio of NaOH/Ni, e.g., 15 and 7.5, is favorable to preparing uniform Ni fibers with an average diameter of about 500 nm and a length of 50 μm (Fig. 6a,b). Contrarily, at a lower NaOH/Ni^{2+} ratio, short twist Ni fibers were obtained (Fig. 6c), and spherical/chain-like Ni powders co-existed at a too low concentration of NaOH (Fig. 6d). Therefore, the authors claimed that they selected the molar ratio of NaOH/Ni as 7.5. The calculated RL curves of composites A (Ni fiber filler) and B (Ni particle filler) in relation to the frequency of electromagnetic wave and thickness (1-5 mm) of absorber layer are shown in Fig. 6(e,f). It can be seen that the morphology of the Ni fillers has an obvious effect on the electromagnetic absorption behavior. Namely, composite A with an absorber layer thickness of 2.0 mm exhibits a RL of less than -10 dB at 6.6-8.8 GHz, and a minimum RL of -39.5 dB is obtained at 4.8 GHz with an absorber layer thickness of 3.0 mm (Fig. 6e). Expectedly, composite B (Fig. 6f) has a weak electromagnetic wave absorbance over the whole frequency range of 2.0-18.0 GHz. The authors attributed the excellent microwave absorbance of composite A to the proper electromagnetic impedance matching.

Liu and coworkers [199] fabricated the nickel chains by a facile wet chemical method, and the morphology of nickel chains were tailored by adjusting the amount of PVP during the synthesis process. The complex permittivity and permeability of the three-dimensional (3D) nets constructed by nickel chains present strong dependences on temperature in the frequency range of 8.2-12.4 GHz and temperature range of 323-573 K. The peaks in imaginary component of permittivity and permeability mainly derive from interfacial polarizations and resonances (Fig. 7e), devoting to dielectric and magnetic loss, respectively. Fig. 7(a–c) exhibit the 3D plots of RL values versus frequency and thickness for the samples with 30, 40, and 50 wt% chain nets loadings. Compared with 30 and 40 wt% loading samples, the 50 wt% loading sample has the best electromagnetic wave absorption performance with a thinnest thickness. The RL value can reach approximately -50 dB by tuning temperature, and the effective bandwidth is expanded obviously. Fig. 7d demonstrates the 3D bar plot of their maximum absorption in the temperature range of 323-573 K and X band with the thickness range of 1-5 mm. It is observed that the maximum absorption of 50 wt% loading sample is much better than others, especially at 373 K.

3.1.2.2. Two-dimensional (2D) structural Ni as absorber. For the ferromagnetic absorbers, it is reported that the 2D structure, such as flakes, can cause high shape anisotropy,[32,65,170,201–203] which is beneficial to the electromagnetic absorption. However, to the best of our knowledge, the electromagnetic properties of 2D structural Ni particles were scarcely found in the publications.[204] Wang et al.[204] fabricated the hexagonal Ni/$Ni(OH)_2$ heterogeneous structure plates through a reduction reaction system. In Fig. 8, enhanced microwave absorption of Ni/$Ni(OH)_2$ hexagonal plates in comparison with smooth chains and rings is due to the synergistic effect of magnetic loss and dielectric loss. Specially, the urchin-like nickel chains exhibit a best absorption property in contrast with other as-synthesized samples, which was due to the geometrical effect, and point discharge effect.

3.1.2.3. Three-dimensional (3D) structural Ni as absorber. It is well accepted that the morphology play a vital role on the microwave absorption performances of Ni samples. Particularly, as for the 3D hierarchical complex structure, such as flower-like,[135,205–208] urchin-like,[159,209] and octahedral-shape,[210] would introduce the shape anisotropy to tune permeability. On the other hand, these special structure would cause "structure absorption", constrain electromagnetic wave in absorbers to prolong travel path to dissipate more electromagnetic energy.

In our group,[135] the flower-like Ni structures composed of leaf-like flakes were synthesized through a facile solvothermal approach independent of surfactants or magnetic force (Fig. 9(a,b)). The electromagnetic absorbing properties of the flower-like Ni wax-composite were evaluated in term of the complex permittivity ($\varepsilon_r = \varepsilon' - j\varepsilon''$) and permeability ($\mu_r = \mu' - j\mu''$). The results demonstrated that the wax-based composites containing 70 wt% Ni flowers showed excellent electromagnetic wave absorbing characteristics and the RL values less than -10 dB are

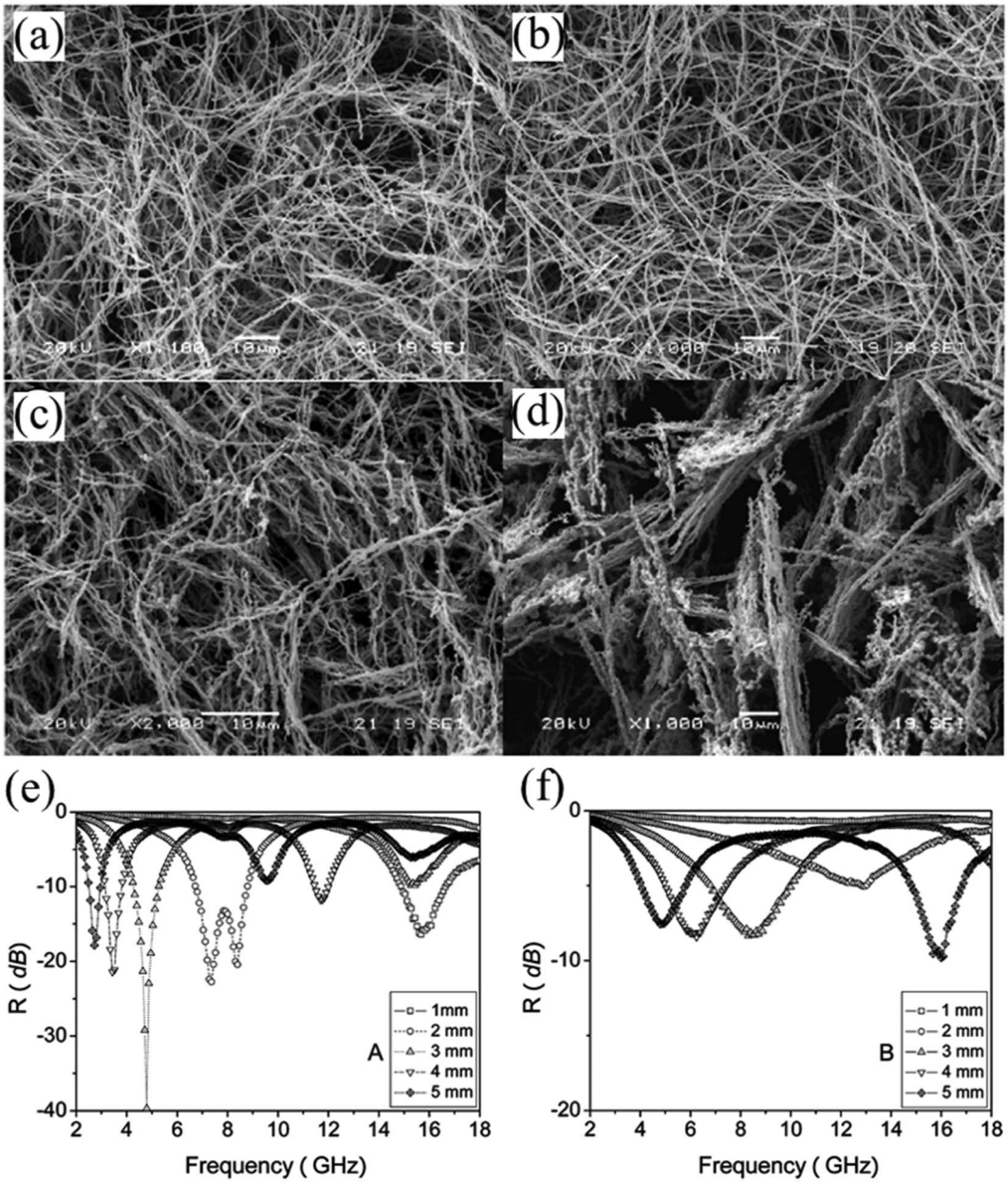

Fig. 6 SEM images of Ni fibers obtained at 70 °C from the reaction systems with different NaOH/Ni molar ratios: (A) 15, (B) 7.5, (C) 2.0, and (D) 0.4. The RL (RL) of Ni fiber-filled (e) and Ni particle-filled (f) paraffin-based composites with different thicknesses. (Reprinted with permission from Ref. [198]. Copyright 2010, American Chemical Society.)

obtained in the frequency range of 2.5–16.4 GHz range with absorber thicknesses of 1.8–6.0 mm. The flower-like Ni presents a minimum RL value of -46.1 dB at 13.3 GHz for the thickness of 2.0 mm (Fig. 9c). The excellent microwave absorbing performance was ascribed to dielectric loss rather than the magnetic loss, and unique flower-like structures.

Tong et al.[210] reported a facile template-free and one-pot thermal decomposition approach to fabricate submicrometer-sized NiO octahedral, and the octahedral Ni with tailored crystallization and texture characteristics were easily achieved through H_2-annealing of NiO octahedra at various temperatures. The electromagnetic properties were closely associated with their microstructures. Fig. 10 shows the electromagnetic wave absorption characteristics of the Ni octahedral obtained at different temperatures. For the porous octahedral Ni powders formed at 300 °C, when the volume fraction was 3 v%, RL values (below -20 dB, corresponding to 99% dissipation) covered the range of 3.04 GHz to 8.49 GHz with thicknesses of 4.0 -10 mm, while the minimum RL value of -30.99 dB appeared at 6.64 GHz with the optimal thickness of 5.0 mm (Fig. 10a). When improved the volume fraction to 4 v% induces an excellent electromagnetic absorption property, a minimum RL value of -37.93 dB could be observed at 12.80 GHz with a matching thickness of 2.5 mm (Fig. 10b). Furthermore, the bandwidth below -20 dB was over 3.20-5.20 GHz and 8.40 -18.00 GHz. However, further increasing the volume fraction to

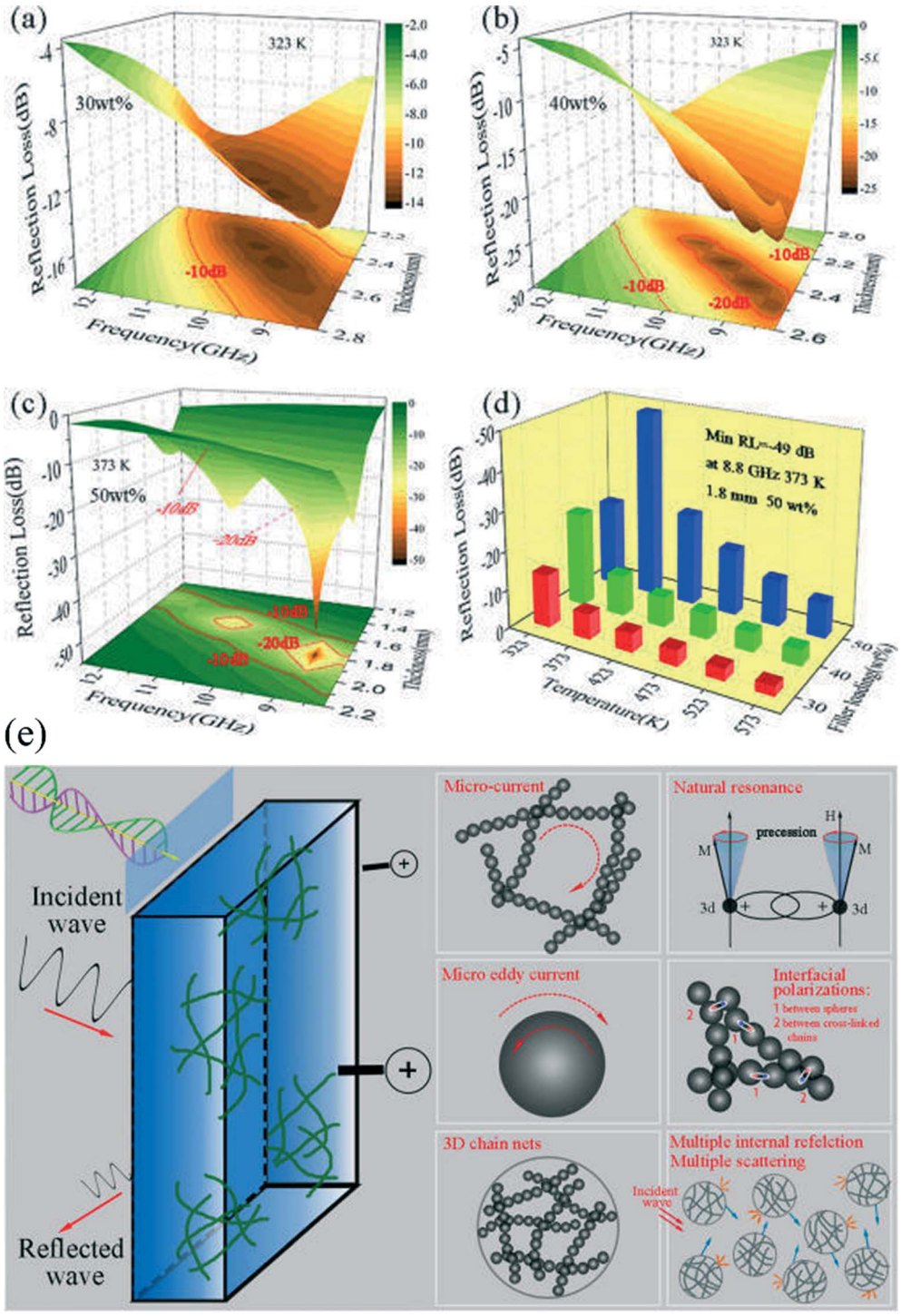

Fig. 7 (a-c) 3D plots of RL versus frequency and thickness for samples with 30, 40, and 50 wt% 3D nickel chain nets loadings, respectively; (d) 3D plot of minimum RL evaluation for all the samples; (e) Schematic illustration of microcurrent, micro eddy current, natural resonance, dielectric polarizations, and microwave propagation in 3D nickel chain nets. (Reprinted with permission from Ref. [199]. Copyright 2016, American Chemical Society.)

5 v%, thanks to the mismatch between the free space impedance and the input impedance, electromagnetic absorption property dropped (Fig. 10c). For the porous octahedral Ni powders prepared at 350 °C, an optimal absorption property was achieved at a volume fraction of 3 v% (Fig. 10d). The bandwidth (RL below -20 dB) was 8.24 GHz, with the minimum RL value of -40.44 dB at 8.80 GHz. In comparison with the above mentioned porous Ni octahedra, the solid Ni octahedra and the spherical Ni exhibited weak electromagnetic wave absorbing properties (Fig. 10(e,f)).

The authors also investigated the electromagnetic absorption mechanism of Ni octahedra. Porous octahedral nanomaterials demonstrated characteristics different from those of solid octahedral and

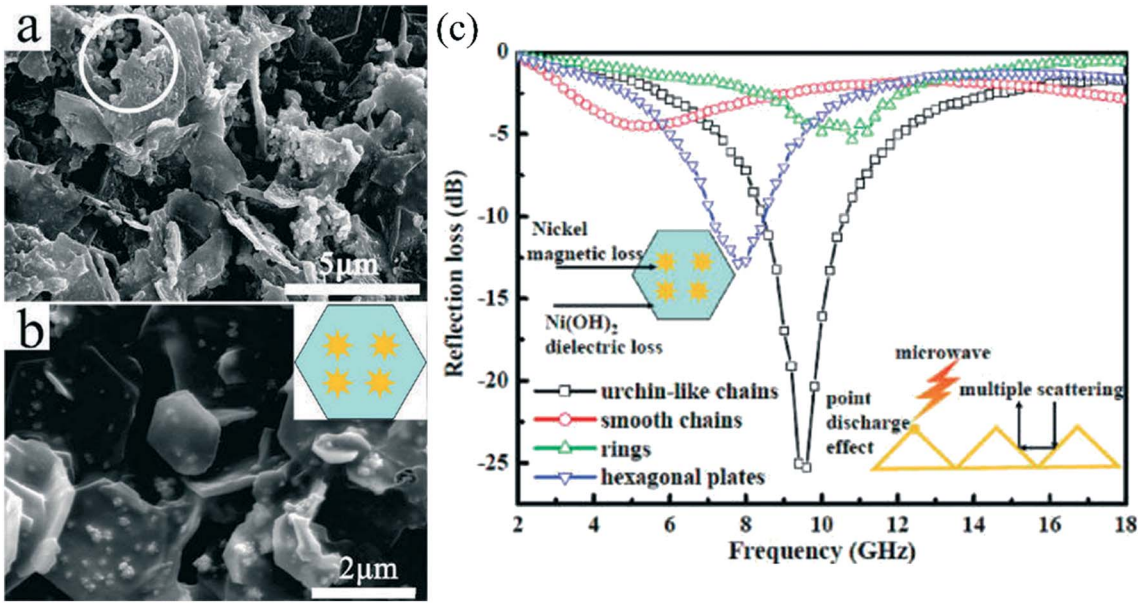

Fig. 8 SEM images of hexagonal Ni/Ni(OH)$_2$ plates after reaction for (a) 1.5 h and (b) 3h (the right inset is the scheme of hexagonal Ni/Ni(OH)$_2$ heterogeneous structure plate); of differently shaped samples in the frequency range 2-18 GHz with the samples thickness of 2 mm. (Reprinted with permission from Ref. [204]. Copyright 2010, American Chemical Society.)

spherical samples in terms of enhanced permittivity parameters and dielectric loss. They attributed it to the following reasons: First, the porous nanostructures can induce the vibrating microcurrent inside the pores, which can improve the conduction loss; Second, the octahedral nanomaterials randomly distributed in the matrix can cause multiple scattering and further attenuate EM waves; Third, the octahedral shapes

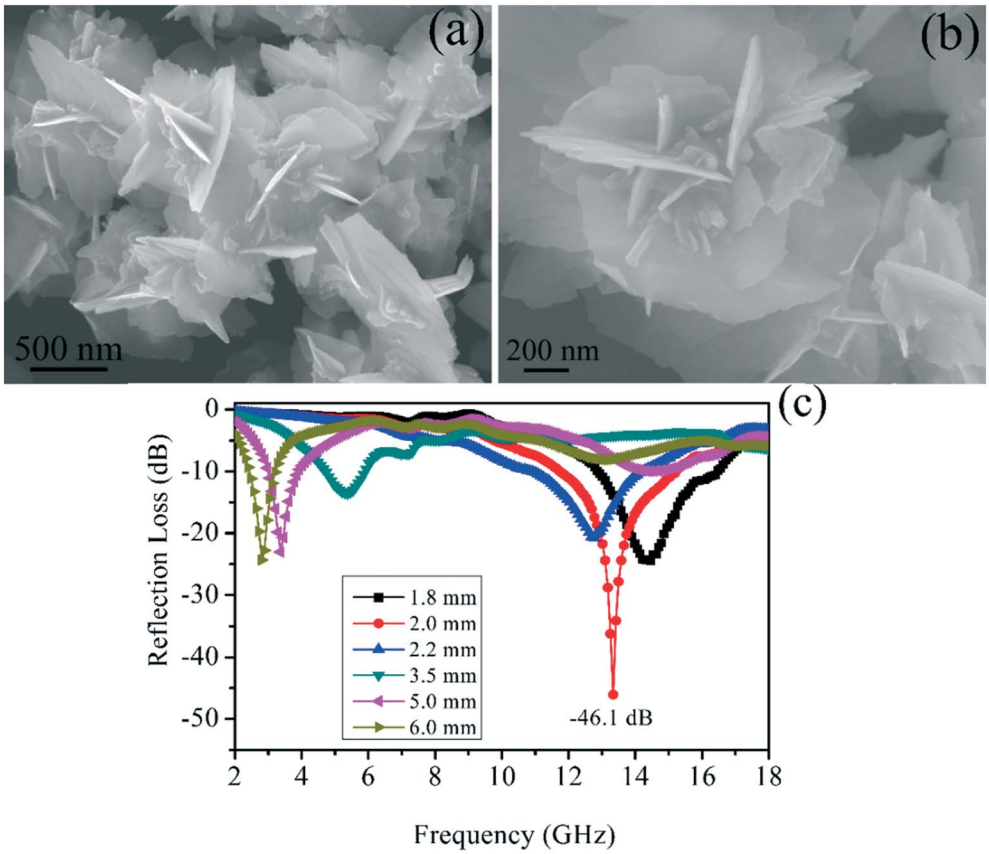

Fig. 9 (a,b) SEM images of the flower-like hierarchical structural Ni; (c) Calculated RL curves dependent on the thickness of flower-like Ni/paraffin composites in the frequency range 2.0-18.0 GHz. (Reprinted with permission from Ref. [135]. Copyright 2014, Springer.)

can consider as isotropic quasi-antennae, which prompted penetration of EM waves.

The above EM energy was further converted and induced into a dissipative current and then consumed in the discontinuous networks.

3.2. Ni based composites as EM absorbers

To decrease the eddy current effect, another effective avenue is to compound Ni with other materials to form tunable microstructure, as a result, we could obtain outstanding electromagnetic absorption performance. Although the pure Ni particles with designable microstructures could obtain the optimal EM absorption performance, the tradeoff would be the higher filler content and the larger absorber thickness. In addition, the pure Ni particles are easily oxidized to prohibit their practical application. Therefore, in order to optimize EM absorption ability, an efficient strategy is to compound Ni with other materials to produce special microstructure. In this section, we will discuss the EM properties of Ni-metal, Ni-polymer, Ni-semiconductor, and Ni-carbon composites.

3.2.1. Ni-metal composite as EM absorber. Magnetic metal nanoparticles may be quite suitable materials as EM wave absorbers because of small size, large specific surface area, high surface atom percentage, and more dangling chemical bonds, which might lead to the interface polarization and the activation of nanoparticles. However, each kind of metal nanoparticles has its intrinsic properties and usually can be used only in a specified frequency range. To meet the above requirements, the development of metal composite nanoparticles may be an efficient strategy.

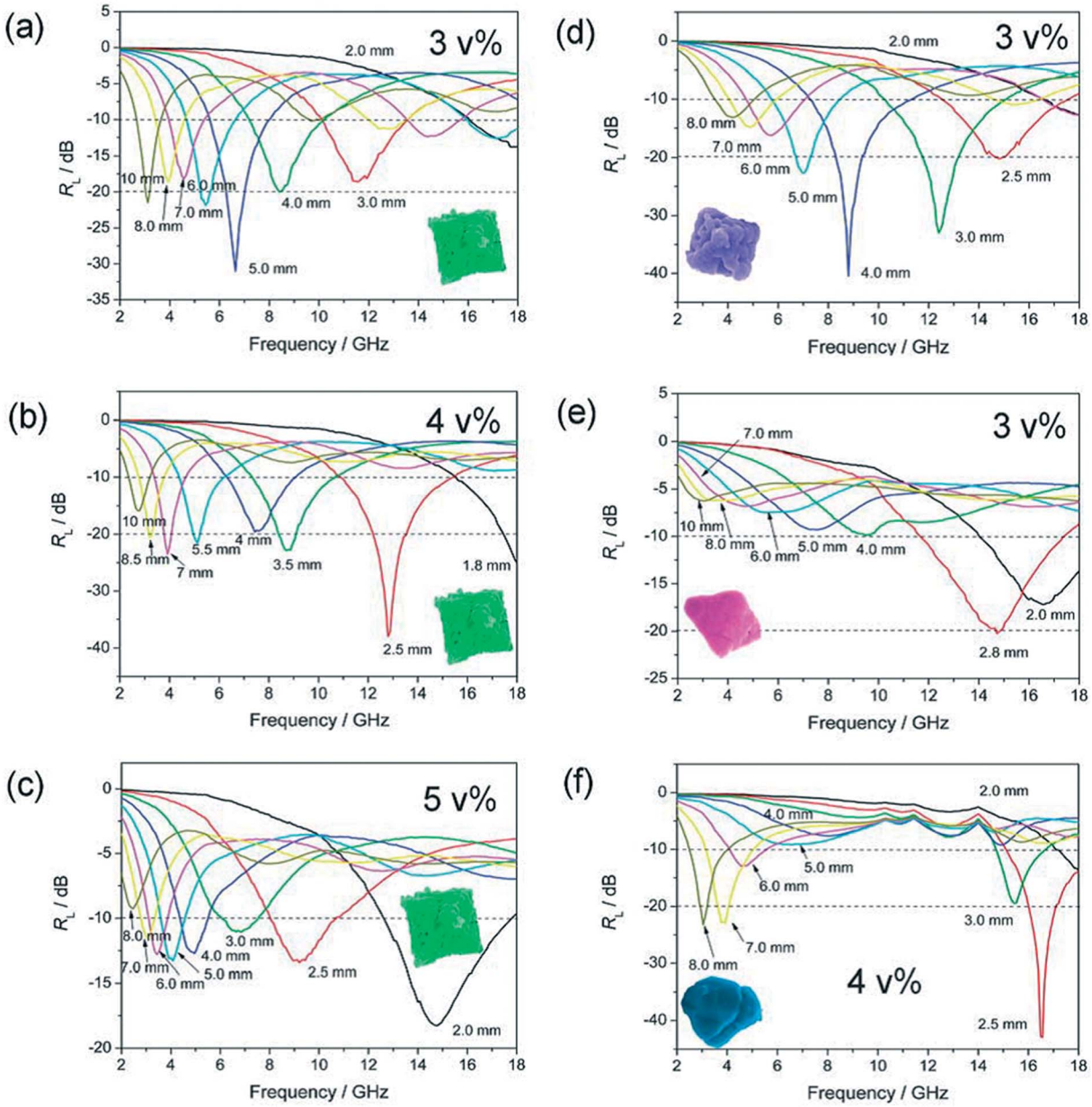

Fig. 10 RL curves of paraffin-based composites containing octahedral Ni with various volume fractions produced at different temperatures: (a to c) 300 °C, (d) 350 °C, (e) 450 °C, and (f) 700 °C. (Reprinted with permission from Ref. [210]. Copyright 2012, Royal Society of Chemistry.)

3.2.1.1. Ag-Ni composite as EM absorber. Lee et al.[211] prepared Ni–Ag core-shell nanoparticles by the successive hydrazine reduction of nickel chloride and silver nitrate in ethylene glycol. The electromagnetic wave absorption properties of the epoxy resin composites containing Ni, Ag, and Ni–Ag core-shell nanoparticles were studied. The results demonstrated that Ni-Ag core-shell nanoparticles showed a dual-frequency absorption property in 2-18 and 18-40 GHz, in comparison with Ni nanoparticles, which exhibited absorption only in 18-40 GHz, and no absorption could be found for Ag nanoparticles in the whole frequency range. The additional absorption of Ni–Ag core-shell nanoparticles in 2-18 GHz might result from the lags of polarization between the core/shell interfaces, which made the contribution to the dielectric loss. Moreover, his team also investigated the electromagnetic wave absorption properties of Ni-Ag composite with various molar ratios embedded in the epoxy at the frequency of 2-40 GHz.[212] Interestingly, the authors found that both the Ni_3Ag_1 and Ni_1Ag_3 nanocomposite particles showed dual-frequency absorption in 2-18 and 18-40 GHz. The reason was that the Ni- and Ag-rich microdomains might be formed within the Ni_3Ag_1 and Ni_1Ag_3 nanoparticles, leading to the appearance of the second absorption mechanism due to the lags of polarization at the interfaces as the frequency was varied.

Guo et al.[213] fabricated core-shell Ag@Ni nanoparticles and constructed on the bayberry tannin (BT) grafted skin collagen fiber (SCF) though a simple one-step route (Fig. 11). They found that these SCF-supported Ag@Ni core–shell NPs composites can be used as high-performance electromagnetic absorption materials in the whole X-band, C-band and some part of S-band with minimal RL (RL) of -51 dB (Fig. 11e). The analysis of electromagnetic parameters indicated that the enhancement of dielectric loss properties of SCF-supported Ag@Ni core–shell NPs was introduced by the multiple defective site polarization and interfacial polarization in bimetallic interface. Moreover, thanks to the combination of magnetic property in the nickel shell, the SCF-supported Ag@Ni core–shell nanoparticles also presented a significant eddy current effect and anisotropic energy effect for the microwave absorption.

3.2.1.2. Cu-Ni composite as EM absorber. Bimetallic composite absorbers combining both the dielectric loss and magnetic loss type have shown an obvious advantage in balancing the complex relative permittivity and permeability.[89,214,215] Copper is a good dielectric loss material but has low stability, whereas nickel is a good magnetic loss material and is corrosion resistant but with low conductivity, therefore Cu–Ni hybrid nanostructures have synergistic advantages as electromagnetic absorption materials. For CuNi composite, the core-shell bimetallic materials would be easily produced based on separate reduction reactions in the heterogeneous nucleation. The standard reduction potential of nickel [$E^0(Ni^{2+}/Ni^0)$ = -0.257 V] is lower than that of copper [E^0 (Cu^{2+}/Cu^0) = 0.342 V].[216–218] Thus the copper is easier to be reduced in competitive redox reactions. Due to their widely differing redox potentials, Cu-Ni core-shell microstructure were generated via the reduction of Ni^{2+} at relative high temperature after the Cu core small particles generation at relative low temperature. It is noticed that the unique core-shell structure would induce interfacial polarization, which is beneficial for the electromagnetic absorption. Additionally, it is well anticipated that that the morphologies of bimetallic composites play a vital role in determining the microwave absorption performances of absorbers. Nowadays, the electromagnetic properties of core-shell Cu@Ni with various shapes, such as dendrite-like, rod-like, fishbone-like, and nanowire-like microstructures,[85,219–222] are widely investigated.

Wang et al.[221] fabricated various Cu/Ni molar ratios of bimetallic nanowires ($Cu_{13}@Ni_7$, $Cu_5@Ni_5$ and $Cu_7@Ni_{13}$) and nanospheres ($Cu_{13}@Ni_7$, $Cu_5@Ni_5$ and $Cu_1@Ni_3$) via facile reduction of hydrazine under similar reaction condition. Ni was incorporated into the Cu–Ni nanomaterials as a shell over the Cu core at low temperature. The RL of Cu@Ni samples was evaluated based on the complex relative permittivity and permeability. The results demonstrated that the electromagnetic absorption capacity greatly depended on the Cu/Ni molar ratio and morphology. The as-prepared Cu–Ni nanowires showed decreased RL values with increasing molar ratios of the Ni shell, however Cu–Ni nanospheres showed a reversed RL variation with the molar ratio of the Ni shell.

In our work,[220] dendrite-like and rod-like NiCu composites were prepared by a one-pot hydrothermal process at various reaction temperatures (120, 140, and 160 °C). The uniform and perfect dendrite-like NiCu obtained at 140 °C showed outstanding electromagnetic-wave absorption properties (Fig. 12). The lowest RL (RL) of -31.13 dB was observed at 14.3 GHz the bandwidth with the RL below -10 dB can reach 3.4 GHz (12.7-16.1 GHz) with a thickness of only 1.5 mm. The outstanding electromagnetic-wave-absorbing properties were ascribed to space-charge polarization arising from the heterogeneous structure of the NiCu composite, interfacial polarization between the CuNi and paraffin, and vibrating micro-current dissipation originating from the uniform and perfect dendrite-like shape.

In summary, For the CuNi as the microwave absorbing fillers, there existed at least three advantages in comparison with metallic Ni fillers. Firstly, due to the the high conductivity of bimetallic CuNi material, it is just required low amounts in the polymer matrix (such as paraffin and epoxy) to form conductive network to generate conduction loss under microwave irradiation. In addition, the ferromagnetic bimetallic NiCu connecting dielectric and magnetic losses can enhance electromagnetic-wave absorption. Second, because of the different redox potentials between Ni and Cu, the CuNi was easily expected to be formed core-shell structure. These core-shell structures can induce space-charge and interfacial polarization to dissipate microwave energy. Third, the Cu was prone to produce one dimensional structured CuNi materials, which can form a dissipation microcurrent and antenna receiver to absorb electromagnetic-wave energy.

3.2.2. Ni-polymer composite as EM absorber. Among the multifunctionalized micro/nanostructures, electromagnetic functionalized micro/nanostructures of conducting polymers, such as polypyrrole (PPy) and polyaniline (PANi), are of special interest due to their potential applications in electromagnetic wave absorbing materials with the features of controllable dielectric loss ability, ease of preparation, good environmental stability.[131,223–226] The addition of good dielectric performance of conductive polymers such as PPy and PANi together with magnetic performance of magnetite such as metal nickel (Ni) can effectively improve the EM wave absorption of composite sphere. Meanwhile, construction of a core/shell structure can further contribute to the additional dielectric loss, namely, interfacial dielectric relaxation.

Dong et al.[227] fabricated Ni/PANi nanocomposites by the chemical polymerization, and the electromagnetic properties were then investigated at 2-18 GHz. Notably, the authors stated that the permittivity of the Ni/PANi nanocomposite displayed dual dielectric relaxations with

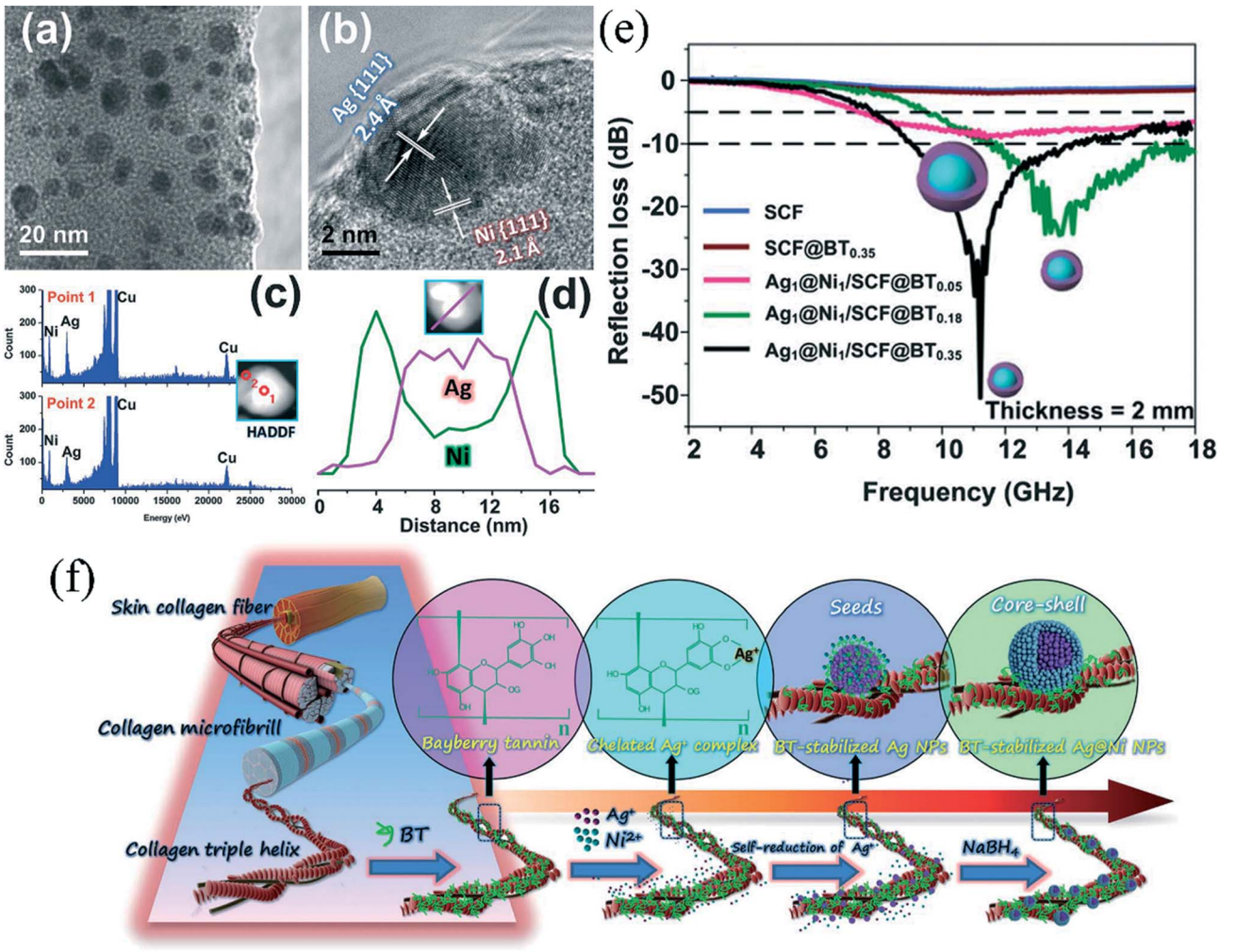

Fig. 11 (a) TEM image of Ag@Ni/ SCF-BT0.05 with molar ratio of Ag^{+}/Ni^{2+} at 1:1; (b) HRTEM images of an individual Ag@Ni core–shell NP; (c) EDX spectra recorded from the centre (top) and edge (bottom) regions of a single nanoparticle; (d) HAADF image and EDX cross-sectional compositional line profiles of a single nanoparticle; (e) RL of comparison of microwave RLes of the SCF, SCF-BT0.35, and $Ag_1@Ni_1/SCF\text{-}BT_x$ (x = 0.05,0.18, and 0.35) with the thickness of 2 mm; (f) Schematic diagram showing the preparation mechanism of the one-step seeding growth of Ag@Ni core–shell NPs on skin collagen fiber. (Reprinted with permission from Ref. [213]. Copyright 2012, Royal Society of Chemistry.)

increasing content of PANi to over 15.6 wt%. This was ascribed to a cooperative consequence of the core/shell interfaces and the dielectric PANi shells. Moreover, the permeability showed a strong natural resonance around 2-8 GHz, which contributed to electromagnetic wave magnetic loss. The proper matching of the permittivity and the permeability was beneficial to the enhancement of electromagnetic absorption. Xu et al.[139] prepared micro-structured Ni/PPy core/shell composites through an in situ chemical oxidative polymerization of pyrrole (Py) monomer in the presence of Ni powder. The permeability of Ni/PPy composites presented a natural magnetic resonance at 6.0 GHz. Electromagnetic absorption less than -10 dB was found for Ni/Py = 4:1 (11-15.4 GHz) and Ni/Py = 2:1 (12-17.5 GHz). The ternary Debye relaxations for enhanced dielectric loss induced by PPy coatings and proper electromagnetic impedance matching due to the synergetic consequence of the Ni cores and PPy shells contributed to the improvement of the electromagnetic absorption of the Ni/PPy core/shell composites.

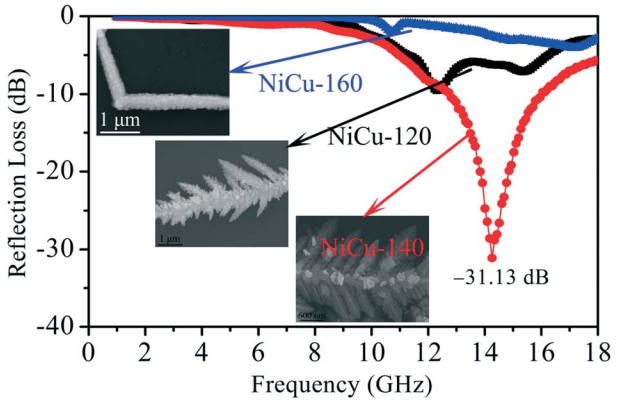

Fig. 12 RL curves of NiCu-120 (dendrites), NiCu-140 (dendrites) and NiCu-160 (rods) paraffin composite with 40 wt% loadings with the thickness of 1.5 mm. (Reprinted with permission from Ref. [220]. Copyright 2015, American Chemical Society.)

Li et al.[228] stated polystyrene@polypyrrole (PS@PPy) composite spheres with well-defined core/shell structure were synthesized via an in situ chemical oxidative copolymerization of pyrrole (Py) and N-2-carboxyethylpyrrole (PyCOOH) templated by PS microspheres. Then, by proper introducing PyCOOH as the comonomer, the authors got uniform and complete PS@P(Py-PyCOOH)@Ni core/shell structures through an in situ oxidative polymerization followed by the electroless plating process. The electroless plating method can effectively increase the incorporation contents of Ni onto the PS@P(Py-PyCOOH) microspheres, which can be confirmed from Fig. 13 (a-c). The formation of uniformed Ni shell structure enhanced the absorption performance. The electromagnetic absorption less than −10 dB was found in 9.16−13.75 GHz range for the PS@P(Py-PyCOOH$_{50}$)@Ni composite microspheres with the minimum RL reached -20.06 dB at 10.69 GHz, as shown in Fig. 13d. Moreover, the RL peaks transferred steady from the low-frequency to high frequency range with the increasing PyCOOH content from 0 to 50%.

3.2.3. Ni-semiconductor composite as EM absorber. As above mentioned, Ni would generate eddy current induced by microwave in GHz range because of high conductivity. The eddy current could lead to impedance mismatching between the materials and air space, which could increase microwave reflection and decrease microwave absorption. This problem is a challenge to the researchers. Therefore, in order to optimize microwave absorption ability, an efficient strategy is to cover the magnetic Ni particles by an inorganic and nonmagnetic coating to create a core/shell microstructure. Especially, for the semiconductor shell, which not only can bring dielectric loss and good impedance match, but also can induce additional absorption mechanism because of similar energy band with microwave as well as providing protective shell, has stimulated numerous interests. It is well supposed that the semiconductor could be categorized in oxide semiconductor and non-oxide semiconductor. Thus, we will classify this section into two topics: electromagnetic absorption of Ni/oxide semiconductor and electromagnetic absorption properties of Ni/non-oxide semiconductor.

3.2.3.1. Ni/oxide semiconductor composite as EM absorber. There are numerous publications about electromagnetic absorption properties of Ni/oxide semiconductor composite, such as Ni@SiO_2,[95,229] Ni@ZnO,[118,230–233] Ni@TiO_2,[234–237] Ni@CuO,[86,238] Ni@Al_2O_3,[27,239–242] Ni@MnO_2,[243–245] Ni@Ni_2O_3,[246,247] and Ni@SnO_2[87,90,94,108,157,158,178] composites. In these kind of core-shell Ni based composites, the magnetic materials acted as cores, which enhance the permeability of the composites, result in the increase of the magnetic loss. The dielectric materials as shells, which acts not only as a center of electric polarization but also as an insulating matrix between the magnetic particles, give rise to the enhanced dielectric loss and good impedance match.

3.2.3.1.1. Ni@SiO_2 composite. Gong et al.[229] fabricated Ni/SiO_2 nanocomposites with tunable composition by a facile one-step wet chemical process. The results showed that the magnetic and electromagnetic properties of the core-shell Ni@SiO_2 hybrid materials were all highly associated with SiO_2 content. Because of the enhanced interfacial polarization between Ni and SiO_2 nanoparticles and the magnetic resonance phenomenon, the as-obtained Ni/SiO_2 nanocomposites with an appropriate content of SiO_2 presented dramatically enhanced

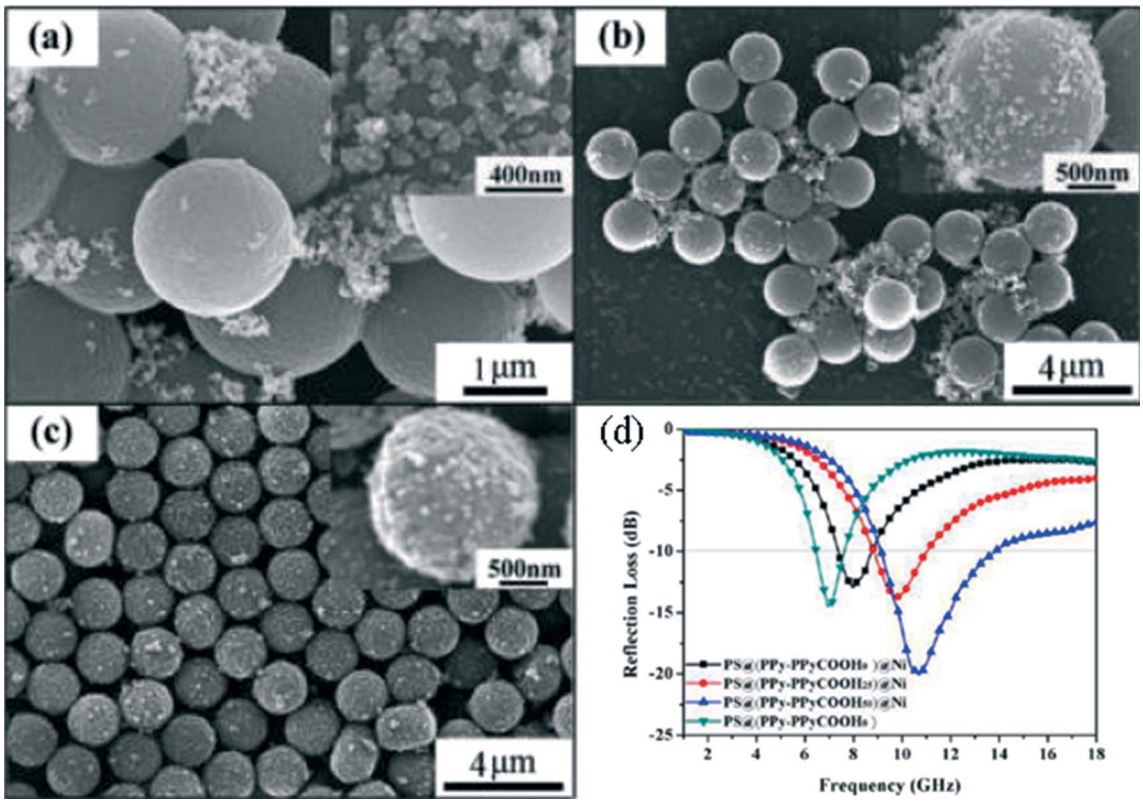

Fig. 13 SEM images of (a) PS@P(Py-PyCOOH$_0$)@Ni, (b) PS@P(Py-PyCOOH$_{25}$)@Ni and (c) PS@P(Py-PyCOOH$_{50}$)@Ni core/shell microspheres; (d) Calculated RL of PS@P(Py-PyCOOH$_{0,25,50}$)@Ni and PS@P(Py-PyCOOH$_0$) composite spheres. (Reprinted with permission from Ref. [228]. Copyright 2013, American Chemical Society.)

magnetic loss and dielectric loss as well as suitable electromagnetic match, showing promising potential as electromagnetic absorbents.

We also prepared the amorphous SiO_2-coated Ni composite microspheres and also investigated their electromagnetic properties.[95] Thanks to the presence of the insulator SiO_2 shell, the core-shell Ni@SiO_2 composites displayed better antioxidation capability than that of pure Ni microspheres (Fig. 14a). For the EM properties of Ni@SiO_2 composite microspheres, an optimal RL (RL) as low as -40.0 dB (99.99% absorption) was observed at 12.6 GHz with an absorber thickness of only 1.5 mm. The effective absorption (below -10 dB, 90% electromagnetic wave absorption) bandwidth can be tuned between 3.1 GHz and 14.4 GHz by tuning the absorber thickness in the range of 1.5-4.5 mm (Fig. 14b). The excellent electromagnetic wave absorption abilities of Ni@SiO_2 composite microspheres are attributed to a higher attenuation ability, Debye relaxation, interface polarization of the core-shell structure and synergistic effects between high dielectric loss and high magnetic loss.

3.2.3.1.2. Ni@ZnO composite. ZnO nano-structural materials may have potential applications in electromagnetic wave absorbing materials because of the light weight and semiconductive properties, and its facile mass synthesis can be easily realized.[76,248–250] Therefore, when the Ni particles were coated by ZnO shell, the electromagnetic properties of Ni may be enhanced, correspondingly. Liu et al.[233] prepared Ni/ZnO nanocapsules through a modified arc-discharge technique, and the electromagnetic characteristics of Ni/ZnO nanocapsules were investigated at 2-18 GHz. The dual nonlinear dielectric resonance and strong natural resonance at 16.6 GHz made a contribution to excellent electromagnetic absorption. The RL below -20 dB could be found in 14-18 GHz for an absorber thickness of 2.05 mm. The equivalent circuit model was applied to describe the dual nonlinear dielectric resonance, which was attributed to a cooperative consequence of the core/shell interfaces and the dielectric ZnO shells.

The effect of ZnO morphology on the electromagnetic properties of Ni/ZnO was investigated by our group.[230] Three different morphologies of Ni/ZnO composites were successfully prepared by a hydrothermal method. The morphologies of ZnO nanostructures can be readily controlled by adjusting the amounts of $NH_3{\cdot}H_2O$ (Fig. 15a), and the ZnO morphology played a significant influence on the electromagnetic absorption properties. The core-shell structured Ni/ZnO with polyhedron ZnO coating showed significantly higher dielectric loss, magnetic loss and excellent absorption properties in comparison with the other two Ni/ZnO composites. The maximum microwave loss was -48.6 dB at 13.4 GHz with the thickness of 2.0 mm (Fig. 15b), and the bandwidth with RL less than -10 dB can reach 6.0 GHz. The excellent microwave-absorption properties mainly resulted from the efficient cooperation between dielectric loss and magnetic loss, large attenuation constant, as well as the multipolarization of the core/shell interface.

Wang et al.[118] fabricated flower-like ZnO coated by Ni nanoparticles by the reduction of NiO coated ZnO produced via an atomic layer deposition (ALD) method. The structure and electromagnetic (EM) absorption properties of the as-prepared samples were investigated. The as-prepared ZnO@Ni composites showed superior EM wave absorbing characteristics in comparison with those of ZnO. The effective absorption bandwidth below -10 dB reached 5.3 GHz for ZnO@Ni with a thickness of only 1.5 mm. Furthermore, when the match thickness was 2.0 mm, the minimum RL was -48.0 dB at 10.4 GHz, as shown in Fig. 16. The excellent absorption ability of ZnO@Ni composites resulted from the integration of multiple dielectric-magnetic loss induced by the unique structure.

3.2.3.1.3. Ni@TiO_2 composite. Nowadays, titanium dioxide (TiO_2), a classical and important metal oxide, has been widely used in electromagnetic absorption.[30,82,251–255] For instance, Chen et al.[251] reported hydrogenated TiO_2 is an excellent electromagnetic properties candidate benefiting from a collective-movement-of-interfacial dipole mechanism which induces the collective interfacial polarization amplified electromagnetic absorption. Liu and co-workers have synthesized composite microspheres with Fe_3O_4 cores and hierarchical TiO_2 shells and the Fe_3O_4@TiO_2 core–shell microspheres exhibited a much lower RL and wider absorption frequency range than pure Fe_3O_4.[15] Chen and co-workers have successfully prepared Fe_3O_4/TiO_2 core/shell nanotubes with excellent electromagnetic wave dissipation properties.[256] The main characteristic feature of the TiO_2 is that it is dielectric loss material, while the dominant dipolar polarization and the associated relaxation phenomena contributed to the loss mechanisms. Thus, combined magnetic Ni with dielectric TiO_2, we could obtain enhanced electromagnetic absorption properties of Ni/TiO_2 composite.

In our study,[237] core-shell microspheres with Ni cores and two phases of TiO_2 (anatase, rutile) were prepared via solvothermal synthesis and an annealing process, in Fig. 17(a-d). The oxidation resistance of the rutile TiO_2-coated Ni composite was better than that of the pure Ni microsphere. Compared with pure Ni, the electromagnetic absorption

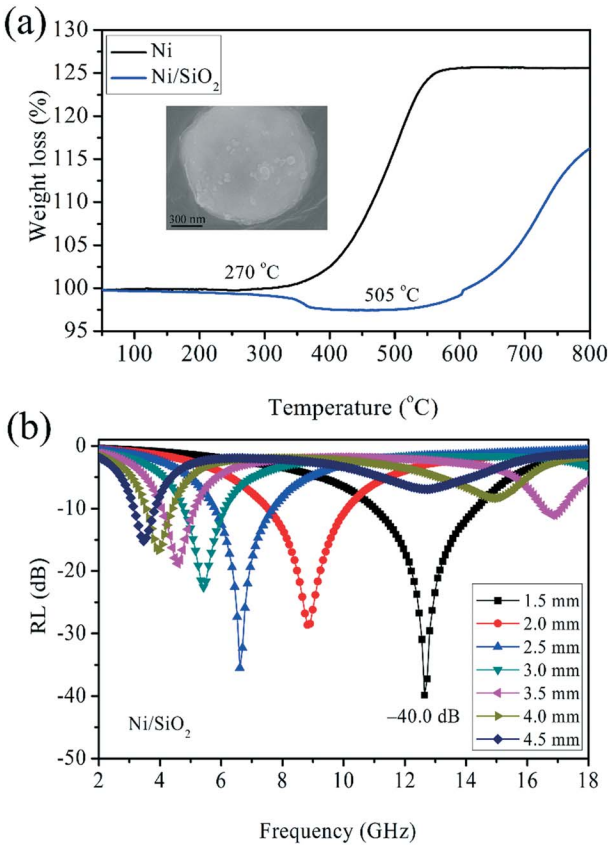

Fig. 14 (a) TG patterns of the Ni and Ni@SiO_2 composite microspheres; (b) RL curve of Ni@SiO_2 paraffin composites with different absorber thicknesses; Inset is SEM of core-shell Ni@SiO_2 composite. (Reprinted with permission from Ref. [95]. Copyright 2015, Royal Society of Chemistry.)

properties can be significantly enhanced no matter coating with anatase or rutile TiO_2 shells. Among the two core–shell structural Ni@TiO_2 composites, rutile TiO_2 coated Ni (Ni-R) displayed better electromagnetic absorption ability, in Fig. 17(e,f). The minimum RL of Ni-R composite microspheres with a thickness of 1.8 mm reached -38.0 dB at 11.1 GHz, and the absorption bandwidth with RL below -10 dB was 9.5 GHz when considering thicknesses of 1.0-2.5 mm. The enhanced absorption capability arose from the efficient complementarities between the magnetic loss and dielectric loss, multiple interfacial polarization, high thermal conductivity of rutile TiO_2 and microwave attenuation capability.

We also prepared the core–shell Ni/ anatase TiO_2 with tunable crystal structure of TiO_2 at various solvothermal reaction times.[235] The electromagnetic absorption performances of Ni/TiO_2 composites were influenced by the crystallinity of TiO_2 shells. The Ni/TiO_2 prepared at 36 h exhibits the best electromagnetic absorption properties, which was attributed to good impedance match and high thermal conductivity. The minimum RL was -16.9 dB at 14.1 GHz and the absorption bandwidth with RL below -10 dB was up to 2.4 GHz (from 13.1 to 15.5 GHz) for a thickness of 2.5 mm. Furthermore, we fabricated core–shell Ni/anatase TiO_2 heterostructures at different contents of TBOT.[236] The amount of TiO_2 played a vital role on the electromagnetic absorption properties of Ni/TiO_2 composite. The Ni/TiO_2 composite prepared at 2.0 mL TBOT exhibited strong EM absorption properties (RL below -10 dB) in the 4.5-17.7 GHz range with corresponding absorber thicknesses of 1.5-4.0 mm. The excellent electromagnetic absorption properties were due to the proper complementarities between magnetic loss and dielectric loss, geometrical effect, the natural resonance and multiple polarization.

3.2.3.1.4. Ni@CuO composite. Liu et al.[238] reported CuO/Cu_2O-coated Ni nanocapsules with Ni nanoparticles as cores and amorphous CuO/Cu_2O as shells were synthesized by the arc discharge method. The dielectric relaxation of the CuO/Cu_2O shell and the interfacial relaxation between the CuO/Cu_2O shell and the Ni core lead to dual nonlinear dielectric resonance. The authors found that the RL less than -20 dB can reach at 2.0-18.0 GHz with a thickness between 1.0 and 8.4 mm for paraffin-nanocapsule composites, consisting of 40 wt% Ni nanocapsules, and an optimal RL value of -47.8 dB was observed at 14.4 GHz on a specimen with a matching thickness of 1.20 mm. The frequency of the microwave absorption complied with the quarter-wavelength matching model.

We synthesized hierarchical heterostructure of Ni microspheres-CuO nano-rices using a simple two-step process, and the CuO rices were densely deposited on the surfaces of Ni microspheres (Fig. 18(a,b)).[86] The core-shell rice-like CuO-coated Ni exhibited better anti-oxidation capability than pure Ni due to the presence of the barrier effect of the CuO shell. In comparison with pristine Ni microspheres and CuO nano-rices, the Ni-CuO composites exhibited better electromagnetic absorption properties. Moreover, the amount of CuO played a vital role in the electromagnetic dissipation ability of Ni-CuO composites. The Ni-CuO heterostructures prepared at 0.017 M Cu^{2+} showed the best electromagnetic wave absorption capabilities. A minimum RL reached -62.2 dB at 13.8 GHz with the thickness of only 1.7 mm (Fig. 18c). The effective absorption (below -10 dB) bandwidth can be tuned between 6.4 GHz and 18.0 GHz by tuning the absorber thickness of 1.3-3.0 mm.

3.2.3.1.5. Ni@Al_2O_3 composite. Recent interest has been devoted to ferromagnetic-metal/Al_2O_3 nanocomposites, which can be

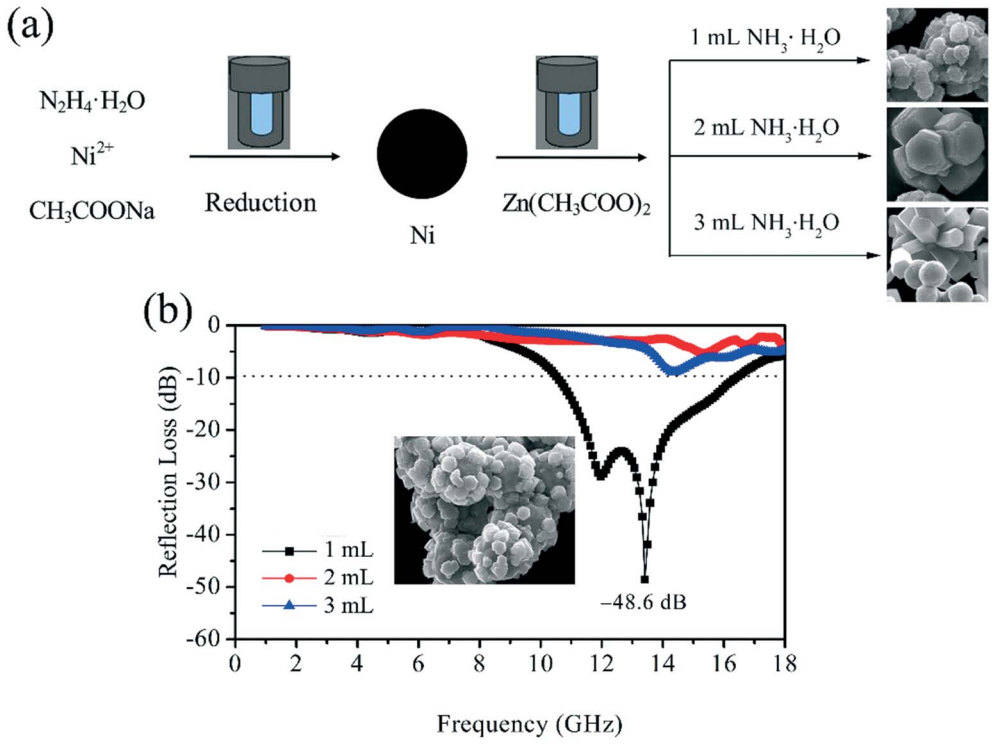

Fig. 15 (a) Schematic illustration of formation of various morphologies of Ni/ZnO composites; (b) Frequency dependences of RL (RL) with the thickness of 2.0 mm for the three Ni/ZnO composites; Inset is the SEM image of Ni/ZnO composite prepared at 1.0 mL $NH_3 \cdot H_2O$. (Reprinted with permission from Ref. [230]. Copyright 2015, Elsevier B.V.)

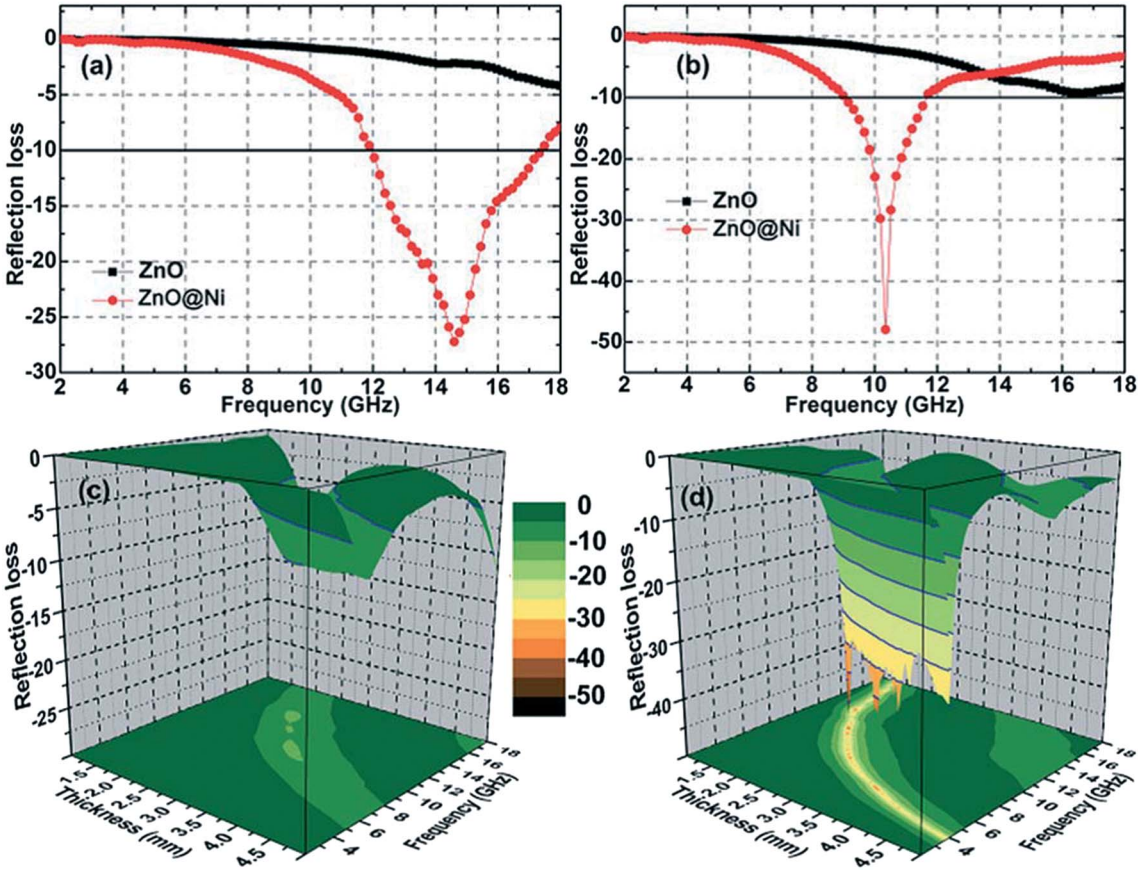

Fig. 16 RL curves of the product/paraffin composites with a thickness of (a) 1.5 mm and (b) 2 mm in the frequency range of 2-18 GHz; Three dimensional representations of RL of (c) ZnO and (d) ZnO@Ni. (Reprinted with permission from Ref. [118]. Copyright 2015, Royal Society of Chemistry.)

used as high-efficiency electromagnetic absorption materials due to the introduction of insulating Al_2O_3,[214,257] which suppressed the eddy-current effect. Xu et al.[239] prepared Ni/Al_2O_3 nanocomposites by the mechanochemical synthesis method. The annealing process enlarged the grain size of both the metal Ni and insulating Al_2O_3 and lead to an increase of the saturation magnetization and a decrease of the surface anisotropy. An optimal RL of -23 dB was obtained in the as-milled nanocomposite at 17.8 GHz for an absorber thickness of 6.6 mm. The annealed sample exhibited a RL below -20 dB in the whole *K*u-band for an absorber thickness of 6.6-9.7 mm with an optimal RL of -54.7 dB at 13.2 GHz for a layer thickness of 9.3 mm. The excellent electromagnetic-absorption properties were a consequence of a proper match of the dielectric and magnetic losses.

We fabricated the core-shell composite microspheres with Ni cores and Al_2O_3 nanoflake shells by a hydrothermal deposition method (Fig. 19(a-c)).[240] A significant enhancement of electromagnetic absorption (EMA) performance of Ni microspheres coated by the alumina shells was achieved over the 1–18 GHz. The RL (RL) less than −10 dB of the composite was obtained over 7.5–18.0 GHz by tuning the sample thickness between 1.3 and 2.2 mm, and an optimal RL of -33.03 dB was obtained at 9.2 GHz with a thin absorber thickness of 2.0 mm (Fig. 19d). The coating of the dielectric alumina shell significantly enhanced the EM absorption performance due to the enhancement of interface polarization between the metals and dielectric interfaces, the synergetic effect between the dielectric loss and magnetic loss and unique flake–like dielectric alumina.

Yan et al.[27] used atomic layer deposition (ALD) to fabricate coaxial multi-interface hollow Ni-Al_2O_3-ZnO nanowires (Fig. 20(a-f)). The morphology, microstructure, and ZnO shell thickness dependent electromagnetic and microwave absorbing properties of these Ni-Al_2O_3-ZnO nanowires were analyzed. Excellent electromagnetic wave absorbing properties with a minimum RL of about -50 dB at 9.44 GHz could be observed for the Ni-Al_2O_3-100ZnO nanowires, which was 10 times of Ni-Al_2O_3 nanowires. The electromagnetic absorption frequency could be effectively varied by simply adjusting the number of ZnO deposition cycles. The absorption peaks of Ni-Al_2O_3-100ZnO and Ni-Al_2O_3-150ZnO nanowire shifted of 5.5 and 6.8 GHz towards lower frequencies, respectively (Fig. 20(g-i)). The enhanced electromagnetic wave absorption originated from multiple loss mechanisms caused by the unique coaxial multi-interface structure, such as multi-interfacial polarization relaxation, natural and exchange resonances, as well as multiple internal reflections and scattering.

3.2.3.1.6. Ni@MnO_2 composite. Tang et al.[245] investigated the electromagnetic properties of MnO_2 coated nickel particles with submicron size. In their work, nickel particles with submicron size were prepared by using the solvothermal method. Then, these spheres were coated with a layer of MnO_2 using the soft chemical method. The composites possessed a classical core/shell structure with the MnO_2 superficial

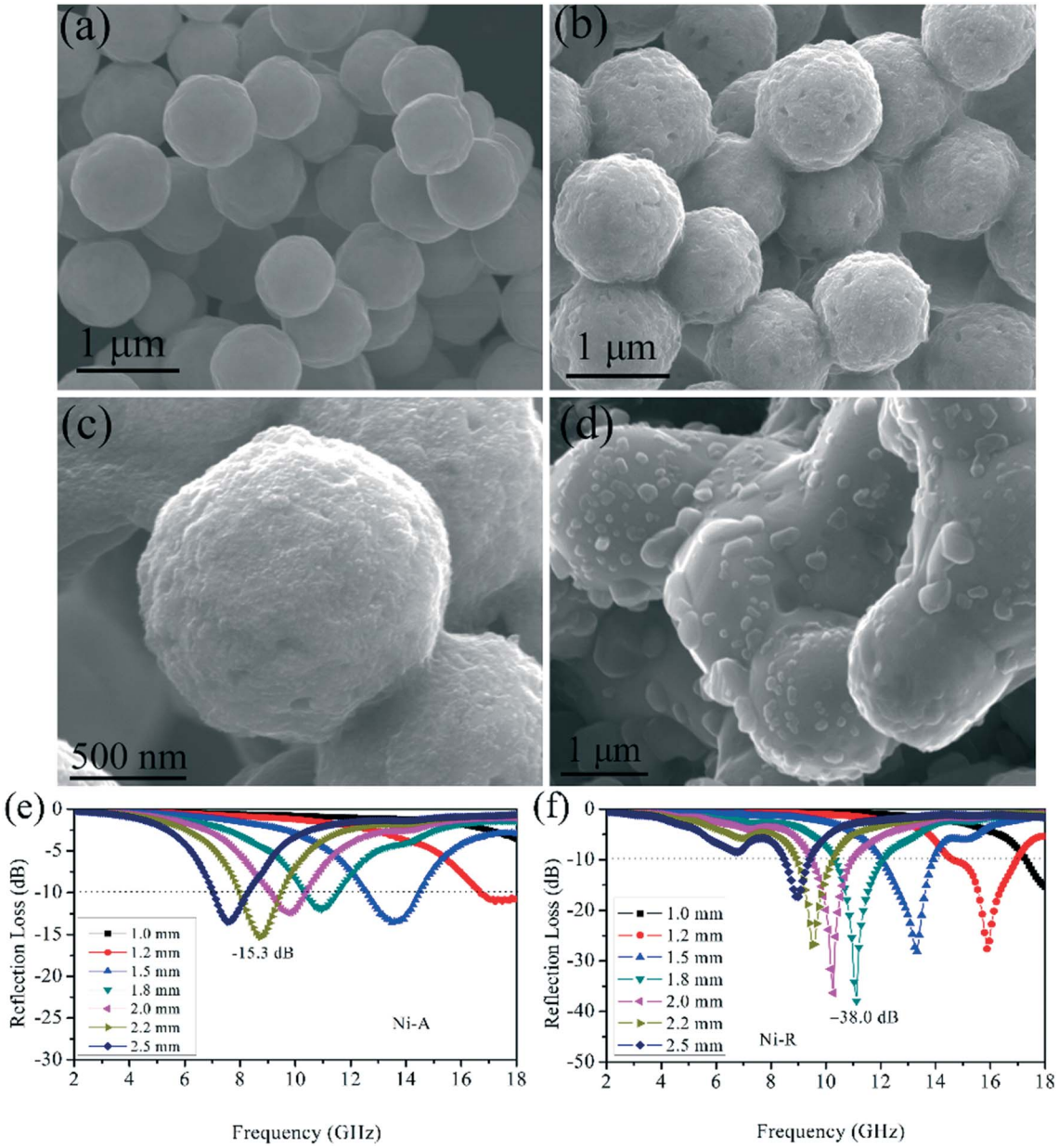

Fig. 17 (a) SEM images of Ni microspheres, (b, c) SEM images of Ni-A composite and (d) SEM image of Ni-R composite; Simulation of RL of (e) Ni-A and (f) Ni-R paraffin-composite with different thicknesses vs. frequency. (Reprinted with permission from Ref. [237]. Copyright 2015, Royal Society of Chemistry.)

layer, no more than 10 nm in thickness. As for electromagnetic properties, the core-shell composites had a rather small and stable permittivity in the frequency range of 2-18 GHz. These powders also presented a very stable real component of complex permeability. The well coated feature of the submicron Ni/MnO_2 particles contributed to these electromagnetic characteristics. Moreover, Ni/MnO_2 powders exhibited desirable electromagnetic matching, which could be enhanced through the structural modulation, such as changing core size or shell thickness.

Huang et al.[243] reported that the Ni nanoplatelets with an average diameter of 75 nm and an average thickness of 10 nm were coated with MnO_2 through a simple solution phase chemical method. The MnO_2-coated Ni nanoplatelets were dispersed in paraffin wax to form the composite samples of the magnetic filler dispersed in the nonmagnetic insulating matrix. The effect of the Ni nanoplatelet volume fraction on the complex permittivity, complex permeability, and electromagnetic absorption of the composites were studied in the frequency range of 0.1–10 GHz. The complex permittivity of the composites with different volume fractions of the Ni nanoplatelets was almost constant in the 0.1-10 GHz frequency range. The complex permeability of the composites showed several resonance peaks. Besides the natural resonance peak, the exchange resonance peaks were also observed. The composite with 17% volume fraction of Ni nanoplatelets presented excellent electromagnetic absorption properties with a minimum RL value -31 dB at 9.1 GHz for a thickness of 2 mm and a broad absorption bandwidth of 2.3-10 GHz ($R < -10$ dB). For the Ni nanoplatelet composites, the magnetic loss was the dominant term for microwave absorption.

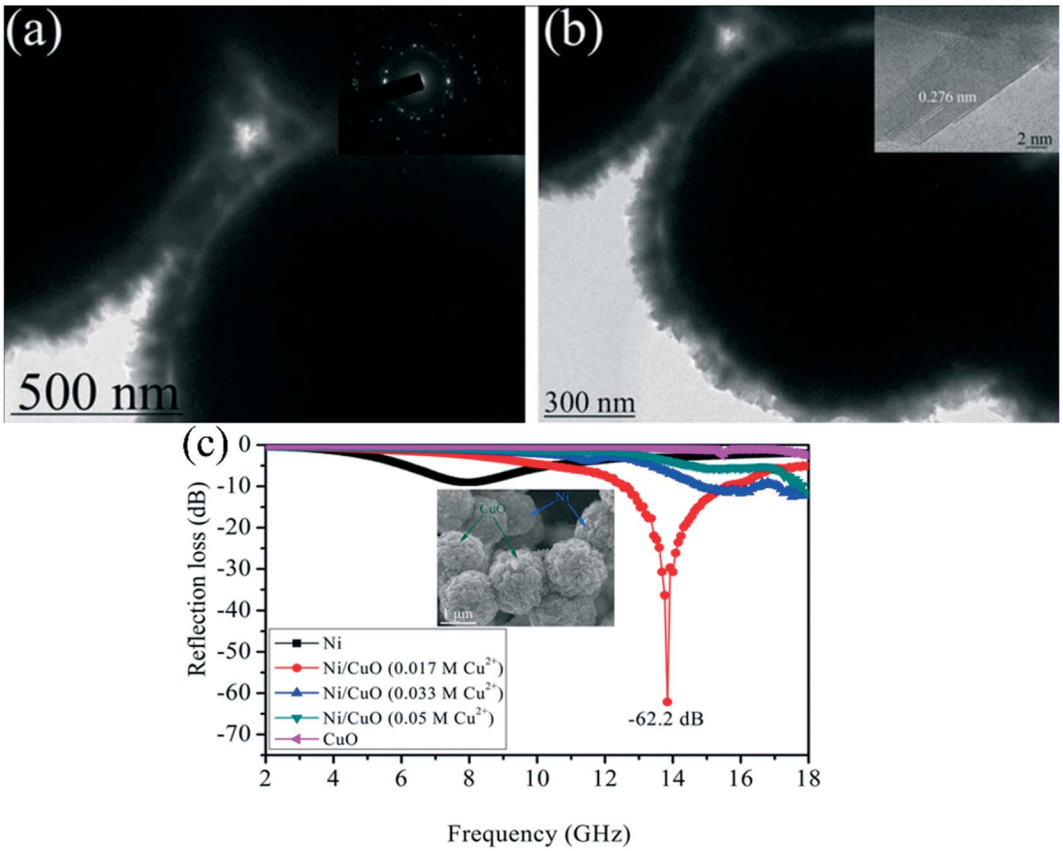

Fig. 18 TEM and HRTEM images of the as-prepared Ni-CuO structures: (a) low magnification, inset of (a) shows the SAED pattern; (b) high magnification; inset of (b) shows the HRTEM. (c) Comparison of RLes of the five as-obtained samples with a thickness of 1.7 mm; inset of (c) shows the SEM of Ni/CuO. (Reprinted with permission from Ref. [86]. Copyright 2015, Royal Society of Chemistry.)

3.2.3.1.7. $Ni@Ni_2O_3$ composite. Liu et al.[246] fabricated the microporous Ni nanoparticles (NPs) of 22 nm by chemical dealloying method. During the passivation process, the microporous Ni NPs covered with NiO shell were generated as the result of surface oxidation. The unique architectures of the microporous morphology, core/shell structure and nanostructure (very fine crystalline) remarkably improved the electromagnetic wave absorption properties. The microporous Ni/NiO sample showed a much higher dielectric loss between 2 and 18 GHz and a higher magnetic loss above 10 GHz than those of the nonporous counterpart. It exhibited high electromagnetic wave absorption properties with a minimum RL value of -49.1 dB and a wide absorption bandwidth of 5.8 GHz (Rl ≤ -10 dB).

Wang et al.[247] reported the enhanced electromagnetic absorbing properties of the $Ni@Ni_2O_3$ core-shell soft magnetic particles synthesized by a hydrogen peroxide oxidation method, as shown in Fig. 21. Complex electromagnetic parameters (permittivity and permeability) of the paraffin mixed composite were measured in the frequency range of 0.1-18 GHz. Compared with the Ni/paraffin composite, the apparent electrical resistivity of $Ni@Ni_2O_3$/paraffin composite increased and the permittivity decreased dramatically. The RL of the composite below -20 dB in the frequency range of 4.0-12.6 GHz were obtained with the absorber thicknesses of 1.8-4.3mm, while an optimal RL of -53.5 dB was obtained at 7.9 GHz for the thickness of 2.5 mm. The good microwave absorption properties was attributed to suitable impedance match as a consequence of the insulator Ni_2O_3 shell around Ni particles. Quantitative calculation indicated that not only the RL peak position but also the number of the peaks complied with the quarter-wavelength matching model.

3.2.3.1.8. $Ni@SnO_2$ composite. As an n-type wide-bandgap (E_g = 3.6 eV) semiconductor, SnO_2 is one of the most intensively studied materials, which are potentially used in a variety of applications in chemical, optical, electronic, and mechanical fields, due to its unique high conductivity, chemical stability, photoluminescence, and gas sensitivity.[258–262] Thus, it may be a promising electromagnetic absorption material,[140,263] which is similar with semiconductor ZnO absorbers. In our group, we used the hydrothermal deposition method to prepared core-shell structured Ni/SnO_2 composites, and the amounts of SnO_2 nanaoshells can be tuned by control of precursor.[157,158,178] Compared with pure Ni microspheres, the core-shell $Ni@SnO_2$ composites exhibited enhanced electromagnetic absorption capabilities. The outstanding electromagnetic properties were attributed to good electromagnetic impedance match, geometrical factors, cooperation effect between magnetic loss and dielectric loss, multi-resonance and interfacial polarization of the core-shell structures. Moreover, the porous hollow Ni/SnO_2 hybrids were also prepared by a facile two-step approach composed of solution reduction and subsequent reaction-induced acid corrosion, and the hydrothermal temperature exerted a vital influence on the phase crystal and morphology of Ni/SnO_2 hybrids.[87] The porous Ni/SnO_2 hybrid composites exhibited superior electromagnetic absorption properties in comparison

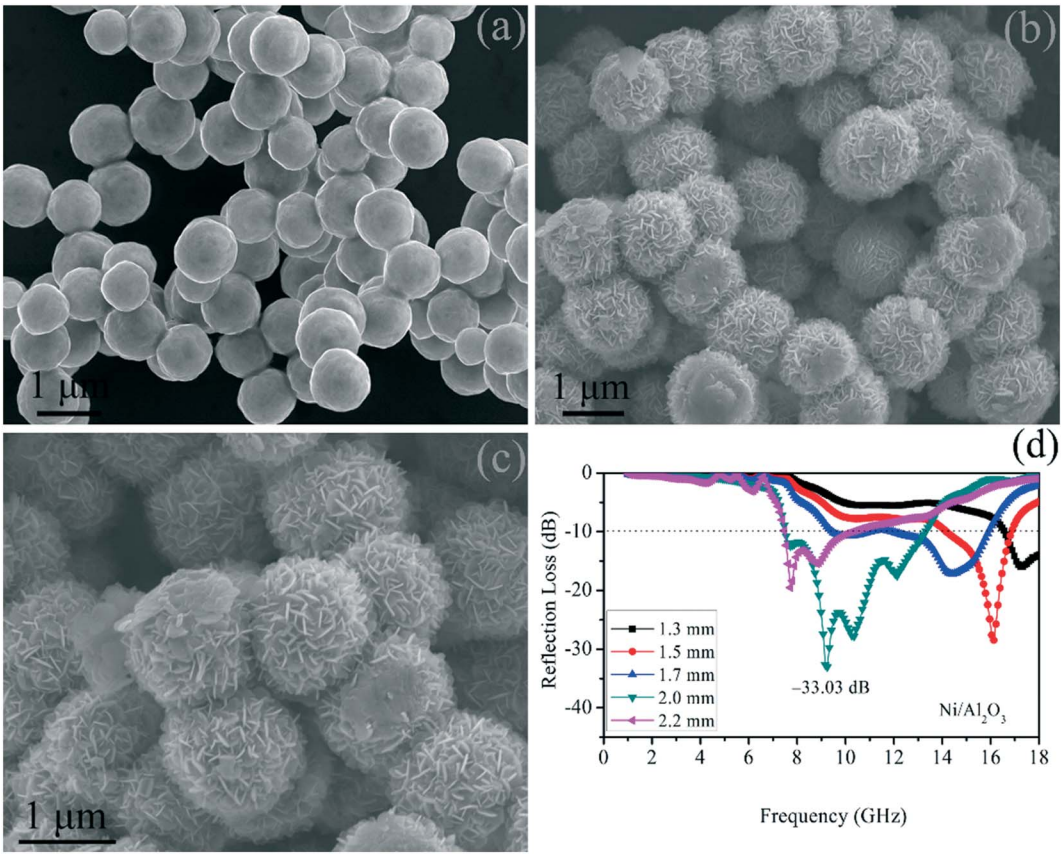

Fig. 19 (a) SEM image of the Ni microspheres, (b,c) SEM image of Ni/Al_2O_3 composite particles, (d) Frequency dependence of the RL for the paraffin matrix composites containing 40 wt% Ni/Al_2O_3 with different thicknesses. (Reprinted with permission from Ref. [240]. Copyright 2014, Royal Society of Chemistry.)

with pure Ni microspheres. The outstanding electromagnetic absorption performances could be observed for the hollow porous Ni/SnO_2 hybrid prepared at 200 °C. The minimum RL was -36.7 dB at 12.3 GHz and effective electromagnetic wave absorption band (RL< -10 dB, 90% microwave attenuation) was in the frequency range of 10.6-14.0 GHz with the thin thickness of 1.7 mm. The excellent electromagnetic absorption properties were due to the good impedance match, much more interfacial polarization and unique hollow porous structures, which could result in microwave multi-reflection and scattering.

As expected, the morphology vitally affected the electromagnetic absorption performance of absorbers. By analysis of the above mentioned EM properties of Ni/SnO_2, one can find that we just focused on the SnO_2 nanospheres as shell. To observe the effect of shell morphology change on the EM properties of Ni/SnO_2 composite, we prepared a novel heterostructure composed of SnO_2 nanorods grown on a Ni submicron sphere by a simple two-step method (Fig. 22 (a-c)).[90] SnO_2 nanorods were perpendicularly grown on the surfaces of Ni spheres and the density of the SnO_2 nanorods could be tuned by simply varying the addition amount of Sn^{2+} in this process. When the coverage density of SnO_2 nanorod was in an optimum state (diameter of 10 nm and length of about 40-50 nm), the optimal RL (RL) of electromagnetic wave was -45.0 dB at 13.9 GHz and the effective bandwidth (RL below -10 dB) could reach 3.8 GHz (12.3-16.1 GHz) with the absorber thickness of only 1.8 mm (Fig. 22d). In this work, SnO_2 nanorods played at least three roles in ameliorating electromagnetic wave absorption properties. Firstly, introducing SnO_2 into this system can tune the complex permittivity of Ni/SnO_2 composites to improve impedance match. Secondly, the core-shell structure between nickel and SnO_2 can cause additional space charge polarization and interfacial polarization, as shown in Fig. 22e, which was beneficial for enhancing microwave absorption. Thirdly, the SnO_2 nanorods were supposed to consider as antenna receiver to allow more microwave enter interior of absorber.

Yolk−shell structures are regarded as typical structures of microwave absorbers due to their multiple reflection and scattering dissipations. A yolk-shell structure with a cavity is a distinctive kind of core−shell structure,[183,264–267] which has specific advantages of low density, designable interspace, large surface area, and functional interfaces. Compared with core-shell structures, the specific yolk-shell structures used as electromagnetic absorbers presented much superiority, such as lightweight, tunable dielectric properties, multiple reflection and scattering, which satisfy the current requirement of absorbers (lightweight, thin thickness, high absorption and wideband). It is reported that yolk-shell structured $Fe_3O_4@TiO_2$,[266] $Fe_3O_4@ZrO_2$,[267] $Fe_3O_4@SnO_2$,[183] and Fe_3O_4@copper silicate [265] exhibited enhanced electromagnetic absorption properties compared with pristine Fe_3O_4 microspheres. Thus, we fabricated yolk-shell $Ni@SnO_2$ composites with designable interspace by a simple acid etching hydrothermal method. The unique yolk-shell $Ni@void@SnO_2$ shows outstanding electromagnetic wave absorption properties. The minimum RL

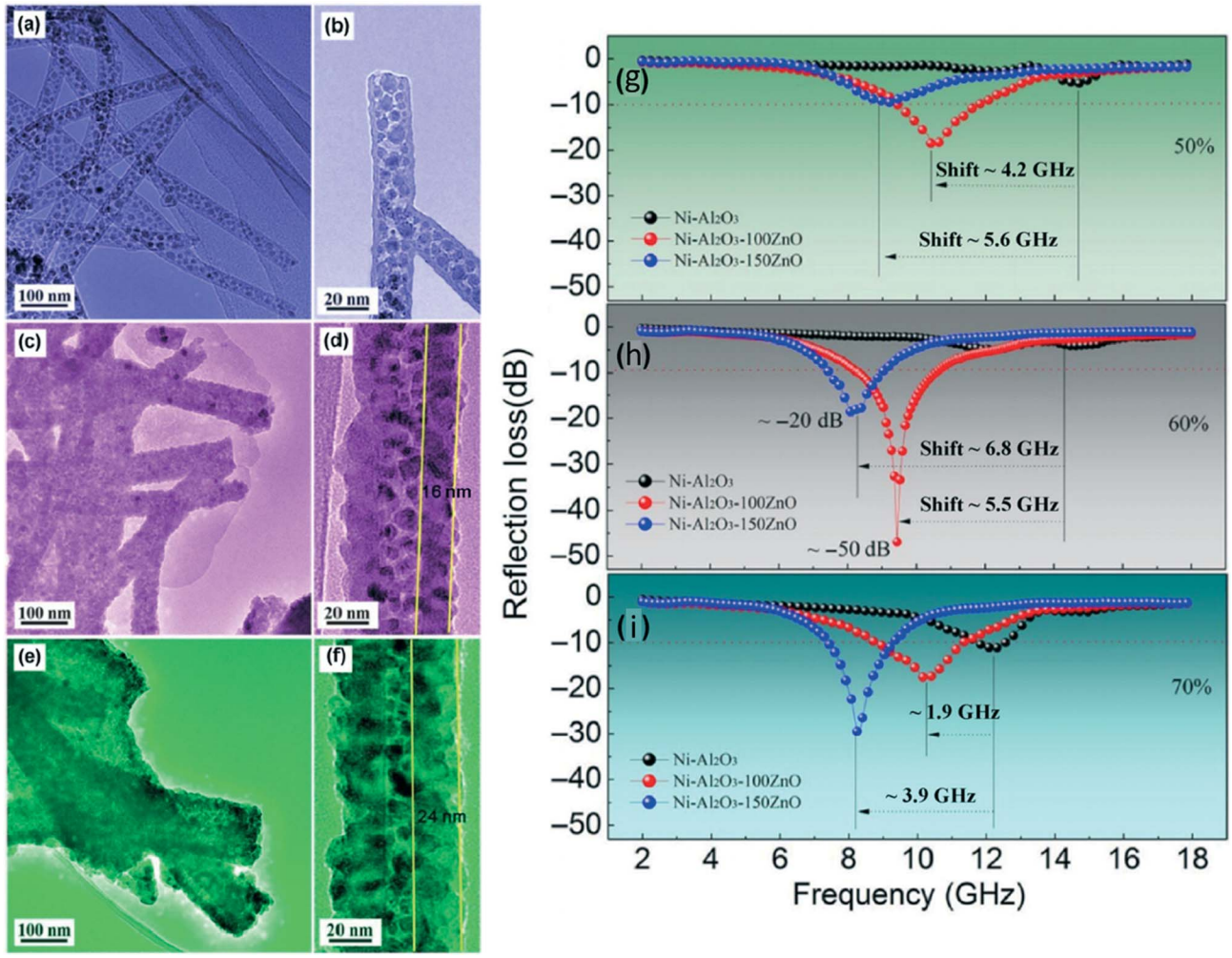

Fig. 20 TEM images of the Ni-Al_2O_3 and Ni-Al_2O_3-*x*ZnO nanowires obtained by sequential deposition of 20 cycles of Al_2O_3, different cycles of ZnO, and then a hydrogen reduction step, (a) and (b) 0, (c) and (d) 100, and (e) and (f) 150 cycles of ZnO; RL curves of Ni-Al_2O_3 and Ni-Al_2O_3-*x*ZnO nanowires with (g) 50 wt%, (h) 60 wt%, and (i) 70 wt% loading at a thickness of 2.43 mm. (Reprinted with permission from Ref. [27]. Copyright 2017, Springer.)

of -50.2 dB can be achieved at 17.4 GHz with a thickness of 1.5 mm (Fig. 23). The outstanding electromagnetic wave absorption properties resulted from unique yolk-shell structure. These yolk-shell structures can tune dielectric properties of Ni@air@SnO_2 composite to achieve good impedance matching. Moreover, the designable interspace could induce interfacial polarization, multiple reflection and microwave plasma.

Furthermore, we also prepared yolk-shell ternary composites, consisting of a Ni sphere as the core and dual SnO_2 (Ni_3Sn_2) compositions as the shell. The core sizes, interstitial void volumes and constituents of the yolk-shell structures can be tuned by control of the reaction times. The formation mechanism of the yolk-shell structures were also proposed based on time-dependent experiments. The yolk-shell structures were attributed to the cooperation between the etching reaction, galvanic replacement reaction and Kirkendall effect. The yolk-shell ternary SnO_2 (Ni_3Sn_2)@Ni composites synthesized at 15 h showed excellent electromagnetic absorption properties. The RL was shown to be as low as -43 dB at 6.1 GHz. The enhanced electromagnetic wave absorption properties were due to the good impedance match, multiple reflection and scattering thanks to the voids between core and shell, and effective complementarities between the dielectric loss and the magnetic loss.

3.2.3.2. Ni/non-oxide semiconductor composite as EM absorber

3.2.3.2.1. Ni/ZnS composite. Core-shell composites with Ni cores (1.0 μm) and ZnS nanowall shells were prepared through a hydrothermal deposition method by our team.[136] In comparison with Ni and ZnS particles, the Ni/ZnS composites showed the best electromagnetic wave absorption properties. The optimal RL was −25.78 dB at 14.24 GHz with the thickness of 2.7 mm. The RL below -10 dB (90% microwave absorption) was 4.72 GHz (11.52-16.24 GHz) with only thickness of 2.7 mm. The enhanced electromagnetic wave absorption capabilities of core-shell Ni/ZnS composites were due to good electromagnetic impedance match, interfacial relaxation and unique wall-like ZnS shells.

Subsequently, we also investigated the effect of Ni-core size on the electromagnetic wave absorption properties of Ni@ZnS composite.[268] The ultra-thin and crumpled ZnS nets-wrapped Ni walnut submicrosphere spheres (500 nm) core-shell composites were synthesized by a facile two-step process (Fig. 24(a-c)). The morphologies and microwave absorption properties of Ni/ZnS were

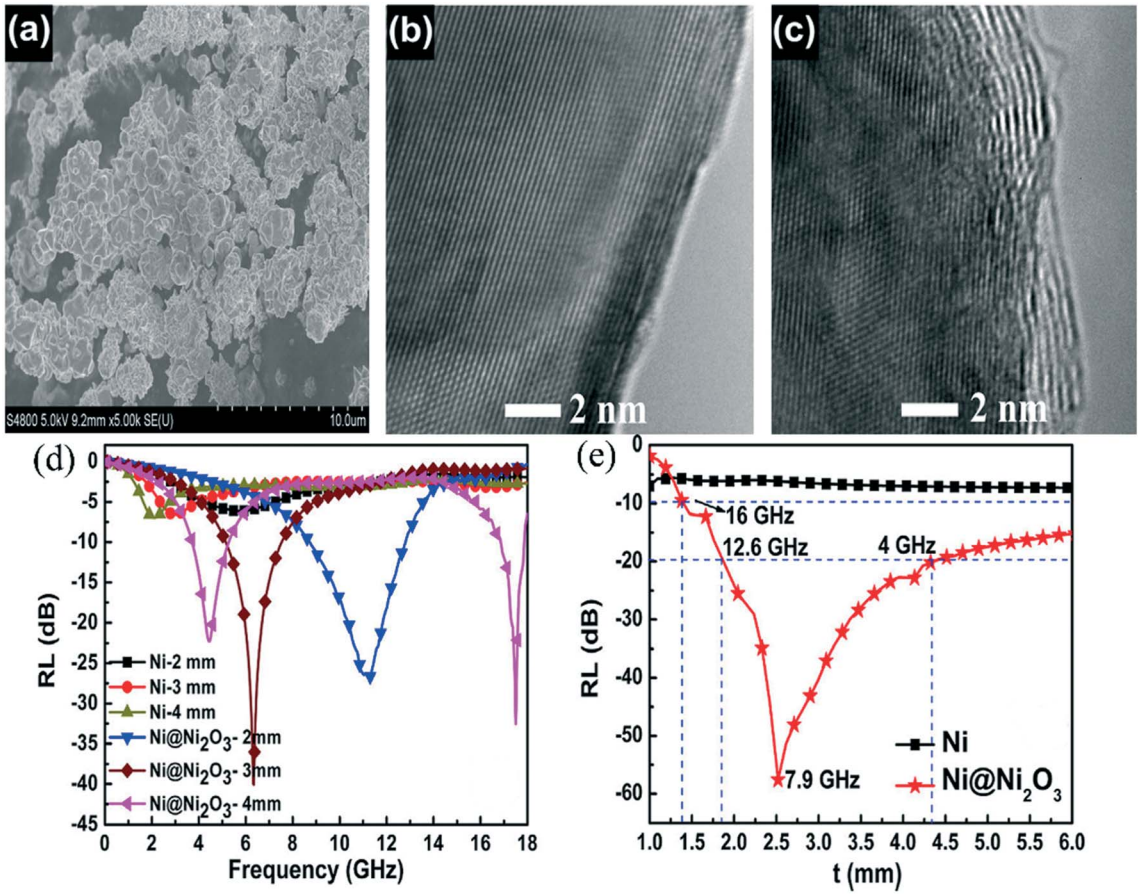

Fig. 21 SEM image of (a) Ni micro-particle; HRTEM images of(b) Ni micro-particle and (c) $Ni@Ni_2O_3$ core–shell particle. (d) Frequency dependence of RL for the Ni/paraffin and $Ni@Ni_2O_3$/paraffin composite at various thicknesses; (e) dependence of RL on the thickness of the Ni/paraffin and $Ni@Ni_2O_3$/paraffin composite. (Reprinted with permission from Ref. [247]. Copyright 2013, Elsevier B.V.)

determined by the hydrothermal temperature. Compared to pristine walnut-like Ni particles, the core-shell Ni/ZnS composites exhibited better electromagnetic absorption capabilities. The minimum RL of Ni@ZnS prepared at 60 °C was -42.4 dB at 12.3 GHz. Moreover, the effective bandwidth (RL< -10 dB, 90% microwave dissipation) could be observed in the 11.3-15.6 GHz rang with only absorber thickness of 2.2 mm (Fig. 24d). The outstanding electromagnetic absorption properties were attributed to good impedance match, nanosize effect, high attenuation constant, Debye relaxation and interfacial polarization of core-shell structure.

3.2.3.2.2. Other Ni/non-oxide semiconductor composite. We also prepared novel urchin-like ZnS/Ni_3S_2 coated Ni microspheres with core-shell structure (Fig. 25(a-c)).[93] We proposed a plausible formation mechanism of core-shell urchin-like architectures based on temperature dependent experiments (in-situ Ni reaction). The electromagnetic absorption measurements showed that the urchin-like ZnS/Ni_3S_2@Ni composite possessed the outstanding electromagnetic absorption properties compared with other ZnS/Ni_3S_2@Ni composites. The optimal RL of -27.6 dB can be observed at 5.2 GHz and the effective absorption (below -10 dB, 90% electromagnetic absorption) bandwidth can be tuned between 4.6 GHz and 18.0 GHz for the absorber with the thin thickness in 0.8-2.5 mm (Fig. 25d). The enhanced electromagnetic absorption properties were attributed to synergistic effect between dielectric loss and magnetic loss, multiple interfacial polarization resulting from the heterogeneous structures of core-shell ternary ZnS/Ni_3S_2@Ni composite, good impedance match and unique urchin-like structure. Lv et al.[269] used a sulfurization method to improve the poor impedance matching properties of Ni. Then, a novel material, NiS/Ni_3S_4 composite, was synthesized with excellent electromagnetic absorption because of excellent dielectric loss, good impedance matching properties and strong interfacial polarization. The RL (RL) values that less than -10 dB were observed in the frequency range 13.8-18.0 GHz (a broad microwave absorption bandwidth of 4.2 GHz) with only thickness of 1.8 mm. Besides, the minimum RL value was as low as -43.0 dB at 9.1 GHz with the thickness of 2.4 mm.

In our research, we prepared a hollow three-dimensional CuS hierarchical microspheres used Ni microspheres as template (Fig. 26).[270] Based on the time-dependent experiments, we proposed a plausible formation mechanism consisting of Galvanic replacement reaction and Ostwald ripening. The paraffin based composites containing 50 wt% hollow CuS flowers exhibited outstanding electromagnetic absorption capabilities. The minimal RL was -17.5 dB and the effective bandwidth was 3.0 GHz with thin absorber thickness of 1.1 mm. The high efficiency electromagnetic absorption properties originated from electric dielectric polarization and unique hollow flower-like structure. Moreover, the hollow structures can also tune dielectric properties

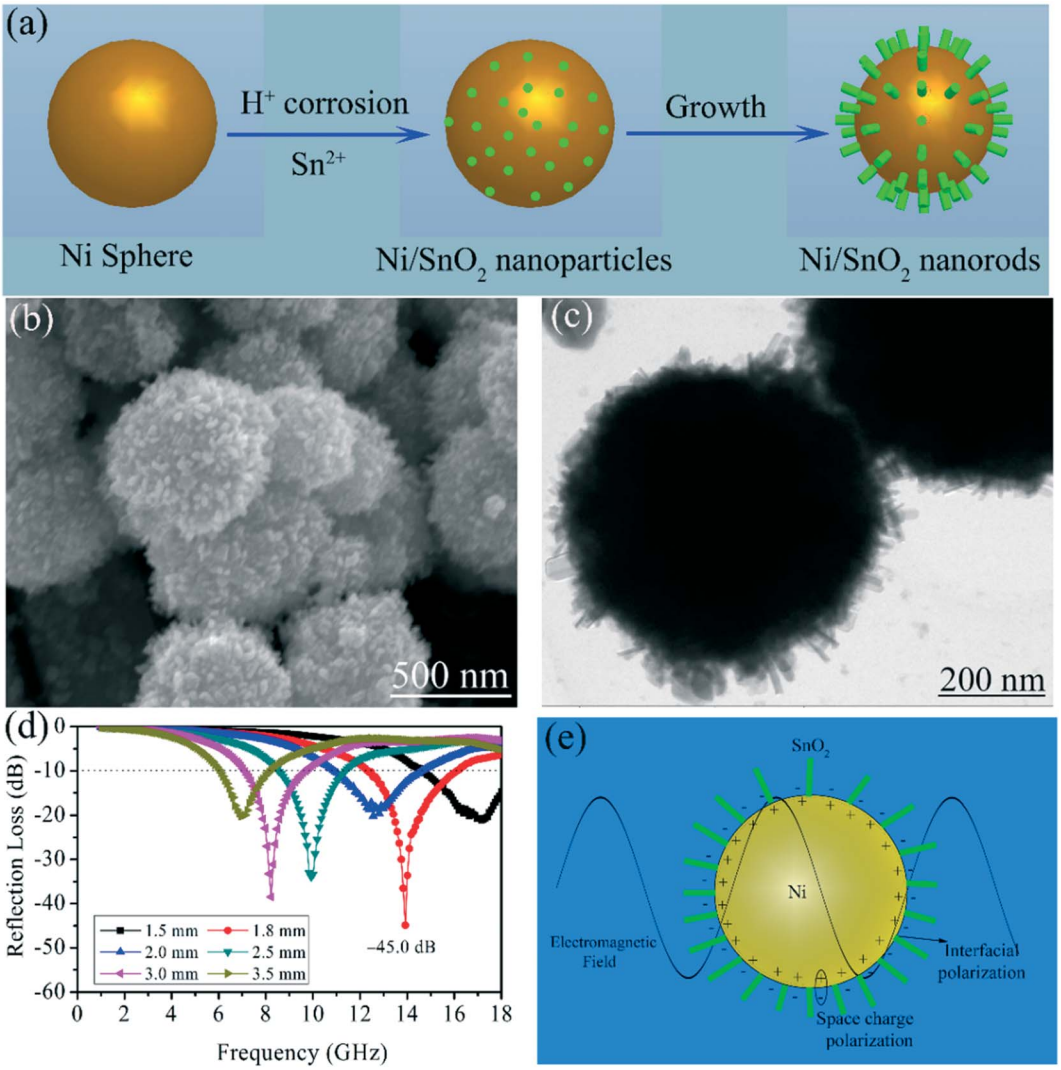

Fig. 22 (a) A formation mechanism of core-shell Ni/SnO_2 composites with SnO_2 nanorods grown on Ni spheres; (b) SEM and (c) TEM images of core-shell SnO_2 nanorods grown on Ni composite; (d) The frequency dependence of simulated RL values of core-shell Ni@SnO_2 composite; (e) Schematic illustration of the interaction of electromagnetic waves with a core-shell dielectric-magnetic Ni sphere@SnO_2 nanorods composite. (Reprinted with permission from Ref. [94]. Copyright 2015, American Chemical Society.)

to obtain good impedance matching. Additionally, the two-dimensional flakes and hollow flowers would cause more multiple reflection and scattering, which consumed more electromagnetic energy.

3.2.4. Ni-carbon composite as EM absorber. Carbon (C) is the fourth most abundant chemical element in the universe by mass after hydrogen, helium, and oxygen. It is the element that is nature's choice as a basis for life under conditions corresponding to those of Earth's surface.[271] Recently, carbonaceous electromagnetic wave absorbers have aroused intensive attention due to their low density and good electrical conductivity. Among them, porous carbon, carbon fibers, carbon nanotubes (CNTs), and graphene are playing a leading role as carbonaceous microwave absorbers because they have excellent physical and chemical properties such as high specific surface area, light weight, good electrical conductivity, mechanical strength, thermal stability, and corrosion resistance.[1,5,7,8,11,21,23,31,49,71,77,79,89,122,138,156,182,272–290] When the absorbers were designed with Ni as well as carbon materials, we may get suitable absorbing materials with the features of strong-absorption, wide-band and lightweight. This section intends to review recent progresses of Ni-carbon composites, such as Ni- porous carbon, Ni-carbon fiber, Ni-CNTs and Ni-graphene, for EM wave absorption applications.

3.2.4.1. Ni-porous carbon composite. Sunny et al.[291] reported the electromagnetic absorbing properties of nickel/carbon nanostructures synthesized by a controlled pyrolysis method. RLes were evaluated and found to be less than -10 dB over the entire X-band (8-12 GHz) for a thickness of 2.2-2.8 mm. A minimum RL of -45 dB was attained for an absorber thickness of 6.6 mm at 3.13 GHz. The space charge polarization from the nickel carbon interface and intrinsic magnetic loss of the hybrid magnetic metal carbon nanostructures were responsible for enhanced microwave absorbing properties. The Ni/C nanocapsules with ferromagnetic Ni nanoparticles as cores and graphite as shells, were prepared by a modified arc discharge technique.[292,293] The graphite shell played the double roles that makes the Ni nanoparticles free from oxidation and the separator for suppressing the eddy current loss, which

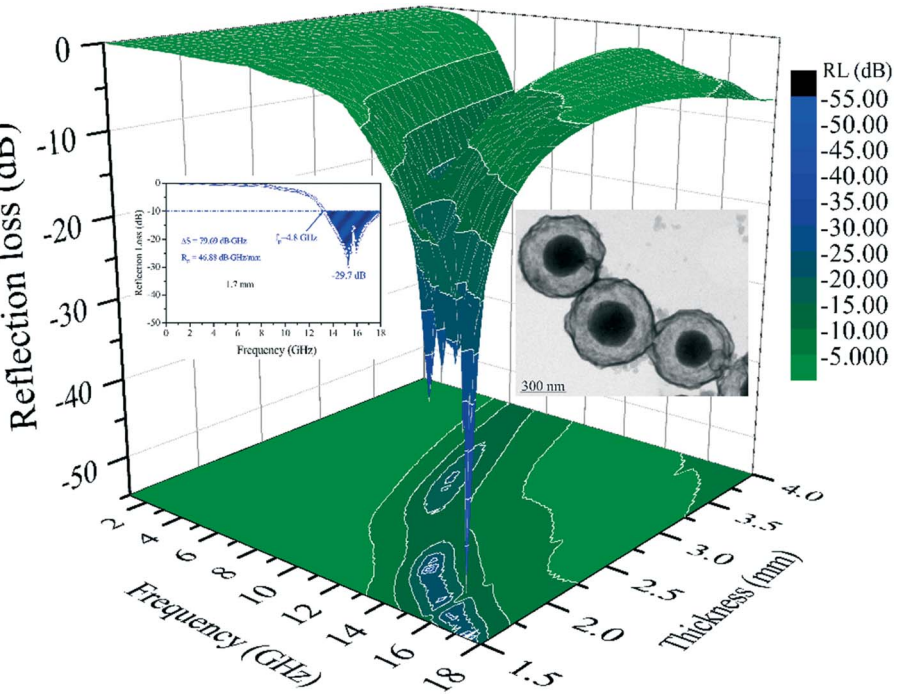

Fig. 23 Three-dimensional representation of RL values for the yolk-shell Ni@void@SnO_2 paraffin-based composite. Insets are the TEM image of Ni@void@SnO_2 and RL of yolk-shell Ni@void@SnO_2 composite with the thickness of 1.7 mm. (Reprinted with permission from Ref. [94]. Copyright 2016, American Chemical Society.)

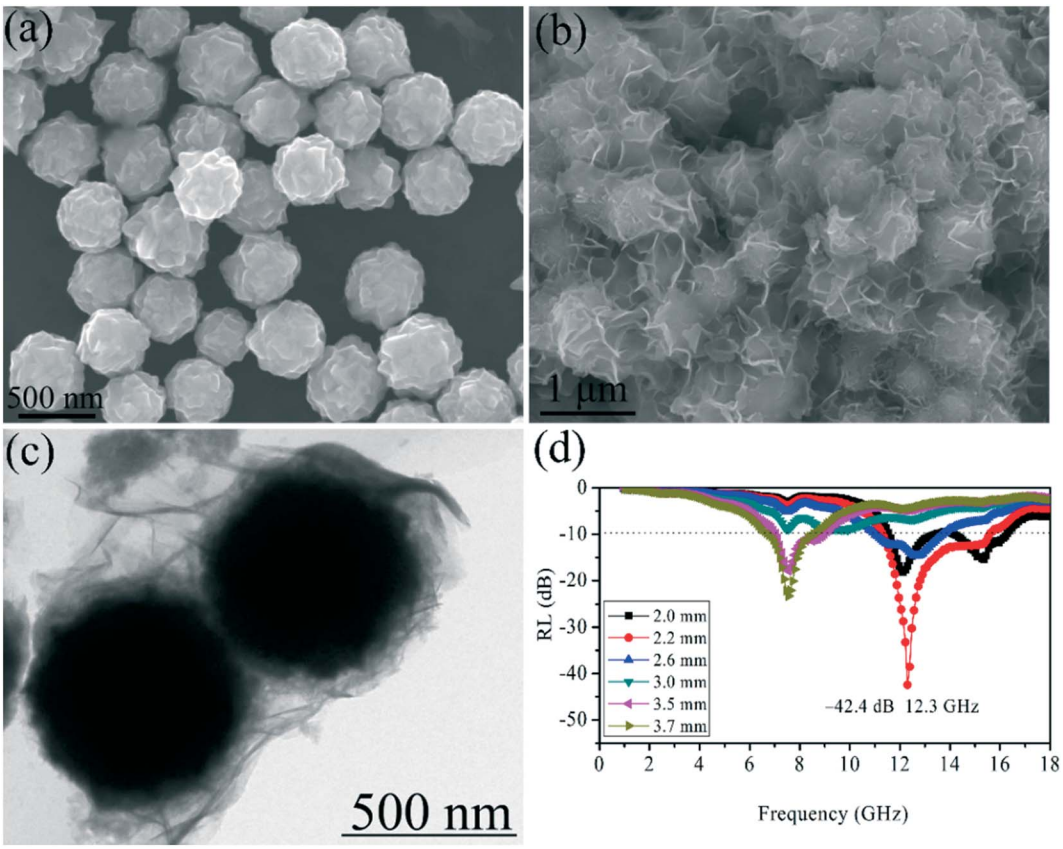

Fig. 24 (a) SEM image of Ni submicrometer walnuts; (b) SEM image and (c) TEM images of Ni@ZnS composite; (d) The RL of Ni@ZnS composite with various thicknesses. (Reprinted with permission from Ref. [268]. Copyright 2015, Royal Society of Chemistry.)

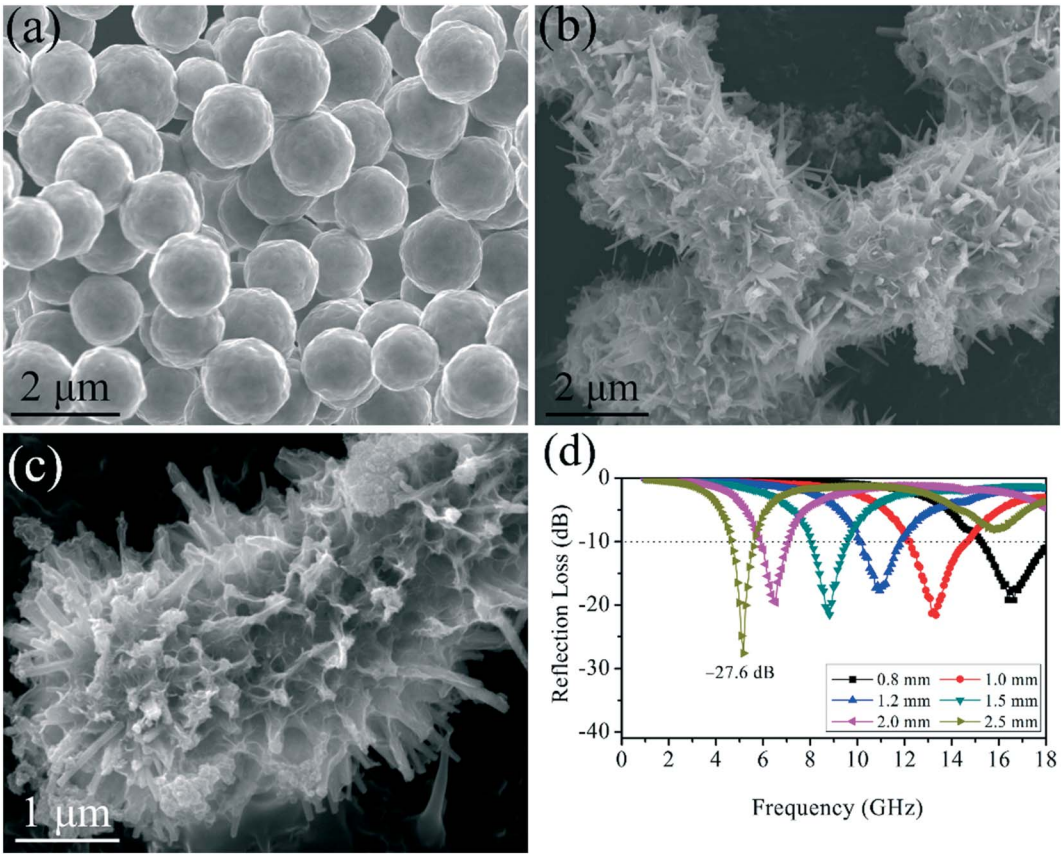

Fig. 25 (a) SEM image of Ni microspheres; (b,c) SEM images of Ni@ZnS/Ni_3S_2 composite; (d) The RL of Ni@ZnS/Ni_3S_2 composite with various thicknesses. (Reprinted with permission from Ref. [93]. Copyright 2015, Royal Society of Chemistry.)

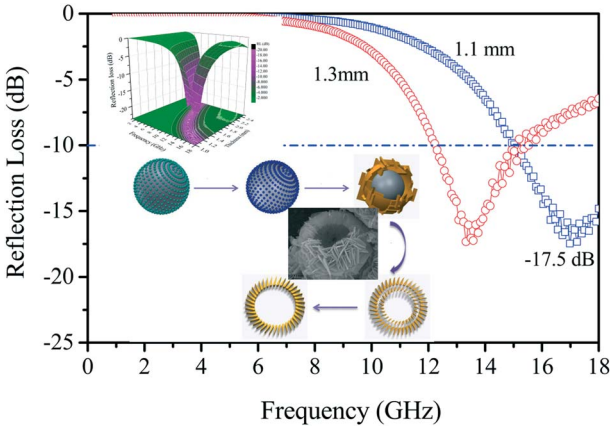

Fig. 26 Electromagnetic absorption properties of 50 wt% hollow CuS paraffin composites with a sample thickness of 1.1 and 1.3 mm. Insets are the SEM image of hollow CuS, three-dimensional representation of RL values, the proposed formation process of flower-like hierarchical CuS hollow microspheres. (Reprinted with permission from Ref. [270]. Copyright 2017, Royal Society of Chemistry.)

was beneficial for the enhancement of EM absorption properties of nanocapsules. Li et al.[294] prepared porous activated carbon ball composites impregnated with Ni composites through the wet chemistry method with a subsequent carbothermal reduction. With favorable magnetic loss and dielectric loss, the as-synthesized composites exhibited outstanding electromagnetic wave absorbing performances. Furthermore, the electromagnetic wave absorption including matching frequency, RL value, and effective bandwidth could be adjusted by changing the concentration of precursor solution and the thickness of the coating.

Zhao et al.[295] used an innovative, easy, and green method to synthesize an electromagnetic functionalized Ni/carbon foam (Fig. 27(a-c)). These Ni nanoparticles with a diameter of about 50-100 nm were highly crystallized and uniformly embedded in porous graphite carbon without aggregation. Also, the resultant foam had a high surface area (451 m^2 g^{-1}) and porosity and showed a moderate conductivity (6 S/m) and significant magnetism. Thanks to these special characteristics, the Ni/carbon foam showed greatly enhanced electromagnetic absorption ability. The Ni/carbon foam based composite could reach an effective absorption bandwidth (below -10 dB) of 4.5 GHz and the minimum RL value of -45 dB at 13.3 GHz with a thickness of 2 mm (Fig. 27d). Furthermore, the absorption mechanism of the foam was investigated in detail. The results showed that the derived strong dielectric loss, including conduction loss, interface polarization loss, weak magnetic loss, and nanoporosity, simultaneously made the contribution to electromagnetic absorption (Fig. 27e).

Ji and his group[296] prepared one-dimensional Ni@C composites with core-shell porous structure by a facile self-template strategy. Due to the interconnected mesoporous texture in nanorods, strengthened interfacial polarization from core-shell structure, and better impedance matching derived from a great deal of pores, the porous Ni@C nanorod

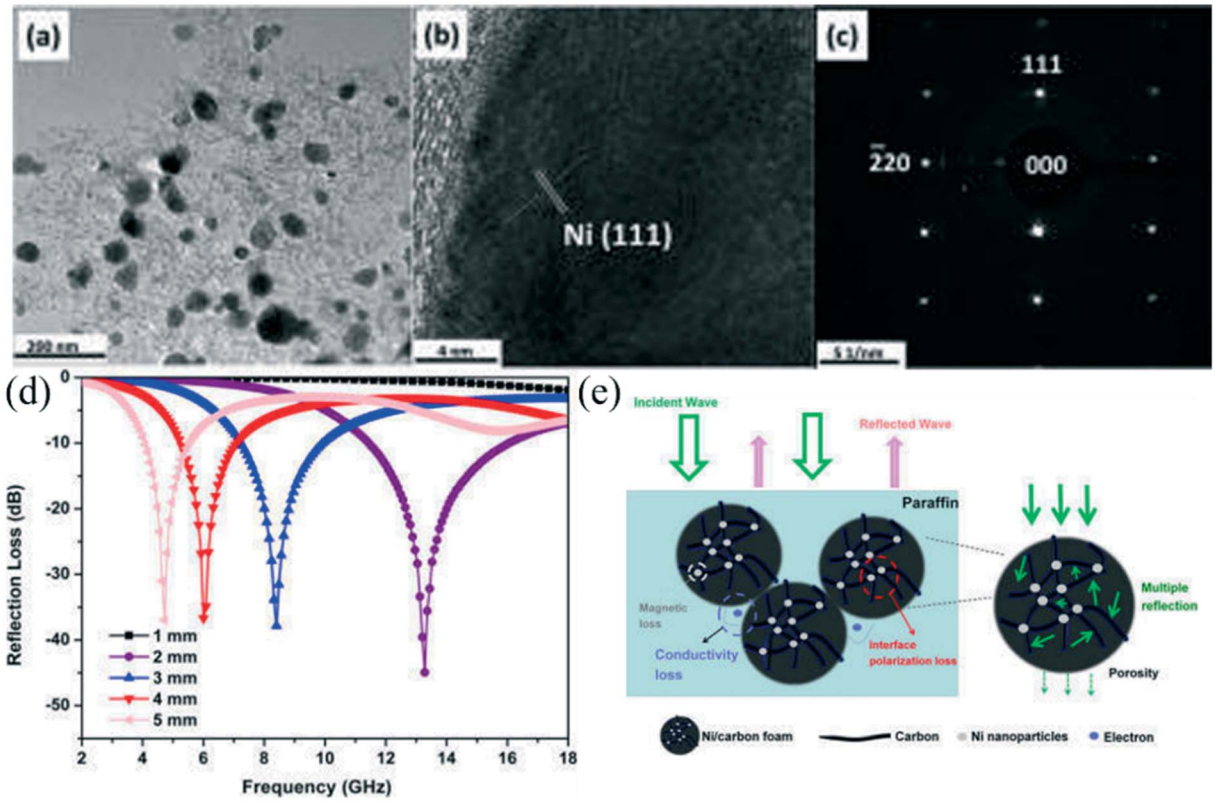

Fig. 27 (a) TEM image, (b) HR-TEM image, and (c) SEAD image of the Ni/carbon foam; (d) RL curves of the Ni/carbon foam sample in paraffin matrix with an absorber thickness from 1 mm to 5 mm; (e) Schematic description of possible microwave absorption mechanisms of the Ni/carbon foam sample in the paraffin matrix. (Reprinted with permission from Ref. [295]. Copyright 2016, American Chemical Society.)

composites exhibited perfect microwave absorption performance. The minimum RL value of -26.3 dB can be obtained at 10.8 GHz with a thickness of 2.3mm. Moreover, the effective bandwidth (RL≤-10 dB) can be achieved 5.2 GHz (12.2-17.4 GHz) with an absorber thickness of 1.8 mm. Moreover, in his team, they investigated electromagnetic properties of another porous carbon-wrapped Ni composite, which was derived from metal–organic-frameworks (Fig. 28(a-f)).[297] In the work, electromagnetic parameters were controlled through changing the carbonization temperature to fulfill optimized impedance matching. RL value of -51.8 dB and an effective frequency bandwidth of 3.48 GHz with a thickness of 2.6 mm could be obtained by Ni/C prepared at 500 °C, and RL value of -15.0 dB and an effective bandwidth of 4.72 GHz with a thin thickness of 1.8 mm could be received by Ni/C synthesized at 600 °C (Fig. 28(g-i)). They attributed strong absorption to the multiple dissipation mechanisms including conduction loss caused mainly by carbon, magnetic loss in Ni nanoparticles and multiple reflections induced by porous structure.

Zhao et al.[298] fabricated the magnetic and conductive Ni/carbon aerogels through an autocatalytic reduction process. In the composite aerogels, the crystallized Ni nanoparticles can be uniformly coated on the pore surface of the carbon aerogel matrix without aggregation. The influences of Ni nanoparticles amounts on the microstructures, porous characteristic, electrical conductivities, and magnetic properties were investigated in detail. The results showed that the Ni/carbon aerogels were highly porous with high specific surface area, suitable electrical conductivities and controllable magnetism. Thanks to these features, the Ni/carbon aerogels showed enhanced EM wave absorption properties. A minimal RL of -57 dB was observed at 13.3 GHz with the thickness of 2 mm. The dielectric loss (including conduction loss and interfacial polarization loss), relatively weak magnetic loss, as well as good impedance match contributed to the enhanced electromagnetic wave absorption.

3.2.4.2. Ni-carbon fiber composite. Xiang et al.[126] used the electrospinning combined with heat treatment in an Ar atmosphere to prepare the magnetic carbon nanofibers CNF–Ni in which the in situ formed magnetic Ni metal nanoparticles were evenly dispersed along nanofibers and encapsulated by ordered graphite layers (Fig. 29(a-c)). The generated core/shell microstructure could improve the impedance matching, EM-wave absorption properties and oxidation and corrosion resistances of the metal nanoparticles in CNF-Ni composites. The RL values below -20 dB were obtained in the frequency range of 3.8-18 GHz with the absorber thickness between 1.1 and 5.0 mm for the silicone composites containing 5 wt% CNF–Ni as filler (Fig. 29d). Moreover, the minimal RL reach -61.0 dB at 13.1 GHz with the matching thickness of 1.7 mm thanks to the efficient complementarities of complex permeability and permittivity resulting from the magnetic metal nanoparticles and lightweight carbon, as well as the particular particle/graphite core/shell microstructures. The results showed that the as-synthesized CNF–Ni hybrid nanofibers had a wide absorption frequency range, strong absorption ability, low density, and good physical and chemical stability, which are very attractive for potential applications in EM-wave absorbing materials.

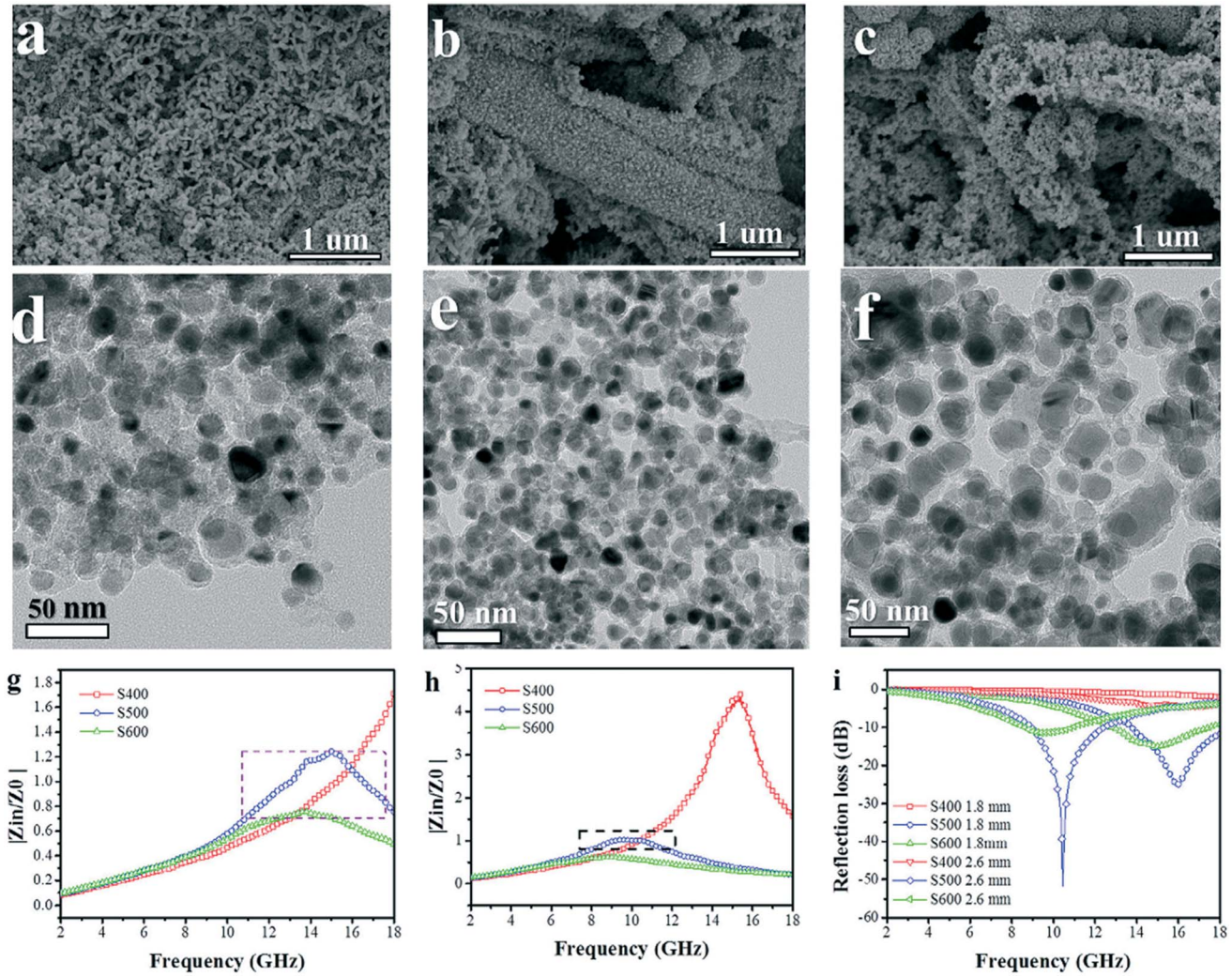

Fig. 28 SEM images of (a) porous Ni/C (400 °C, S400), (b) porous Ni/C (500 °C, S500) and (c) porous Ni/C (500 °C, S600); TEM images of (d) S400, (e) S500 and (f) S600; $|Z_{in}/Z_0|$ values of Ni/C composites with thickness of (g) 1.8 mm and (h) 2.6 mm and (i) corresponding RL values of each sample. (Reprinted with permission from Ref. [297]. Copyright 2017, Elsevier B.V.)

Bian et al.[299] employed an in situ assembly and electrochemical deposition technology with introducing reduced graphene oxide (RGO) into carbon fiber (CF) textiles to fabricate RGO-CF-Ni composites, in which nickel nanoparticles were in situ grown on the carbon matrices. Due to the presence of three-dimensional CF textiles and bi-functional nickel nanoparticles substantially influenced the related EM properties in the resulting hierarchical RGO-CF-Ni composite. The hierarchical composite textiles owned a strong shielding effectiveness greater than 61 dB, showing greater advantages than conventional polymeric and foamy shielding composites. The flexible CF-RGO-Ni composites of all electromagnetic active components offered the unique understanding of the multi-scale and multiple mechanisms in electromagnetic energy consumption.

3.2.4.3. Ni-carbon nanotubes composite. Wen et al.[119] prepared multi-walled carbon nanotubes (MWCNTs)/Ni nanopowders through a simple chemical method. The excellent electromagnetic absorption properties in S-band have been obtained due to proper combination of the complex permeability and permittivity resulting from the magnetic nanoparticles and lightweight MWCNTs. The frequency of microwave absorption obeys the quarter-wavelength matching model. A minimum RL value of -37 dB was observed at 2.14 GHz on a specimen with a matching thickness 5.19 mm. Moreover, it was also found that the RL below −20 dB from 1.83 to 3.07 GHz for the absorber thickness between 3.77 and 6.56 mm for MWCNTs/Ni. The MWCNTs/Ni composite could be a promising candidate for lightweight microwave absorption materials in S-band.

Tong et al.[300] reported rambutan-like heterostructures consisting of Ni microspheres coated with oriented multiwall carbon nanotubes (MWCNTs) were synthesized by the one-pot thermal decomposition of a mixture of polyethylene glycol (PEG) 20 000 as carbon source and NiO as Ni source (Fig. 30(a-c)). The growth of MWCNTs capped by Ni nanoparticles on the surface of the Ni nanoparticle-built microspheres followed a tip-growth mode (Fig. 30(d-f)). Increasing the mass ratio δ of polyethylene glycol (PEG) 20 000 to NiO rendered not only the increased C mass fraction but also the morphological conversion from Ni/C film core–shell structures to rambutan-like Ni/MWCNT heterostructures. Because of intensive eddy current loss and multi-resonance behaviors, rambutan-like Ni/MWCNT heterostructures

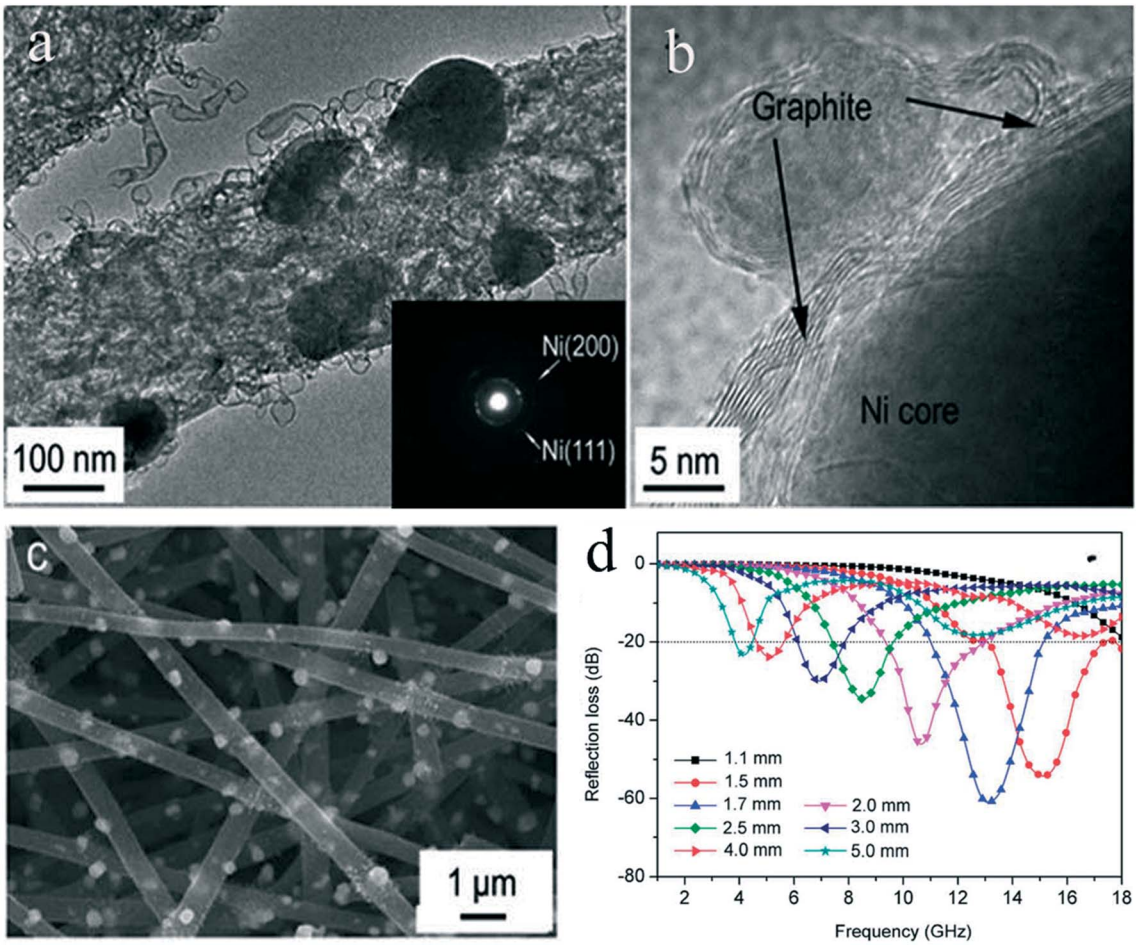

Fig. 29 (a) TEM image, (b) HRTEM image and (c) SEM image of the synthesized composite nanofibres CNF-Ni; (d) RL curve of CNF–Ni with different thicknesses in the frequency range of 1-18 GHz. Insets in (a) is the SAED patterns of a single Ni nanoparticle. (Reprinted with permission from Ref. [126]. Copyright 2014, Royal Society of Chemistry.)

with long MWCNTs exhibited significantly improved complex permeability and magnetic loss. The Ni/MWCNT heterostructures coated by short MWCNTs showed an optimal microwave absorption property with a minimum RL value of −37.9 dB occurring at 12.8 GHz. In particular, the absorption range less than −20 dB was over 5.0 to 9.2 GHz.

Sha et al.[301] used a microwave welding method to construct the chemical Ni−C bonding at the interface between carbon nanotubes (CNTs) and metal Ni to provide a different surface electron distribution. Originating from the Ni−C bonding between CNTs and metal Ni, the surface electric field distribution of the bonded metal nickel was adjusted and favored its high-frequency EM absorption based on a surface plasmon resonance mechanism. The Ni−CNT composite possessed outstanding microwave absorption properties in general radar frequency (2-18 GHz) as the thickness is only 2 mm, where the absorption bandwidth with a RL less than −10 dB was up to 6.5 GHz and the minimal RL was down to −30 dB. The absorption mechanism was mainly due to CNTs and metal Ni in the composite, as well as the Ni−C bonded interface.

3.2.4.4. Ni-graphene composite. Up to now, graphene, composed of a single layer of sp^2-bonded carbon atoms, has become a focus in the searching of the lightweight and efficient EM wave absorbers. Moreover, graphene is considered to be a promising alternative to EMI shielding materials, as it shows outstanding electrical conductivity, large surface area, low density and high corrosion resistance.[302–306] Lv et al.[307] and Cao et al.[308] have reviewed the recent progress about EM absorption properties of graphene based materials. One can refer to EM properties of graphene based absorbers from these two reviews. Herein, we just review recent advances of EM absorption properties of Ni/graphene composites.

Lv et al.[309] fabricated Ni/reduced graphene oxide (RGO) nanocomposites via an in-situ reduction step. During the reduction process, graphene oxide (GO) and Ni^{2+} ions were reduced synchronously, as a result, the magnetic Ni nanoparticles were dispersed in nonmagnetic RGO homogeneously. Benefiting from the cooperative effect between RGO and Ni, the as-fabricated Ni/RGO composites exhibited enhanced EM absorption performance in comparison with the individual compositions due to the enhancement of the electromagnetic wave loss properties and the enhanced electromagnetic impedance matching. Lai et al.[310] applied a facile one-step solvothermal reduction approach to prepare Ni microspheres decorated reduced graphene oxide (RGO). The electromagnetic parameters revealed that the samples exhibited tunable electromagnetic absorption properties through adjusting the initial concentrations of nickel salt. With the matching thickness of 1.2 mm, the

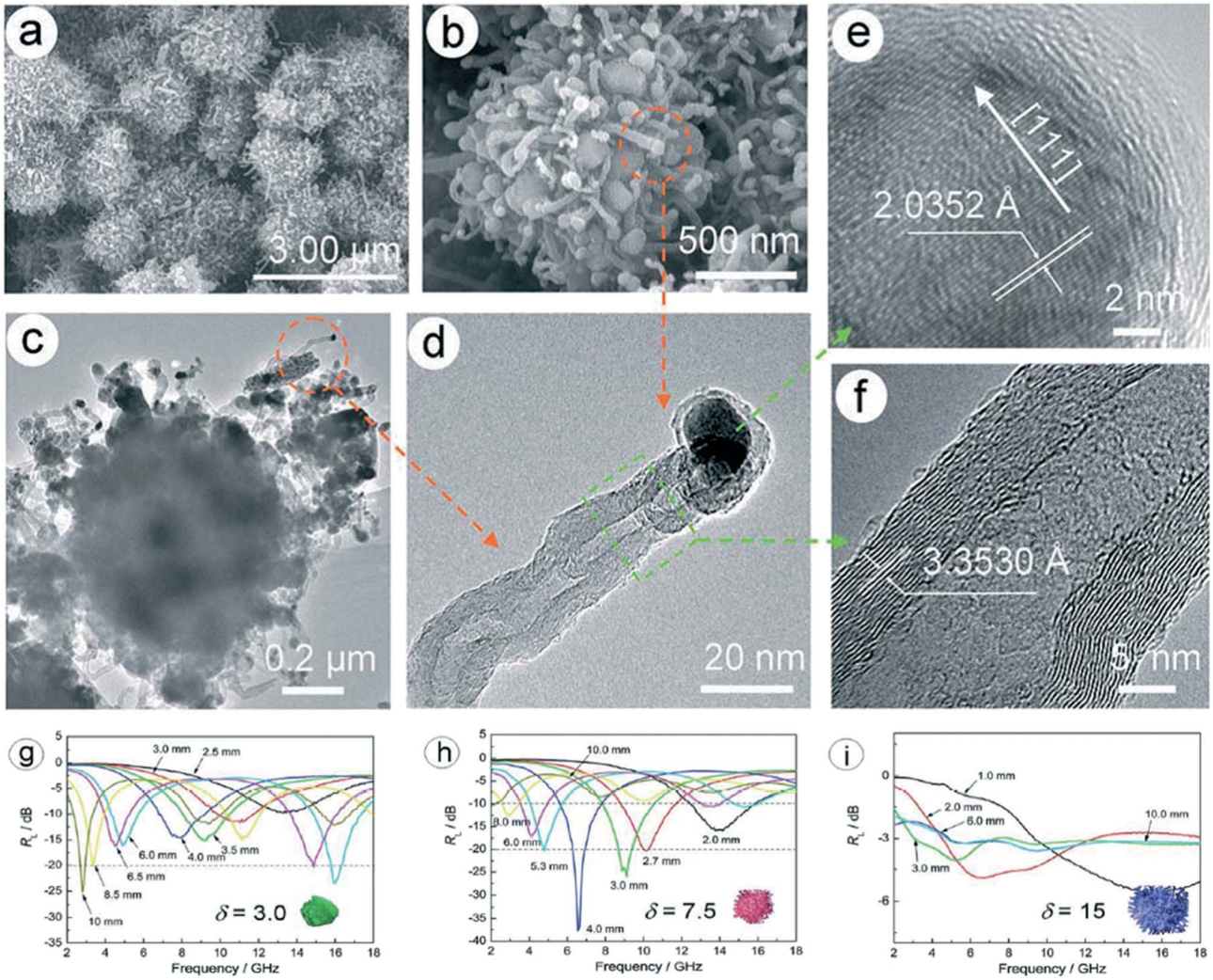

Fig. 30 (a, b) SEM and (c) TEM images of a typical rambutan-like particle. (d) TEM image of a typical MWCNT with catalyst particle encapsulated at the tip. The HRTEM images of (e) the catalyst particle and (f) the MWCNT. (g–i) RL curves (RL) of wax composites containing 30% mass fractions of the samples obtained at different mass ratios of PEG 20 000 to NiO (δ). (Reprinted with permission from Ref. [300]. Copyright 2014, Royal Society of Chemistry.)

RL (RL) of RGO-Ni achieved −31.4 dB at 14.5 GHz, and the effective absorption band (RL < −10 dB) ranged from 13.3 to 16.0 GHz. The excellent electromagnetic wave absorption capability could be reasonably described by the impedance matching characteristics and the quarter-wavelength attenuation model.

Fang et al.[311] stated that nanostructures of nickel were deposited on graphene nanosheet by direct electrochemical deposition. The RL values were calculated at given thickness layer according to transmit line theory in the range 2-18 GHz based on the relative complex permeability and permittivity. With the increasing of the thickness of the samples, the matching frequency inclined to shift to the lower frequency region, and theoretical RL become less at the matching frequency. After decorating graphene sheet with magnetic nickel nanoparticles, the composites were shown to efficiently promote electromagnetic absorbability. The absorption value of the composites below −10 dB reached 5 GHz absorbing bandwidth with a thickness of 1.5 mm and the maximum absorption value was −16.0 dB at 9.15 GHz. Cao et al.[312] fabricated the Ni/graphene nanocomposites via a substrate-free, atmospheric-pressure chemical vapor deposition process. The as-grown thin graphene sheets were produced in large scale with the thickness of ~2 nm, and they were decorated with numerous Ni/graphene core-shell nanoparticles. The electromagnetic absorption abilities of such Ni/graphene composites were investigated, and the maximum absorption was around −13 dB, and the absorbing characteristics could be modulated by varying the thickness of the nanocomposite absorbers for application in different frequency bands.

Wang et al.[138] used an atomic layer deposition (ALD) method to synthesize Ni/graphene composites (Fig. 31(a-c)). The surfaces of graphene were densely covered by Ni nanoparticles with a narrow size distribution, and the magnetic nanoparticles were well distributed on each graphene sheet without significant conglomeration or large vacancies. The coated graphene materials exhibited remarkably improved electromagnetic absorption properties compared to the pristine graphene. The minimum RL of 200-Ni/G was −21.1 dB at 15.1 GHz and the bandwidth corresponding to RL below −10 dB was higher than 3.8 GHz at a thickness of 2.0 mm (Fig. 31d). The enhanced absorption ability originated from the effective impedance

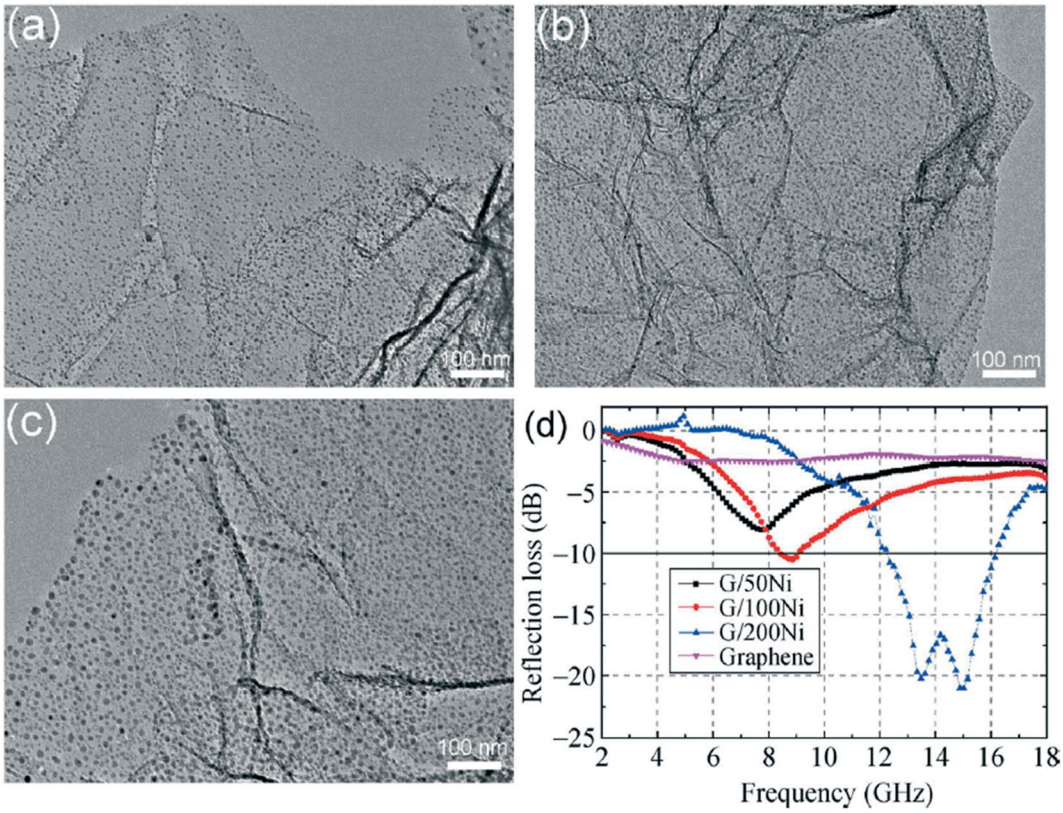

Fig. 31 TEM images of Ni/graphene obtained by applying (a) 50, (b) 100, and (c) 200 cycles of NiO deposition and then a hydrogen reduction process. (d) Electromagnetic RL curves of the product/paraffin composites with a thickness of 2.0 mm. (Reprinted with permission from Ref. [138]. Copyright 2017, Springer.)

matching, multiple interfacial polarization and increased magnetic loss from the added magnetic constituents.

Zhu et al.[313] reported a facile microwave assisted heating approach to produce reduced graphene oxide-nickel (RGO-Ni) composites. The results showed that Ni nanoparticles with a diameter round 20 nm were grown densely and evenly on the RGO sheets. In addition, enhanced electromagnetic absorption properties in Ku-band of RGO-Ni composites was mainly resulted from the synergistic effect of dielectric loss and magnetic loss and the dramatically electron polarizations induced by the formation of large conductive network. The optimal RL of RGO-Ni composite with the thickness of 2 mm could reach -42 dB at 17.6 GHz. Liu et al.[314] reported urchin-like Ni nanoparticles/reduced graphene oxide (u-Ni/RGO) composites were synthesized through a facile one-pot solvothermal method to reduce graphene oxide (GO) and nickel salt with hydrazine hydrate in ethylene glycol (EG). The resulting electromagnetic (EM) absorption properties showed that the optimal RL of u-Ni/RGO composites was up to -32.1 dB at 13.8 GHz and the absorption bandwidth with the RLless than −10 dB was 4.5 GHz (from 10.9 to 15.4 GHz) with the thickness of 2 mm. Interestingly, the RL curve exhibited two obvious peaks. The remarkable EM absorption properties of u-Ni/RGO composites could be attributed to the multiple absorbing mechanisms including multi-interfacial polarization, better impedance matching between the dielectric loss and magnetic loss, polarization relaxation, residual defects and groups in RGO.

Yuan et al.[315] developed a facile strategy for preparation of nickel particle encapsulated in few-layer nitrogen doped graphene supported by graphite carbon sheets (Ni@NG/NC) as a high performance electromagnetic wave absorbing material (Fig. 32(a-d)). The fabricated hetero-nanostructures exhibited excellent EM absorption property including strong absorption capability and lightweight feature. The effective bandwidth could reach 8.5 GHz at the thicknesses of 3.0 mm for the heteronanostructures with the optimized Ni content as the addition amount the hetero-nanostructures is only 20 wt% (Fig. 32(e,f)). Furthermore, due to the nitrogen-doped graphene shell, the Ni NPs showed robust stability against strong acidic solution and strong anti-oxidation upon air exposure. The reason for the positive of the N doping may be related to the different electronegativity between C and N atoms, resulting in partial positive and negative charges in the adjacent C and N species, respectively. Such adjacent C and N species can regard as polarization centers, which can enhance the dielectric loss of nitrogen-doped carbonaceous materials upon electromagnetic wave irradiation.

Chen et al.[316] reported hexagonal close-packed Ni (h-Ni) nanocrystals and face-centered cubic Ni (c-Ni) nanoflowers with uniform size and high dispersion were assembled on graphene nanosheets (GN) via a facile one-step solution-phase strategy under different reaction conditions. The results showed that the as-formed h-Ni nanocrystals with a diameter as small as 3 nm were grown densely and uniformly on the graphene sheets, and thus the aggregation of the h-Ni nanocrystals was effectively prevented. Moreover, c-Ni nanospheres assembled by c-Ni nanocrystals with a size of 15 nm were also uniformly deposited on the graphene sheets. These Ni/GN nanocomposites exhibited remarkable electromagnetic absorption performance at low or middle frequencies (2.0-10.0 GHz). The outstanding electromagnetic

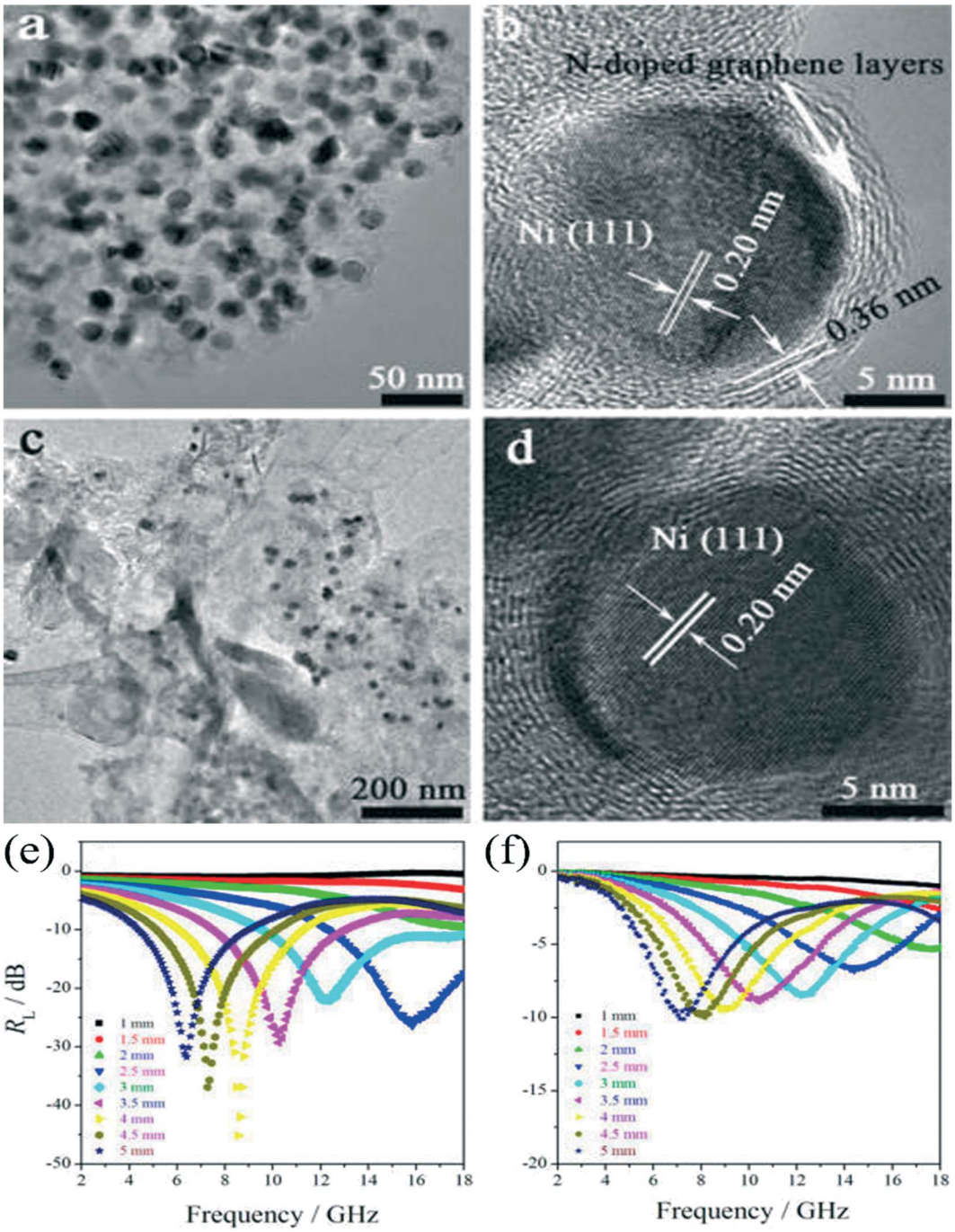

Fig. 32 (a and b) TEM and HRTEM images of Ni@NG/NC-3:1; (c and d) TEM and HRTEM images of Ni@NG/NC-9:1. Frequency dependence RL curves for (e) Ni@NG/NC-3:1 and (f) Ni@NG/NC-9:1. (Reprinted with permission from Ref. [315]. Copyright 2016, American Chemical Society.)

absorption performance of the Ni/GN nanocomposites may be ascribed to the excellent electronic properties of GN nanosheets and excellent magnetic properties of Ni nanostructures.

4. Conclusions and outlook

This review has introduced various synthesis methods, electromagnetic attenuation theories, and electromagnetic absorption properties of Ni-based absorbers. As a typical ferromagnetic absorbers, metal Ni, due to the high saturation magnetization and high permeability at high frequency, have attracted more attention. However, because of the relatively high electrical conductivity, the permeability of Ni materials decrease very rapidly at high frequency thanks to the eddy current losses caused by the alternated electromagnetic fields, which is generally named as skin-depth effect. There are two accepted method to deal with this issue. One way is to decrease the size of Ni particles or fabricate complex hierarchical shape to decrease electrical conductivity, thus, the eddy current effect is prohibited. The other way is to compound

with other materials to generate unique structure to tune impedance match and electromagnetic energy dissipation ability, which would cause more absorption and less reflection.

Ni particle has a skin depth of about 1 μm over 1-5 GHz. That is to say, if Ni particles possess sizes larger than 1 μm, then only the surface part with a thickness of about 1 μm contributed to electromagnetic properties, while the remain interior portion makes no contribution. Thus, we decrease the Ni size to less than 1 μm to obtain enhance electromagnetic absorption performance. Furthermore, the Ni particles were deliberately designed with hierarchical complex structure, such as one-dimensional structure (nanowires, nano-chains), two-dimensional structure (nano-flakes) and three dimensional structure (flowers, nano-cones, nano-urchins), besides the decrease of eddy current effect, the special microstructures would also be beneficial for the enhancement of electromagnetic absorption capabilities.

Nowadays, the well accepted avenue is to blend other materials to produce Ni based composites, such as Ni-metal composites, Ni-polymer composite, Ni-semiconductor composite, and Ni-carbon composite. In these composites, synergistic effect between dielectric loss and magnetic loss, as well as better impedance match are favorable for the improvement of electromagnetic properties. Furthermore, when the unique microstructures, such as, core-shell structure, yolk-shell and hollow porous structure, are introduced into Ni based composites, benefiting from lightweight characteristic, interfacial polarization, multiple reflection and scattering mechanism, they would exhibit enhanced electromagnetic properties. Additionally, one can also tune electromagnetic properties of Ni based composites by control of the constituent morphology.

To obtain the suitable absorbers with features of lightweight, small thickness, strong absorption and wide bandwidth, the ferromagnetic Ni materials should be compounded with other high dielectric or magnetic loss materials as well as accompanying porous structure. Especially, combing with carbonaceous (CNTs or graphene), the Ni-carbon ternary or quaternary even more phases composite, would be the promising absorption materials. When the core-shell structure, yolk-shell or hollow porous structure were simultaneously added into these Ni-carbon composites, benefiting from multiple absorption mechanisms, the enhanced electromagnetic wave absorption could be obtained, and this direction would be the best choice in the future.

Conflict of interest

There are no conflicts to declare.

Acknowledgements

The authors gratefully acknowledge the financial support from the National Natural Science Foundation of China (Grant No. 51602287, 51764022 and 51672254), and Key Science and Technology Program of Henan Province (182102210108).

References:

1 X. Li, J. Feng, Y. Du, J. Bai, H. Fan, H. Zhang, Y. Peng and F. Li, *J. Mater. Chem. A*, 2015, **3**, 5535–5546.
2 B. Zhao, J. Deng, L. Liang, C. Zuo, Z. Bai, X. Guo and R. Zhang, *CrystEngComm*, 2017, **19**, 6095–6106.
3 B. Zhao, L. Liang, J. Deng, Z. Bai, J. Liu, X. Guo, K. Gao, W. Guo and R. Zhang, *CrystEngComm*, 2017, **19**, 6579–6587.
4 B. Zhao, C. Ma, L. Liang, W. Guo, B. Fan, X. Guo and R. Zhang, *CrystEngComm*, 2017, **19**, 3640–3648.
5 F. Wang, Y. Sun, D. Li, B. Zhong, Z. Wu, S. Zuo, D. Yan, R. Zhuo, J. Feng and P. Yan, *Carbon*, 2018, **134**, 264–273.
6 X. Jian, B. Wu, Y. Wei, S. X. Dou, X. Wang, W. He and N. Mahmood, *ACS Appl. Mater. Interfaces*, 2016, **8**, 6101–6109.
7 G. Wang, Z. Gao, S. Tang, C. Chen, F. Duan, S. Zhao, S. Lin, Y. Feng, L. Zhou and Y. Qin, *ACS Nano*, 2012, **6**, 11009–11017.
8 Z. Zeng, H. Jin, M. Chen, W. Li, L. Zhou and Z. Zhang, *Adv. Funct. Mater.*, 2016, **26**, 303–310.
9 C. Wang, Y. Ding, Y. Yuan, X. He, S. Wu, S. Hu, M. Zou, W. Zhao, L. Yang and A. Cao, *J. Mater. Chem. C*, 2015, **3**, 11893–11901.
10 F. Shahzad, M. Alhabeb, C. B. Hatter, B. Anasori, S. Man Hong, C. M. Koo and Y. Gogotsi, *Science*, 2016, **353**, 1137.
11 Q. Song, F. Ye, X. Yin, W. Li, H. Li, Y. Liu, K. Li, K. Xie, X. Li, Q. Fu, L. Cheng, L. Zhang and B. Wei, *Adv. Mater.*, 2017, **29**, 1701583.
12 D. Ding, Y. Wang, X. Li, R. Qiang, P. Xu, W. Chu, X. Han and Y. Du, *Carbon*, 2017, **111**, 722.
13 G. Sun, B. Dong, M. Cao, B. Wei and C. Hu, *Chem. Mater.*, 2011, **23**, 1587–1593.
14 J. Fang, T. Liu, Z. Chen, Y. Wang, W. Wei, X. Yue and Z. Jiang, *Nanoscale*, 2016, **8**, 8899–8909.
15 J. Liu, R. Che, H. Chen, F. Zhang, F. Xia, Q. Wu and M. Wang, *Small*, 2012, **8**, 1214–1221.
16 J.-M. Thomassin, C. Jérôme, T. Pardoen, C. Bailly, I. Huynen and C. Detrembleur, *Mater. Sci. Eng., R*, 2013, **74**, 211–232.
17 B. Zhao, C. Zhao, R. Li, S. M. Hamidinejad and C. B. Park, *ACS Appl. Mater. Interfaces*, 2017, **9**, 20873–20884.
18 B. Zhao, S. Wang, C. Zhao, R. Li, S. M. Hamidinejad, Y. Kazemi and C. B. Park, *Carbon*, 2018, **127**, 469–478.
19 B. Zhao and C. B. Park, *J. Mater. Chem. C*, 2017, **5**, 6954–6961.
20 H. Lv, X. Liang, Y. Cheng, H. Zhang, D. Tang, B. Zhang, G. Ji and Y. Du, *ACS Appl. Mater. Interfaces*, 2015, **7**, 4744–4750.
21 G. Wu, Y. Cheng, Z. Yang, Z. Jia, H. Wu, L. Yang, H. Li, P. Guo and H. Lv, *Chem. Eur. J.*, 2018, **333**, 519–528.
22 H. Lv, H. Zhang, B. Zhang, G. Ji, Y. He and Q. Lin, *J. Mater. Chem. C*, 2016, **4**, 5476–5482.
23 X. Qiu, L. Wang, H. Zhu, Y. Guan and Q. Zhang, *Nanoscale*, 2017, **9**, 7408–7418.
24 M. Qiao, X. Lei, Y. Ma, L. Tian, X. He, K. Su and Q. Zhang, *Nano Res.*, 2017, **11**, 1500–1519.
25 D. Sun, Q. Zou, Y. Wang, Y. Wang, W. Jiang and F. Li, *Nanoscale*, 2014, **6**, 6557–6562.
26 C. Song, X. Yin, M. Han, X. Li, Z. Hou, L. Zhang and L. Cheng, *Carbon*, 2017, **116**, 50–58.
27 L. Yan, J. Liu, S. Zhao, B. Zhang, Z. Gao, H. Ge, Y. Chen, M. Cao and Y. Qin, *Nano Res.*, 2017, **10**, 1595–1607.
28 H. Lv, H. Zhang, J. Zhao, G. Ji and Y. Du, *Nano Res.*, 2016, **9**, 1813–1822.
29 X. F. Zhang, H. Huang and X. L. Dong, *J. Phys. Chem. C*, 2013, **117**, 8563–8569.
30 Q. Liu, Q. Cao, H. Bi, C. Liang, K. Yuan, W. She, Y. Yang and R. Che, *Adv. Mater.*, 2016, **28**, 486–490.
31 H. Lv, G. Ji, H. Zhang, M. Li, Z. Zuo, Y. Zhao, B. Zhang, D. Tang and Y. Du, *Sci. Rep.*, 2015, **5**, 18249.
32 A. Wang, W. Wang, C. Long, W. Li, J. Guan, H. Gu and G. Xu, *J. Mater. Chem. C*, 2014, **2**, 3769–3776.
33 L.-S. Fu, J.-T. Jiang, C.-Y. Xu and L. Zhen, *CrystEngComm*, 2012, **14**, 6827–6832.
34 S. L. Wen, Y. Liu, X. C. Zhao, J. W. Cheng and H. Li, *Phys. Chem. Chem. Phys.*, 2014, **16**, 18333–18340.
35 X. Zhan, H. Tang, Y. Du, A. Talbi, J. Zha and J. He, *RSC Adv.*, 2013, **3**, 15966–15970.
36 J.-r. Liu, M. Itoh, M. Terada, T. Horikawa and K.-i. Machida, *Appl. Phys. Lett.*, 2007, **91**, 093101.
37 X. Li, D. Du, C. Wang, H. Wang and Z. Xu, *J. Mater. Chem. C*, 2018, **6**, 558–567.

38 G.-X. Tong, W.-H. Wu, Q. Hu, J.-H. Yuan, R. Qiao and H.-S. Qian, *Mater. Chem. Phys.*, 2012, **132**, 563–569.
39 Y. Lü, Y. Wang, H. Li, Y. Lin, Z. Jiang, Z. Xie, Q. Kuang and L. Zheng, *ACS Appl. Mater. Interfaces*, 2015, **7**, 13604–13611.
40 X.-L. Shi, M.-S. Cao, J. Yuan and X.-Y. Fang, *Appl. Phys. Lett.*, 2009, **95**, 163108.
41 Z. Wang, H. Bi, P. Wang, M. Wang, Z. Liu, L. shen and X. Liu, *Phys. Chem. Chem. Phys.*, 2015, **17**, 3796–3801.
42 C. Wang, X. Han, X. Zhang, S. Hu, T. Zhang, J. Wang, Y. Du, X. Wang and P. Xu, *J. Phys. Chem. C*, 2010, **114**, 14826–14830.
43 C. He, S. Qiu, X. Wang, J. Liu, L. Luan, W. Liu, M. Itoh and K.-i. Machida, *J. Mater. Chem.*, 2012, **22**, 22160–22166.
44 P. Yang, M. Yu, J. Fu and L. Wang, *J. Alloys Compd.*, 2017, **721**, 449–455.
45 Y. Wang, F.-q. Gu, L.-j. Ni, K. Liang, K. Marcus, S.-l. Liu, F. Yang, J.-j. Chen and Z.-s. Feng, *Nanoscale*, 2017, **9**, 18318–18325.
46 H. Liu, Y. Li, K. Dai, G. Zheng, C. Liu, C. Shen, X. Yan, J. Guo and Z. Guo, *J. Mater. Chem. C*, 2016, **4**, 157–166.
47 Y. Wang, L.-j. Ni, F. Yang, F.-q. Gu, K. Liang, K. Marcus, Y.-d. Wan, J.-j. Chen and Z.-s. Feng, *J. Mater. Chem. C*, 2017, **5**, 12769–12776.
48 J. Jung, H. Lee, I. Ha, H. Cho, K. K. Kim, J. Kwon, P. Won, S. Hong and S. H. Ko, *ACS Appl. Mater. Interfaces*, 2017, **9**, 44609–44616.
49 Y. Yuan, W. Yin, M. Yang, F. Xu, X. Zhao, J. Li, Q. Peng, X. He, S. Du and Y. Li, *Carbon*, 2018, **130**, 59–68.
50 I. Arief, S. Biswas and S. Bose, *ACS Appl. Mater. Interfaces*, 2017, **9**, 19202–19214.
51 S. Biswas, G. P. Kar and S. Bose, *Nanoscale*, 2015, **7**, 11334–11351.
52 S.-T. Hsiao, C.-C. M. Ma, W.-H. Liao, Y.-S. Wang, S.-M. Li, Y.-C. Huang, R.-B. Yang and W.-F. Liang, *ACS Appl. Mater. Interfaces*, 2014, **6**, 10667–10678.
53 S.-T. Hsiao, C.-C. M. Ma, H.-W. Tien, W.-H. Liao, Y.-S. Wang, S.-M. Li, C.-Y. Yang, S.-C. Lin and R.-B. Yang, *ACS Appl. Mater. Interfaces*, 2015, **7**, 2817–2826.
54 D. D. L. Chung, *Carbon*, 2001, **39**, 279–285.
55 A. Chaudhary, S. Kumari, R. Kumar, S. Teotia, B. P. Singh, A. P. Singh, S. K. Dhawan and S. R. Dhakate, *ACS Appl. Mater. Interfaces*, 2016, **8**, 10600–10608.
56 Z. Zeng, C. Wang, Y. Zhang, P. Wang, S. I. Seyed Shahabadi, Y. Pei, M. Chen and X. Lu, *ACS Appl. Mater. Interfaces*, 2018, **10**, 8205–8213.
57 H. Li, X. Lu, D. Yuan, J. Sun, F. Erden, F. Wang and C. He, *J. Mater. Chem. C*, 2017, **5**, 8694–8698.
58 S. Biswas, S. S. Panja and S. Bose, *J. Mater. Chem. C*, 2018, **6**, 3120–3142.
59 H.-J. Yang, W.-Q. Cao, D.-Q. Zhang, T.-J. Su, H.-L. Shi, W.-Z. Wang, J. Yuan and M.-S. Cao, *ACS Appl. Mater. Interfaces*, 2015, **7**, 7073–7077.
60 J.-M. Thomassin, X. Lou, C. Pagnoulle, A. Saib, L. Bednarz, I. Huynen, R. Jérôme and C. Detrembleur, *J. Phys. Chem. C*, 2007, **111**, 11186–11192.
61 P. Saini, V. Choudhary, N. Vijayan and R. K. Kotnala, *J. Phys. Chem. C*, 2012, **116**, 13403–13412.
62 X. Yin, L. Kong, L. Zhang, L. Cheng, N. Travitzky and P. Greil, *Int. Mater. Rev.*, 2014, **59**, 326–355.
63 F. Meng, H. Wang, F. Huang, Y. Guo, Z. Wang, D. Hui and Z. Zhou, *Composites Part B*, 2018, **137**, 260–277.
64 A. Ameli, M. Nofar, S. Wang and C. B. Park, *ACS Appl. Mater. Interfaces*, 2014, **6**, 11091–11100.
65 L. Wang, H. Xing, S. Gao, X. Ji and Z. Shen, *J. Mater. Chem. C*, 2017, **5**, 2005–2014.
66 J. Liu, H.-B. Zhang, R. Sun, Y. Liu, Z. Liu, A. Zhou and Z.-Z. Yu, *Adv. Mater.*, 2017, **29**, 1702367.
67 T. H. Ting, R. P. Yu and Y. N. Jau, *Mater. Chem. Phys.*, 2011, **126**, 364–368.
68 L. Zhang, P. Zhou, H. Lu, L. Zhang, J. Xie and L. Deng, *Opt. Mater. Express*, 2016, **6**, 1393–1404.
69 H. Lv, Z. Yang, L. Wang Paul, G. Ji, J. Song, L. Zheng, H. Zeng and J. Xu Zhichuan, *Adv. Mater.*, 2018, **30**, 1706343.
70 Y. Li, Y. Zhao, X. Lu, Y. Zhu and L. Jiang, *Nano Res.*, 2016, **9**, 2034–2045.
71 H. Sun, R. Che, X. You, Y. Jiang, Z. Yang, J. Deng, L. Qiu and H. Peng, *Adv. Mater.*, 2014, **26**, 8120–8125.
72 Q. Liu, X. Xu, W. Xia, R. Che, C. Chen, Q. Cao and J. He, *Nanoscale*, 2015, **7**, 1736–1743.
73 Q. Liu, Q. Cao, X. Zhao, H. Bi, C. Wang, D. S. Wu and R. Che, *ACS Appl. Mater. Interfaces*, 2015, **7**, 4233–4240.
74 O. Khani, M. Z. Shoushtari, M. Jazirehpour and M. H. Shams, *Ceram. Int.*, 2016, **42**, 14548–14556.
75 M. Han, X. Yin, H. Wu, Z. Hou, C. Song, X. Li, L. Zhang and L. Cheng, *ACS Appl. Mater. Interfaces*, 2016, **8**, 21011–21019.
76 M. Han, X. Yin, L. Kong, M. Li, W. Duan, L. Zhang and L. Cheng, *J. Mater. Chem. A*, 2014, **2**, 16403–16409.
77 L. Kong, X. Yin, X. Yuan, Y. Zhang, X. Liu, L. Cheng and L. Zhang, *Carbon*, 2014, **73**, 185–193.
78 M. Han, X. Yin, W. Duan, S. Ren, L. Zhang and L. Cheng, *J. Eur. Ceram. Soc.*, 2016, **36**, 2695–2703.
79 H. Lv, G. Ji, X. Liang, H. Zhang and Y. Du, *J. Mater. Chem. C*, 2015, **3**, 5056–5064.
80 M. Qiao, X. Lei, Y. Ma, L. Tian, K. Su and Q. Zhang, *Chem. Eur. J.*, 2016, **304**, 552–562.
81 Y. Wan, J. Xiao, C. Li, G. Xiong, R. Guo, L. Li, M. Han and H. Luo, *J. Magn. Magn. Mater.*, 2016, **399**, 252–259.
82 X. Zhang, G. Ji, W. Liu, X. Zhang, Q. Gao, Y. Li and Y. Du, *J. Mater. Chem. C*, 2016, **4**, 1860–1870.
83 X. Zhang, Y. Rao, J. Guo and G. Qin, *Carbon*, 2016, **96**, 972–979.
84 H. Lv, Y. Guo, Z. Yang, Y. Cheng, L. P. Wang, B. Zhang, Y. Zhao, Z. J. Xu and G. Ji, *J. Mater. Chem. C*, 2017, **5**, 491–512.
85 B. Zhao, G. Shao, B. Fan, W. Zhao and R. Zhang, *RSC Adv.*, 2015, **5**, 42587–42590.
86 B. Zhao, G. Shao, B. Fan, W. Zhao and R. Zhang, *Phys. Chem. Chem. Phys.*, 2015, **17**, 6044–6052.
87 B. Zhao, W. Zhao, G. Shao, B. Fan and R. Zhang, *Dalton Trans.*, 2015, **44**, 15984–15993.
88 B. Zhao, G. Shao, B. Fan, C. Wang, Y. Xie and R. Zhang, *Powder Technol.*, 2015, **270**, 20–26.
89 Z. Han, D. Li, H. Wang, X. G. Liu, J. Li, D. Y. Geng and Z. D. Zhang, *Appl. Phys. Lett.*, 2009, **95**, 023114.
90 B. Zhao, B. Fan, G. Shao, W. Zhao and R. Zhang, *ACS Appl. Mater. Interfaces*, 2015, **7**, 18815–18823.
91 L. Wang, X. Jia, Y. Li, F. Yang, L. Zhang, L. Liu, X. Ren and H. Yang, *J. Mater. Chem. A*, 2014, **2**, 14940–14946.
92 Y. Du, W. Liu, R. Qiang, Y. Wang, X. Han, J. Ma and P. Xu, *ACS Appl. Mater. Interfaces*, 2014, **6**, 12997–13006.
93 B. Zhao, G. Shao, B. Fan, W. Zhao, S. Zhang, K. Guan and R. Zhang, *J. Mater. Chem. C*, 2015, **3**, 10862–10869.
94 B. Zhao, X. Guo, W. Zhao, J. Deng, G. Shao, B. Fan, Z. Bai and R. Zhang, *ACS Appl. Mater. Interfaces*, 2016, **8**, 28917–28925.
95 B. Zhao, G. Shao, B. Fan, W. Zhao and R. Zhang, *Phys. Chem. Chem. Phys.*, 2015, **17**, 2531–2539.
96 X. Zhang, Y. Li, R. Liu, Y. Rao, H. Rong and G. Qin, *ACS Appl. Mater. Interfaces*, 2016, **8**, 3494–3498.
97 A. Nicolson and G. Ross, *IEEE Trans. Instrum. Meas.*, 1970, **19**, 377–382.
98 W. B. Weir, *Proc. IEEE*, 1974, **62**, 33–36.
99 S. Wen, Y. Liu, X. Zhao and J. Cheng, *J. Appl. Phys.*, 2014, **116**, 054310.
100 C. Brosseau and P. Talbot, *J. Appl. Phys.*, 2005, **97**, 104325.
101 C. Brosseau and P. Talbot, *Dielectr. Electr. Insul., IEEE Trans.*, 2004, **11**, 819–832.
102 K. Wang, G. Wan, G. Wang, Z. He, S. Shi, L. Wu and G. Wang, *J. Colloid Interface Sci.*, 2018, **511**, 307–317.
103 J. Feng, Y. Zong, Y. Sun, Y. Zhang, X. Yang, G. Long, Y. Wang, X. Li and X. Zheng, *Chem. Eng. J.*, 2018, **345**, 441–451.
104 C. Zhang, B. Wang, J. Xiang, C. Su, C. Mu, F. Wen and Z. Liu, *ACS Appl. Mater. Interfaces*, 2017, **9**, 28868–28875.
105 B. Quan, X. Liang, G. Ji, J. Ma, P. Ouyang, H. Gong, G. Xu and Y. Du, *ACS Appl. Mater. Interfaces*, 2017, **9**, 9964–9974.
106 X. Hong, Q. Wang, Z. Tang, W. Q. Khan, D. Zhou and T. Feng, *J. Phys. Chem. C*, 2016, **120**, 148–156.
107 C. Tian, Y. Du, C. Cui, Z. Deng, J. Xue, P. Xu, R. Qiang, Y. Wang and X. Han, *J. Mater. Sci.*, 2017, **52**, 6349–6361.
108 B. Zhao, X. Guo, W. Zhao, J. Deng, B. Fan, G. Shao, Z. Bai and R. Zhang, *Nano Res.*, 2017, **10**, 331–343.

109 Z. Ma, Y. Zhang, C. Cao, J. Yuan, Q. Liu and J. Wang, *Physica B*, 2011, **406**, 4620–4624.
110 X. Yuan, L. Cheng, L. Kong, X. Yin and L. Zhang, *J. Alloys Compd.*, 2014, **596**, 132–139.
111 H. Xing, Z. Liu, L. Lin, L. Wang, D. Tan, Y. Gan, X. Ji and G. Xu, *RSC Adv.*, 2016, **6**, 41656–41664.
112 X. Yuan, L. Cheng and L. Zhang, *J. Alloys Compd.*, 2016, **680**, 604–611.
113 X. Yuan, X. Xue, H. Ma, S. Guo and L. Cheng, *Nanotechnology*, 2017, **28**, 375705.
114 W. Chu, Y. Wang, Y. Du, R. Qiang, C. Tian and X. Han, *J. Mater. Sci.*, 2017, **52**, 13636–13649.
115 D. Liu, R. Qiang, Y. Du, Y. Wang, C. Tian and X. Han, *J. Colloid Interface Sci.*, 2018, **514**, 10–20.
116 X. Tian, F. Meng, F. Meng, X. Chen, Y. Guo, Y. Wang, W. Zhu and Z. Zhou, *ACS Appl. Mater. Interfaces*, 2017, **9**, 15711–15718.
117 F. Meng, W. Wei, X. Chen, X. Xu, M. Jiang, L. Jun, Y. Wang and Z. Zhou, *Phys. Chem. Chem. Phys.*, 2016, **18**, 2510–2516.
118 G. Wang, X. Peng, L. Yu, G. Wan, S. Lin and Y. Qin, *J. Mater. Chem. A*, 2015, **3**, 2734–2740.
119 F. Wen, F. Zhang and Z. Liu, *J. Phys. Chem. C*, 2011, **115**, 14025–14030.
120 S. Dai, Y. Cheng, B. Quan, X. Liang, W. Liu, Z. Yang, G. Ji and Y. Du, *Nanoscale*, 2018, **10**, 6945–6953.
121 T. Liu, X. Xie, Y. Pang and S. Kobayashi, *J. Mater. Chem. C*, 2016, **4**, 1727–1735.
122 P. Liu, Z. Yao, J. Zhou, Z. Yang and L. B. Kong, *J. Mater. Chem. C*, 2016, **4**, 9738–9749.
123 C. Jin, Z. He, Y. Zhao, Y. Pan, W. Wu, X. Wang and G. Tong, *CrystEngComm*, 2018, **20**, 1997–2009.
124 L. Yan, X. Wang, S. Zhao, Y. Li, Z. Gao, B. Zhang, M. Cao and Y. Qin, *ACS Appl. Mater. Interfaces*, 2017, **9**, 11116–11125.
125 W. Liu, L. Liu, Z. Yang, J. Xu, Y. Hou and G. Ji, *ACS Appl. Mater. Interfaces*, 2018, **10**, 8965–8975.
126 J. Xiang, J. Li, X. Zhang, Q. Ye, J. Xu and X. Shen, *J. Mater. Chem. A*, 2014, **2**, 16905–16914.
127 D. Li, H. Liao, H. Kikuchi and T. Liu, *ACS Appl. Mater. Interfaces*, 2017, **9**, 44704–44714.
128 C. Liu, Y. Zhang, Y. Tang, Z. Wang, N. Ma and P. Du, *J. Mater. Chem. C*, 2017, **5**, 3461–3472.
129 Y. Yong, Y. Yang, X. Wen and D. Jun, *J. Appl. Phys.*, 2014, **115**, 17A521.
130 P. Liu, V. M. H. Ng, Z. Yao, J. Zhou, Y. Lei, Z. Yang, H. Lv and L. B. Kong, *ACS Appl. Mater. Interfaces*, 2017, **9**, 16404–16416.
131 C. Tian, Y. Du, P. Xu, R. Qiang, Y. Wang, D. Ding, J. Xue, J. Ma, H. Zhao and X. Han, *ACS Appl. Mater. Interfaces*, 2015, **7**, 20090–20099.
132 D. Chen, H. Quan, G. S. Wang and L. Guo, *ChemPlusChem*, 2013, **78**, 843–851.
133 H. Yu, T. Wang, B. Wen, M. Lu, Z. Xu, C. Zhu, Y. Chen, X. Xue, C. Sun and M. Cao, *J. Mater. Chem.*, 2012, **22**, 21679–21685.
134 Y.-Z. Wei, G.-S. Wang, Y. Wu, Y.-H. Yue, J.-T. Wu, C. Lu and L. Guo, *J. Mater. Chem. A*, 2014, **2**, 5516–5524.
135 B. Zhao, G. Shao, B. Fan, B. Sun, K. Guan and R. Zhang, *J. Mater. Sci.: Mater. Electron.*, 2014, **25**, 3614–3621.
136 B. Zhao, G. Shao, B. Fan, W. Zhao, Y. Xie and R. Zhang, *RSC Adv.*, 2014, **4**, 61219–61225.
137 G. Li, L. Wang, W. Li and Y. Xu, *RSC Adv.*, 2015, **5**, 8248–8257.
138 G. Wang, Z. Gao, G. Wan, S. Lin, P. Yang and Y. Qin, *Nano Res.*, 2014, **7**, 704–716.
139 P. Xu, X. Han, C. Wang, D. Zhou, Z. Lv, A. Wen, X. Wang and B. Zhang, *J. Phys. Chem. B*, 2008, **112**, 10443–10448.
140 B. Zhao, B. Fan, Y. Xu, G. Shao, X. Wang, W. Zhao and R. Zhang, *ACS Appl. Mater. Interfaces*, 2015, **7**, 26217–26225.
141 X. Zhang, P. Guan and X. Dong, *Appl. Phys. Lett.*, 2010, **96**, 223111.
142 S. He, C. Lu, G.-S. Wang, J.-W. Wang, H.-Y. Guo and L. Guo, *ChemPlusChem*, 2014, **79**, 569–576.
143 X.-J. Zhang, G.-S. Wang, Y.-Z. Wei, L. Guo and M.-S. Cao, *J. Mater. Chem. A*, 2013, **1**, 12115–12122.
144 B. Zhao, G. Shao, B. Fan, W. Zhao, Y. Xie and R. Zhang, *J. Mater. Chem. A*, 2015, **3**, 10345–10352.
145 B. Wen, M.-S. Cao, Z.-L. Hou, W.-L. Song, L. Zhang, M.-M. Lu, H.-B. Jin, X.-Y. Fang, W.-Z. Wang and J. Yuan, *Carbon*, 2013, **65**, 124–139.
146 K. Zhang, F. Wu, A. Xie, M. Sun and W. Dong, *ACS Appl. Mater. Interfaces*, 2017, **9**, 33041–33048.
147 P. H. Fang, *J. Chem. Phys.*, 1965, **42**, 3411–3413.
148 A.-P. Guo, X.-J. Zhang, J.-K. Qu, S.-W. Wang, J.-Q. Zhu, G.-S. Wang and L. Guo, *Mater. Chem. Front.*, 2017, **1**, 2519–2526.
149 M. Zong, Y. Huang, Y. Zhao, X. Sun, C. Qu, D. Luo and J. Zheng, *RSC Adv.*, 2013, **3**, 23638–23648.
150 J.-Z. He, X.-X. Wang, Y.-L. Zhang and M.-S. Cao, *J. Mater. Chem. C*, 2016, **4**, 7130–7140.
151 K. Yuan, R. Che, Q. Cao, Z. Sun, Q. Yue and Y. Deng, *ACS Appl. Mater. Interfaces*, 2015, **7**, 5312–5319.
152 X. Jian, X. Xiao, L. Deng, W. Tian, X. Wang, N. Mahmood and S. Dou, *ACS Appl. Mater. Interfaces*, 2018, **10**, 9369–9378.
153 P. J. van der Zaag, *J. Magn. Magn. Mater.*, 1999, **196**, 315.
154 Z. Zhu, X. Sun, H. Xue, H. Guo, X. Fan, X. Pan and J. He, *J. Mater. Chem. C*, 2014, **2**, 6582–6591.
155 N. Li, G.-W. Huang, Y.-Q. Li, H.-M. Xiao, Q.-P. Feng, N. Hu and S.-Y. Fu, *ACS Appl. Mater. Interfaces*, 2017, **9**, 2973–2983.
156 Y. Zhang, X. Wang and M. Cao, *Nano Res.*, 2018, **11**, 1426–1436.
157 B. Zhao, G. Shao, B. Fan, W. Guo, Y. Chen and R. Zhang, *Appl. Surf. Sci.*, 2015, **332**, 112–120.
158 B. Zhao, G. Shao, B. Fan, W. Zhao and R. Zhang, *J. Mater. Sci.: Mater. Electron.*, 2015, **26**, 5393–5399.
159 T. Liu, P. Zhou, J. Xie and L. Deng, *J. Appl. Phys.*, 2012, **111**, 093905.
160 T. Liu, P. H. Zhou, J. L. Xie and L. J. Deng, *J. Appl. Phys.*, 2011, **110**, 033918.
161 P. Toneguzzo, O. Acher, G. Viau, F. Fiévet-Vincent and F. Fiévet, *J. Appl. Phys.*, 1997, **81**, 5546–5548.
162 P. Toneguzzo, G. Viau, O. Acher, F. Fiévet-Vincent and F. Fiévet, *Adv. Mater.*, 1998, **10**, 1032–1035.
163 B. Lu, X. L. Dong, H. Huang, X. F. Zhang, X. G. Zhu, J. P. Lei and J. P. Sun, *J. Magn. Magn. Mater.*, 2008, **320**, 1106–1111.
164 G. Datt, C. Kotabage and A. C. Abhyankar, *Phys. Chem. Chem. Phys*, 2017, **19**, 20699–20712.
165 I. Shanenkov, A. Sivkov, A. Ivashutenko, V. Zhuravlev, Q. Guo, L. Li, G. Li, G. Wei and W. Han, *Phys. Chem. Chem. Phys*, 2017, **19**, 19975–19983.
166 X.-J. Zhang, G.-S. Wang, W.-Q. Cao, Y.-Z. Wei, J.-F. Liang, L. Guo and M.-S. Cao, *ACS Appl. Mater. Interfaces*, 2014, **6**, 7471–7478.
167 D. Moitra, S. Dhole, B. K. Ghosh, M. Chandel, R. K. Jani, M. K. Patra, S. R. Vadera and N. N. Ghosh, *J. Phys. Chem. C*, 2017, **121**, 21290–21304.
168 J. Zhu, S. Wei, N. Haldolaarachchige, D. P. Young and Z. Guo, *J. Phys. Chem. C*, 2011, **115**, 15304–15310.
169 T. Wu, Y. Liu, X. Zeng, T. Cui, Y. Zhao, Y. Li and G. Tong, *ACS Appl. Mater. Interfaces*, 2016, **8**, 7370.
170 Y. Yang, C. Xu, Y. Xia, T. Wang and F. Li, *J. Alloys Compd.*, 2010, **493**, 549–552.
171 J. Ji, Y. Huang, J. Yin, X. Zhao, X. Cheng, J. He, J. Wang, X. Li and J. Liu, *J. Phys. Chem. C*, 2018, **122**, 3628–3637.
172 M. Wu, Y. D. Zhang, S. Hui, T. D. Xiao, S. Ge, W. A. Hines, J. I. Budnick and G. W. Taylor, *Appl. Phys. Lett.*, 2002, **80**, 4404–4406.
173 K. Wang, Y. Chen, R. Tian, H. Li, Y. Zhou, H. Duan and H. Liu, *ACS Appl. Mater. Interfaces*, 2018, **10**, 11333–11342.
174 Y. Wang, Y. Lai, S. Wang and W. Jiang, *Ceram. Int.*, 2017, **43**, 1887–1894.
175 G. Tong, Y. Liu, T. Cui, Y. Li, Y. Zhao and J. Guan, *Appl. Phys. Lett.*, 2016, **108**, 072905.
176 B. Bateer, L. Wang, L. Zhao, P. Yu, C. Tian, K. Pan and H. Fu, *RSC Adv.*, 2015, **5**, 60135–60140.
177 B. Zhao, B. Fan, Y. Xie and R. Zhang, *Optik*, 2015, **126**, 4597–4600.
178 B. Zhao, G. Shao, B. Fan, W. Li, X. Pian and R. Zhang, *Mater. Lett.*, 2014, **121**, 118–121.
179 S. He, G.-S. Wang, C. Lu, J. Liu, B. Wen, H. Liu, L. Guo and M.-S. Cao, *J. Mater. Chem. A*, 2013, **1**, 4685–4692.
180 J. Fang, Y. Shang, Z. Chen, W. Wei, Y. Hu, X. Yue and Z. Jiang, *J. Mater. Chem. C*, 2017, **5**, 4695–4705.
181 Y.-J. Chen, P. Gao, R.-X. Wang, C.-L. Zhu, L.-J. Wang, M.-S. Cao and H.-B. Jin, *J. Phys. Chem. C*, 2009, **113**, 10061–10064.

182 Y.-J. Chen, G. Xiao, T.-S. Wang, Q.-Y. Ouyang, L.-H. Qi, Y. Ma, P. Gao, C.-L. Zhu, M.-S. Cao and H.-B. Jin, *J. Phys. Chem. C*, 2011, **115**, 13603–13608.
183 J. Liu, J. Cheng, R. Che, J. Xu, M. Liu and Z. Liu, *J. Phys. Chem. C*, 2012, **117**, 489–495.
184 H.-L. Zhu, Y.-J. Bai, R. Liu, N. Lun, Y.-X. Qi, F.-D. Han and J.-Q. Bi, *J. Mater. Chem.*, 2011, **21**, 13581–13587.
185 D. Yan, S. Cheng, R. Zhuo, J. Chen, J. Feng, H. Feng, H. Li, Z. Wu, J. Wang and P. Yan, *Nanotechnology*, 2009, **20**, 105706.
186 G. Wang, L. Wang, Y. Gan and W. Lu, *Appl. Surf. Sci.*, 2013, **276**, 744–749.
187 L. Yun, C. Tingting, W. Tong, L. Yana and T. Guoxiu, *Nanotechnology*, 2016, **27**, 165707.
188 X. a. Fan, J. Guan, W. Wang and G. Tong, *J. Phys. D: Appl. Phys.*, 2009, **42**, 075006.
189 Y.-H. Chen, Z.-H. Huang, M.-M. Lu, W.-Q. Cao, J. Yuan, D.-Q. Zhang and M.-S. Cao, *J. Mater. Chem. A*, 2015, **3**, 12621–12625.
190 J. Bao, C. Tie, Z. Xu, Q. Zhou, D. Shen and Q. Ma, *Adv. Mater.*, 2001, **13**, 1631–1633.
191 W. Zhou, L. He, R. Cheng, L. Guo, C. Chen and J. Wang, *J. Phys. Chem. C*, 2009, **113**, 17355–17358.
192 H. Niu, Q. Chen, M. Ning, Y. Jia and X. Wang, *J. Phys. Chem. B*, 2004, **108**, 3996–3999.
193 J. Xiang, Y. Chu, X. Zhang and X. Shen, *Appl. Surf. Sci.*, 2012, **263**, 320–325.
194 J. Yang, J. Zhang, C. Liang, M. Wang, P. Zhao, M. Liu, J. Liu and R. Che, *ACS Appl. Mater. Interfaces*, 2013, **5**, 7146–7151.
195 B. Zhao, G. Shao, B. Fan, Y. Xie and R. Zhang, *J. Magn. Magn. Mater.*, 2014, **372**, 195–200.
196 B. Gao, L. Qiao, J. Wang, Q. Liu, F. Li, J. Feng and D. Xue, *J. Phys. D: Appl. Phys.*, 2008, **41**, 235005.
197 B. Zhao, B. Fan, G. Shao, B. Wang, X. Pian, W. Li and R. Zhang, *Appl. Surf. Sci.*, 2014, **307**, 293–300.
198 C. Gong, J. Zhang, X. Zhang, L. Yu, P. Zhang, Z. Wu and Z. Zhang, *J. Phys. Chem. C*, 2010, **114**, 10101–10107.
199 J. Liu, M.-S. Cao, Q. Luo, H.-L. Shi, W.-Z. Wang and J. Yuan, *ACS Appl. Mater. Interfaces*, 2016, **8**, 22615–22622.
200 W. W. Pan, Q. F. Liu, R. Han, X. Chi and J. B. Wang, *Appl. Phys. A*, 2013, **113**, 755–761.
201 F. Ma, Y. Qin and Y.-Z. Li, *Appl. Phys. Lett.*, 2010, **96**, 202507.
202 L. Deng, L. Ding, K. Zhou, S. Huang, Z. Hu and B. Yang, *J. Magn. Magn. Mater.*, 2011, **323**, 1895–1898.
203 M. Zhou, F. Lu, B. Chen, X. Zhu, X. Shen, W. Xia, H. He and X. Zeng, *Mater. Lett.*, 2015, **159**, 498–501.
204 C. Wang, X. Han, P. Xu, J. Wang, Y. Du, X. Wang, W. Qin and T. Zhang, *J. Phys. Chem. C*, 2010, **114**, 3196–3203.
205 Z. Wang, J. Zou, Z. Ding, J. Wu, P. Wang, S. Jin and H. Bi, *Mater. Chem. Phys.*, 2013, **142**, 119–123.
206 Z. An, S. Pan and J. Zhang, *J. Phys. Chem. C*, 2009, **113**, 2715–2721.
207 Y. Sun, N. Wu, C. Cui, S. W. Or and X. Liu, *Mater. Res.*, 2015, **18**, 1115–1120.
208 J. Kong, W. Liu, F. Wang, X. Wang, L. Luan, J. Liu, Y. Wang, Z. Zhang, M. Itoh and K.-i. Machida, *J. Solid State Chem.*, 2011, **184**, 2994–3001.
209 B. Zhao, G. Shao, B. Fan, Y. Xie, B. Wang and R. Zhang, *J. Mater. Res.*, 2014, **29**, 1431–1439.
210 G. Tong, Q. Hu, W. Wu, W. Li, H. Qian and Y. Liang, *J. Mater. Chem.*, 2012, **22**, 17494–17504.
211 C.-C. Lee and D.-H. Chen, *Appl. Phys. Lett.*, 2007, **90**, 193102.
212 C.-C. Lee, Y.-Y. Cheng, H. Y. Chang and D.-H. Chen, *J. Alloys Compd.*, 2009, **480**, 674–680.
213 J. Guo, X. Wang, P. Miao, X. Liao, W. Zhang and B. Shi, *J. Mater. Chem.*, 2012, **22**, 11933–11942.
214 X. G. Liu, D. Y. Geng and Z. D. Zhang, *Appl. Phys. Lett.*, 2008, **92**, 243110.
215 V. F. Meshcheryakov, Y. K. Fetisov, A. A. Stashkevich and G. Viau, *J. Appl. Phys.*, 2008, **104**, 063910.
216 S. Zhang and H. C. Zeng, *Chem. Mater.*, 2010, **22**, 1282–1284.
217 T. Yamauchi, Y. Tsukahara, K. Yamada, T. Sakata and Y. Wada, *Chem. Mater.*, 2011, **23**, 75–84.
218 T. Yamauchi, Y. Tsukahara, T. Sakata, H. Mori, T. Yanagida, T. Kawai and Y. Wada, *Nanoscale*, 2010, **2**, 515–523.
219 L. Liang, X. Guo, Z. Bai, B. Zhao and R. Zhang, *Powder Technol.*, 2017, **319**, 245–252.
220 B. Zhao, W. Zhao, G. Shao, B. Fan and R. Zhang, *ACS Appl. Mater. Interfaces*, 2015, **7**, 12951–12960.
221 W. Xiaoxia, D. Lifeng, Z. Baoqin, Y. Mingxun and L. Jingquan, *Nanotechnology*, 2016, **27**, 125602.
222 X. Wang, B. Zhang, W. Zhang, M. Yu, L. Cui, X. Cao and J. Liu, *Sci. Rep.*, 2017, **7**, 1584.
223 N. E. Kazantseva, J. Vilčáková, V. Křesálek, P. Sáha, I. Sapurina and J. Stejskal, *J. Magn. Magn. Mater.*, 2004, **269**, 30–37.
224 P. Xu, X. Han, J. Jiang, X. Wang, X. Li and A. Wen, *J. Phys. Chem. C*, 2007, **111**, 12603–12608.
225 Z. Wu, D. Tan, K. Tian, W. Hu, J. Wang, M. Su and L. Li, *J. Phys. Chem. C*, 2017, **121**, 15784–15792.
226 C. Cui, Y. Du, T. Li, X. Zheng, X. Wang, X. Han and P. Xu, *J. Phys. Chem. B*, 2012, **116**, 9523–9531.
227 X. Dong, X. Zhang, H. Huang and F. Zuo, *Appl. Phys. Lett.*, 2008, **92**, 013127.
228 W. Li, T. Qiu, L. Wang, S. Ren, J. Zhang, L. He and X. Li, *ACS Appl. Mater. Interfaces*, 2013, **5**, 883–891.
229 C. Gong, X. Wang, X. Zhang, X. Zhao, H. Meng, Y. Jia, J. Zhang and Z. Zhang, *Mater. Lett.*, 2014, **121**, 81–84.
230 B. Zhao, G. Shao, B. Fan, W. Guo, Y. Xie and R. Zhang, *J. Magn. Magn. Mater.*, 2015, **382**, 78–83.
231 J. Deng, Q. Wang, Y. Zhou, B. Zhao and R. Zhang, *RSC Adv.*, 2017, **7**, 9294–9302.
232 V. Castel, J. B. Youssef and C. Brosseau, *J. Nanomaterials*, 2007, **2007**, 27437.
233 X. G. Liu, J. J. Jiang, D. Y. Geng, B. Q. Li, Z. Han, W. Liu and Z. D. Zhang, *Appl. Phys. Lett.*, 2009, **94**, 053119.
234 N. Sun, B. Du, F. Liu, P. Si, M. Zhao, X. Zhang and G. Shi, *J. Alloys Compd.*, 2013, **577**, 533–537.
235 B. Zhao, G. Shao, B. Fan, W. Zhao and R. Zhang, *J. Mater. Sci. : Mater. Electron.*, 2015, **26**, 8848–8853.
236 B. Zhao, G. Shao, B. Fan, Y. Chen and R. Zhang, *Physica B*, 2014, **454**, 120–125.
237 B. Zhao, G. Shao, B. Fan, W. Zhao, Y. Xie and R. Zhang, *Phys. Chem. Chem. Phys.*, 2015, **17**, 8802–8810.
238 X. Liu, C. Feng, S. W. Or, Y. Sun, C. Jin, W. Li and Y. Lv, *RSC Adv.*, 2013, **3**, 14590–14594.
239 S. Xu, M. Zhao, Z. Cai, N. Sun, F. Liu, B. Du, X. Zhang and Z. Ling, *Acta Metall. Sin.*, 2013, **26**, 385–389.
240 B. Zhao, G. Shao, B. Fan, W. Zhao and R. Zhang, *RSC Adv.*, 2014, **4**, 57424–57429.
241 X. Liu, C. Feng, S. W. Or, C. Jin, F. Xiao, A. Xia, W. Li, Y. Sun and S. Zhao, *Mater. Res. Bull.*, 2013, **48**, 3887–3891.
242 B. Zhao, J. Liu, X. Guo, W. Zhao, L. Liang, C. Ma and R. Zhang, *Phys. Chem. Chem. Phys.*, 2017, **19**, 9128–9136.
243 J. Huang, Y. Qin, J. Li, X. Jiang and F. Ma, *J. Nanosci. Nanotechnol.*, 2008, **8**, 3967–3972.
244 H. Guan, Y. Wang, C. Dong, G. Chen, X. Xiao and Y. Wang, *Ceram. Int.*, 2015, **41**, 5688–5695.
245 B.-L. Tang, J. He, T.-H. Ji and X.-L. Wang, *Chin. Phys. B*, 2009, **18**, 2571.
246 T. Liu, Y. Pang, X. Xie, W. Qi, Y. Wu, S. Kobayashi, J. Zheng and X. Li, *J. Alloy Compd.*, 2016, **667**, 287–296.
247 B. Wang, J. Zhang, T. Wang, L. Qiao and F. Li, *J. Alloy Compd.*, 2013, **567**, 21–25.
248 Q. Hu, G. Tong, W. Wu, F. Liu, H. Qian and D. Hong, *CrystEngComm*, 2013, **15**, 1314–1323.
249 H. Li, Y. Huang, G. Sun, X. Yan, Y. Yang, J. Wang and Y. Zhang, *J. Phys. Chem. C*, 2010, **114**, 10088–10091.
250 R. F. Zhuo, H. T. Feng, J. T. Chen, D. Yan, J. J. Feng, H. J. Li, B. S. Geng, S. Cheng, X. Y. Xu and P. X. Yan, *J. Phys. Chem. C*, 2008, **112**, 11767–11775.
251 T. Xia, C. Zhang, N. A. Oyler and X. Chen, *Adv. Mater.*, 2013, **25**, 6905–6910.
252 K. Li, J. Xu, X. Yan, L. Liu, X. Chen, Y. Luo, J. He and D. Z. Shen, *Appl. Phys. Lett.*, 2016, **108**, 183102.
253 Q. Zhang, C. Li, Y. Chen, Z. Han, H. Wang, Z. Wang, D. Geng, W. Liu and Z. Zhang, *Appl. Phys. Lett.*, 2010, **97**, 133115.
254 G. Wan, L. Yu, X. Peng, G. Wang, X. Huang, H. Zhao and Y. Qin, *RSC Adv.*, 2015, **5**, 77443–77448.

255 J. Dong, R. Ullal, J. Han, S. Wei, X. Ouyang, J. Dong and W. Gao, *J. Mater. Chem. A*, 2015, **3**, 5285–5288.
256 C.-L. Zhu, M.-L. Zhang, Y.-J. Qiao, G. Xiao, F. Zhang and Y.-J. Chen, *J. Phys. Chem. C*, 2010, **114**, 16229–16235.
257 T. Wang, J. He, J. Zhou, X. Ding, J. Zhao, S. Wu and Y. Guo, *Microporous Mesoporous Mater.*, 2010, **134**, 58–64.
258 W. Zhou, C. Cheng, J. Liu, Y. Y. Tay, J. Jiang, X. Jia, J. Zhang, H. Gong, H. H. Hng, T. Yu and H. J. Fan, *Adv. Funct. Mater.*, 2011, **21**, 2439–2445.
259 P. Sun, W. Zhao, Y. Cao, Y. Guan, Y. Sun and G. Lu, *CrystEngComm*, 2011, **13**, 3718–3724.
260 X. W. Lou, Y. Wang, C. Yuan, J. Y. Lee and L. A. Archer, *Adv. Mater.*, 2006, **18**, 2325–2329.
261 H. Wang and A. L. Rogach, *Chem. Mater.*, 2013, **26**, 123–133.
262 C. Cheng, B. Liu, H. Yang, W. Zhou, L. Sun, R. Chen, S. F. Yu, J. Zhang, H. Gong and H. Sun, *ACS Nano*, 2009, **3**, 3069–3076.
263 H. T. Feng, R. F. Zhuo, J. T. Chen, D. Yan, J. J. Feng, H. J. Li, S. Cheng, Z. G. Wu, J. Wang and P. X. Yan, *Nanoscale Res. Lett.*, 2009, **4**, 1452–1457.
264 Q. Liu, Q. Cao, H. Bi, C. Liang, K. Yuan, W. She, Y. Yang and R. Che, *Adv. Mater.*, 2016, **28**, 486–490.
265 J. Liu, J. Cheng, R. Che, J. Xu, M. Liu and Z. Liu, *ACS Appl. Mater. Interfaces*, 2013, **5**, 2503–2509.
266 J. Liu, J. Xu, R. Che, H. Chen, M. Liu and Z. Liu, *Chem. Eur. J.*, 2013, **19**, 6746–6752.
267 M. Yu, C. Liang, M. Liu, X. Liu, K. Yuan, H. Cao and R. Che, *J. Mater. Chem. C*, 2014, **2**, 7275–7283.
268 B. Zhao, G. Shao, B. Fan, W. Zhao, Y. Chen and R. Zhang, *RSC Adv.*, 2015, **5**, 9806–9814.
269 J. Lv, Y. Cheng, W. Liu, B. Quan, X. Liang, G. Ji and Y. Du, *J. Mater. Chem. C*, 2018, **6**, 1822–1828.
270 B. Zhao, X. Guo, Y. Zhou, T. Su, C. Ma and R. Zhang, *CrystEngComm*, 2017, **19**, 2178–2186.
271 F. Qin and C. Brosseau, *J. Appl. Phys.*, 2012, **111**, 061301.
272 R. Che, L. M. Peng, X. F. Duan, Q. Chen and X. Liang, *Adv. Mater.*, 2004, **16**, 401–405.
273 P. C. Watts, W. K. Hsu, A. Barnes and B. Chambers, *Adv. Mater.*, 2003, **15**, 600–603.
274 R. Lv, F. Kang, J. Gu, X. Gui, J. Wei, K. Wang and D. Wu, *Appl. Phys. Lett.*, 2008, **93**, 223105.
275 M.-S. Cao, W.-L. Song, Z.-L. Hou, B. Wen and J. Yuan, *Carbon*, 2010, **48**, 788–796.
276 J. Qiu and T. Qiu, *Carbon*, 2015, **81**, 20–28.
277 A. Shah, A. Ding, Y. Wang, L. Zhang, D. Wang, J. Muhammad, H. Huang, Y. Duan, X. Dong and Z. Zhang, *Carbon*, 2016, **96**, 987–997.
278 G. Li, T. Xie, S. Yang, J. Jin and J. Jiang, *J. Phys. Chem. C*, 2012, **116**, 9196–9201.
279 G. Shen, M. Xu and Z. Xu, *Mater. Chem. Phys.*, 2007, **105**, 268–272.
280 P.-B. Liu, Y. Huang and X. Sun, *ACS Appl. Mater. Interfaces*, 2013, **5**, 12355–12360.
281 B. Shen, Y. Li, W. Zhai and W. Zheng, *ACS Appl. Mater. Interfaces*, 2016, **8**, 8050–8057.
282 B. Shen, W. Zhai, M. Tao, J. Ling and W. Zheng, *ACS Appl. Mater. Interfaces*, 2013, **5**, 11383–11391.
283 Y. Wang, D. Chen, X. Yin, P. Xu, F. Wu and M. He, *ACS Appl. Mater. Interfaces*, 2015, **7**, 26226–26234.
284 D. X. Yan, H. Pang, B. Li, R. Vajtai, L. Xu, P. G. Ren, J. H. Wang and Z. M. Li, *Adv. Funct. Mater.*, 2015, **25**, 559–566.
285 Z. Chen, C. Xu, C. Ma, W. Ren and H. M. Cheng, *Adv. Mater.*, 2013, **25**, 1296–1300.
286 Y. Zhang, Y. Huang, T. Zhang, H. Chang, P. Xiao, H. Chen, Z. Huang and Y. Chen, *Adv. Mater.*, 2015, **27**, 2049–2053.
287 B. Shen, Y. Li, D. Yi, W. Zhai, X. Wei and W. Zheng, *Carbon*, 2017, **113**, 55–62.
288 W.-L. Song, X.-T. Guan, L.-Z. Fan, Y.-B. Zhao, W.-Q. Cao, C.-Y. Wang and M.-S. Cao, *Carbon*, 2016, **100**, 109–117.
289 H. Lv, G. Ji, H. Zhang and Y. Du, *RSC Adv.*, 2015, **5**, 76836–76843.
290 H. Lv, H. Zhang and G. Ji, *Part. Part. Syst. Char.*, 2016, **33**, 656–663.
291 V. Sunny, D. S. Kumar, P. Mohanan and M. R. Anantharaman, *Mater. Lett.*, 2010, **64**, 1130–1132.
292 X. F. Zhang, X. L. Dong, H. Huang, Y. Y. Liu, W. N. Wang, X. G. Zhu, B. Lv, J. P. Lei and C. G. Lee, *Appl. Phys. Lett.*, 2006, **89**, 053115.
293 X. G. Liu, B. Li, D. Y. Geng, W. B. Cui, F. Yang, Z. G. Xie, D. J. Kang and Z. D. Zhang, *Carbon*, 2009, **47**, 470–474.
294 G. Li, L. Wang, W. Li and Y. Xu, *ChemPhysChem*, 2015, **16**, 3458–3467.
295 H.-B. Zhao, Z.-B. Fu, H.-B. Chen, M.-L. Zhong and C.-Y. Wang, *ACS Appl. Mater. Interfaces*, 2016, **8**, 1468–1477.
296 Z. Yanan, Z. Xingmiao, Q. Bin, J. Guangbin, L. Xiaohui, L. Wei and D. Youwei, *Nanotechnology*, 2017, **28**, 115704.
297 W. Liu, Q. Shao, G. Ji, X. Liang, Y. Cheng, B. Quan and Y. Du, *Chem. Eng. J.*, 2017, **313**, 734–744.
298 H.-B. Zhao, Z.-B. Fu, X.-Y. Liu, X.-C. Zhou, H.-B. Chen, M.-L. Zhong and C.-Y. Wang, *Ind. Eng. Chem. Res.*, 2018, **57**, 202–211.
299 X. M. Bian, L. Liu, H. B. Li, C. Y. Wang, Q. Xie, Q. L. Zhao, S. Bi and Z. L. Hou, *Nanotechnology*, 2017, **28**, 045710.
300 G. Tong, F. Liu, W. Wu, F. Du and J. Guan, *J. Mater. Chem. A*, 2014, **2**, 7373–7382.
301 J. Jiang, X. Zhang, Z. Dan, J. Ma, Y. Lin, M. Li, C.-W. Nan and Y. Shen, *ACS Appl. Mater. Interfaces*, 2017, **9**, 29717–29731.
302 S. Umrao, T. K. Gupta, S. Kumar, V. K. Singh, M. K. Sultania, J. H. Jung, I.-K. Oh and A. Srivastava, *ACS Appl. Mater. Interfaces*, 2015, **7**, 19831–19842.
303 J. Feng, F. Pu, Z. Li, X. Li, X. Hu and J. Bai, *Carbon*, 2016, **104**, 214–225.
304 W.-L. Song, X.-T. Guan, L.-Z. Fan, W.-Q. Cao, C.-Y. Wang, Q.-L. Zhao and M.-S. Cao, *J. Mater. Chem. A*, 2015, **3**, 2097–2107.
305 D. Guo, K. Cai and Y. Wang, *J. Mater. Chem. C*, 2017, **5**, 2531–2541.
306 P. Martins, A. C. Lopes and S. Lanceros-Mendez, *Prog. Polym. Sci.*, 2014, **39**, 683–706.
307 M. Kanik, O. Aktas, H. S. Sen, E. Durgun and M. Bayindir, *ACS Nano*, 2014, **8**, 9311–9323.
308 S. Yu, F. Qin and G. Wang, *J. Mater. Chem. C*, 2016, **4**, 1504–1510.
309 X. Lv, J. Guo, C. Zhao, Y. Wei, J. Zhang, Z. Wu and C. Gong, *Mater. Lett.*, 2017, **201**, 43–45.
310 Y. Lai, S. Wang, D. Qian, S. Zhong, Y. Wang, S. Han and W. Jiang, *Ceram. Int.*, 2017, **43**, 12904–12914.
311 J. Fang, W. Zha, M. Kang, S. Lu, L. Cui and S. Li, *J. Mater. Sci.*, 2013, **48**, 8060–8067.
312 Y. Cao, Q. Su, R. Che, G. Du and B. Xu, *Synth. Met.*, 2012, **162**, 968–973.
313 Z. Zhu, X. Sun, G. Li, H. Xue, H. Guo, X. Fan, X. Pan and J. He, *J. Magn. Magn. Mater.*, 2015, **377**, 95–103.
314 G. Liu, W. Jiang, D. Sun, Y. Wang and F. Li, *Appl. Surf. Sci.*, 2014, **314**, 523–529.
315 H. Yuan, F. Yan, C. Li, C. Zhu, X. Zhang and Y. Chen, *ACS Appl. Mater. Interfaces*, 2018, **10**, 1399–1407.
316 T. Chen, F. Deng, J. Zhu, C. Chen, G. Sun, S. Ma and X. Yang, *J. Mater. Chem.*, 2012, **22**, 15190–15197.

